MODELLING, ANALYSIS AND DESIGN OF BIOELECTRONIC CIRCUITS IN VLSI

A thesis presented in partial fulfilment of the requirements for the degree of

Doctor of Philosophy

in

Electronics and Computer Engineering

at Massey University, Albany, New Zealand.

Sadia Alam

October 2015

ABSTRACT

Biological phenomena at the molecular level are being imitated by electronic circuits. The immense effectiveness and versatility of bioelectronic circuits have yielded multiple benefits to both the electronic, and the biological worlds. Advancement in technology is being made towards the design and implementation of these systems due to their extreme proficiency and extraordinary capabilities. Development of bioelectronic circuits is assisting researchers to gain deep insights into complex processes of life. These systems are classified into different categories depending on the various kinds and nature of the biological processes. Cytomorphic and neuromorphic circuits are two major classifications of the bioelectronic systems.

Cytomorphic circuits mimic the biological processes taking place inside a living cell. Activities involved in DNA-protein interactions play a vital role for the survival of living organisms. This thesis illustrates modelling and the design of the cytomorphic circuits in VLSI representing the DNA-protein interactions at the molecular level. Electronic circuits imitating neural activities are classified as neuromorphic circuits. The significance of these bioelectronic circuits cannot be denied. Hence, an effort is made in this research to model neuron-to-neuron communication process through electronic circuit components in VLSI. For an electronic representation of these phenomena, biological to electrical analogies are determined, analysed, and modelled. Circuit design validation is accomplished by comparing the circuit results with experimentally reported biological data.

The cytomorphic circuit is capable of analysing the cellular behaviour of living organisms, while the neuromorphic circuit is competent to mimic the neurological processes that are dependent on neuron-to-neuron combination such as neural DNA transcription initiation. Biological experimentation on bacteria *Escherichia coli* is carried out that validates that the cytomorphic VLSI circuit design is capable of predicting gene behaviour of living organisms. The neuromorphic circuit is fabricated using 0.13µm IBM CMOS technology and fabrication results are illustrated in the thesis. Electronic gene oscillators and neural DNA transcription initiation circuits are illustrated as applications of the proposed VLSI bioelectronic circuit designs.

ACKNOWLEDGEMENTS

The doctoral research work carried out in the last four years could not have been achieved without the assistance and direction of others. First and foremost, I would like to express my utmost appreciation to my research supervisor, Dr. S. M. Rezaul Hasan. Without his help and advice, I would not have been able to accomplish my research goals. I gratefully acknowledge the support of my co-supervisors and staff at the School of Engineering and Advanced Technology and the Institute of Natural and Mathematical Sciences. I sincerely thank Massey University for funding my PhD study.

I would like to express my deep acknowledgment to Professor Stephen Marsland for his kind support and immense cooperation during my studies. I really appreciate his willingness to help me out during critical situations.

I owe my deepest gratitude to my co-supervisor, Associate Professor Edmund Lai for his generous guidance and suggestions at my time of need. His encouragement, interest in my work, and immense knowledge always motivates me.

I am indebted to Professor Serge Demidenko for reviewing my research and providing significant advice, thereby enabling me to improve it.

I sincerely thank Mr. Joe Wang for assisting me during circuit testing. I am thankful to Mr. Jarod Young and Miss Natasha Comer from the Institute of Natural and Mathematical Sciences, Massey University. I am really appreciative of Mr. Young for his selfless dedication and guidance at a difficult time. Without his assistance, I would not have been able to perform the biological experiments.

I would like to convey sincere thanks to all my fellow students at the University for their sincere and appropriate suggestions.

TABLE OF CONTENTS

LIST OF ABBREVIATIONS

Acetyl CoA	Acetyl Coenzyme A
ACh	Acetylcholine
BiCMOS	Bipolar-CMOS
BJT	Bipolar Junction Transistor
Ca^{+2}	Calcium ion
CaMKIV	Ca^{+2}/calModulin-dependent protein Kinase IV
CAT	Choline AcetylTransferase
CMOS	Complementary Metal Oxide Semiconductor
CREB	cAMP-Responsive Element Binding Protein
DNA	Deoxyribonucleic acid
E.coli	Escherichia coli
EPC	End Plate Current
EPSP	Excitatory Postsynaptic Potential
IC	Integrated Circuit
Lac	Lactose
MATLAB	MATrix LABoratory
Memristor	Memory Resistor
miRNA	Micro Ribonucleic Acid
MOSFET	Metal Oxide Semiconductor Field Effect Transistor
mRNA	Messenger Ribonucleic Acid
NMOS	n-channel MOSFET
ONPG	*o*-nitrophenyl-β-galactoside
OpAmp	Operational Amplifier
pCREB	Phosphorylated CREB
PMOS	p-channel MOSFET
Pre-miRNA	Precursor Micro Ribonucleic Acid
Pri-miRNA	Primary Micro Ribonucleic Acid
RNA	Ribonucleic Acid
TiO_2	Titanium dioxide
VLSI	Very Large Scale Integration

LIST OF FIGURES

LIST OF TABLES

CHAPTER 1
INTRODUCTION

1.1 BIOELECTRONICS

The term *Bioelectronics* defines a discipline that combines electronic principles and biological phenomena. The versatile characteristics of the discipline are increasing its demand in areas crucial for a nation's economy and interests. Medical treatment, healthcare, and technology advancement are some of the major fields to benefit from *Bioelectronics* [1]. Both the research and the development of bioelectronic circuits have gained immense importance during the last few decades. These circuits are either designed by implementing the analogies between biological systems and electronic circuits or by combining biomaterials and electronic elements.

A *biomimetic* approach is followed in order to design a bioelectronic circuit and systems. It involves the development of electronic devices/models based on the functionality and unique characteristics of bio-cellular interactions, biochemical pathways, or the structure of any biological element [2]. Bioelectronics can be divided into following two sub fields:

- *Cytomorphic electronics:* Electronics inspired by cellular and molecular biology [3]. DNA-protein networks, gene expression mechanisms and cellular functionalities are mimicked by VLSI electronic circuits in a cytomorphic emulation [3].
- *Neuromorphic electronics*: Electronics inspired by neurobiology [3], [4]. Through the neuromorphic approach, neural circuit dynamics are emulated by analog complementary metal-oxide semiconductor (CMOS) very large scale integration (VLSI) circuits [5], [6].

1.2 MOTIVATION

A living cell is densely populated with complex molecular biochemical processes. A bioelectronic circuit explicitly targeting a biological process at the molecular level can be utilized to electronically simulate and analyse an organism's behaviour corresponding to that particular process. The development and behaviour of organisms ranging from bacteria to humans are controlled by gene regulatory circuits [7]. Gene

regulatory circuit means a network of genes in which each gene is either controlling the processing of itself or the processing of other genes [7]. Consequently, a gene can be advanced further or can be suppressed. Gene expression and regulation mechanisms can be interpreted by their analogous integrated circuit entities [8]. Gene expression is a process that determines characteristics of a living organism, while the regulation mechanisms refer to the complex control mechanisms that direct the process of gene expression within cellular organisms [8]. In 1970s, there were significant advances in the fields of computation and nonlinear dynamics. This progress guided the way towards the mathematical modelling of gene expression. Later, with the development of technology, complex gene regulatory circuits were analysed through electrical and electronic circuits. Analogies between biological and electrical entities were developed [9]. Circuit analysis techniques helped understand different components of gene networks. Some of these components are responsible for communication among cells, while others operate as switches or oscillators [10]. The estimated number of genes ranges from 40,000 to 1,000,000 approximately. Since, it is impractical to determine relationships among countless genes; it is necessary to scale down complex features of large gene regulatory systems into smaller subdivisions. This subdivision should be done in such a way that combinations of these small–scale features are able to represent large gene networks and mechanisms [11].

A challenge exists to attain the complex connectivity features and extreme parallel processing characteristics of real time biological systems [12]. The neural computations of a brain are different from traditional computing. The brain follows analog principles of physics, whereas traditional computing operates on digital principles. Mixed-signal (hybrid analog/digital) VLSI circuits are beneficial for emulating real-time behaviour and performing detailed simulations of neural systems [13]. Moreover, the efficiency of current neuromorphic VLSI electronic devices can be enhanced by means of a distinctive circuit element *memristor*. Electronic devices using basic circuit components, developed for highly complex neural mechanisms, are not energy and space efficient. In 1971, Leon Chua drew attention to a fourth fundamental passive circuit element and named it “memristor”, which is actually a resistor with memory. In the current advanced development era of bioelectronic systems, memristor is recognized as the most suitable passive element able to imitate neural activities efficiently [12].

1.3 RESEARCH GOALS

The goal of this research is to electronically model, analyse and develop bioelectronics circuits representing the following biological phenomena:

- Gene expression mechanisms involving DNA–protein interactions within a cell at the molecular level, i.e. a *cytomorphic* electronic circuit, and
- Neuron–to–neuron communication process at molecular level taking place inside the brain, i.e. a *neuromorphic* electronic circuit.

The research steps to be followed are:

1. Explore and analyse the functionality of the biocellular interactions, the stages involved in the DNA–to–protein decoding process, the chemical activities taking place inside the cell, the neuron communication process, and the link between biocellular activities and neuron communication.
2. Develop bioelectronic circuit models for implementing analogies between relevant biological phenomena and electronic circuit components.
3. Design and simulate bioelectronic circuits in VLSI.
4. Test functionality of the bioelectronic circuits through VLSI fabricated chip / biological experimentation.
5. Compare the circuit results with the biological experimentally reported data to validate the design.

1.4 SCOPE OF THE STUDY

The cytomorphic emulations in VLSI electronic systems enable the study and recognition of the behaviour of different sections of complex gene regulatory circuits individually [3],[9]. Consequently, gene control systems can be constructed on the basis of knowledge gained from the analysis of several small modules of a gene system. The purpose of gene control systems is to simulate the innovative behaviour of a species or to fix cellular mechanism malfunctioning [9]. The electronic model of the gene expression mechanisms that will be developed in this research will help to predict the cellular response/behaviour and understand biological processes with minimum effort. The results predicted from the electronic circuit will be observed on the biological

medium and the biological experiment will be carried out on smaller organisms such as bacteria.

Neuromorphic VLSI electronic circuits are low power, intelligent, and real time emulators of neural system dynamics [5]. The reduced computing efficiencies of CMOS digital circuits due to physical limits can be overcome by neuromorphic devices. These highly energy efficient neuromorphic emulators are extremely valuable [14]. Employing complex neural computation techniques for engineering applications, analysing neuron–to–neuron communication phenomena and understanding complicated neural mechanisms are some of the major areas to benefit from neuro-biologically inspired electronic models and devices [14].With the advancement in research, memristive devices can assist future technology to develop neuromorphic electronic chips. Thus, the distinctive nature of the memristor can help in mimicking of complex brain functionality with ease. Memristive neuromorphic bioelectronic circuits can play a significant role in the research field of high performance computing, artificial intelligence, and neural networking [15],[16]. The neuromorphic circuit designs that are not based on memristors are also studied as mentioned in literature review of the thesis, but the recent researches show that memristors are more efficient and suitable for the neuromorphic circuits. Therefore, the neuromorphic circuits propsed in this research have utilized memristors. The neuron-to-neuron communication circuit that will be developed in this research will help to observe the neurons communication process at the molecular level. The neuromorphic chip that will be designed in this doctoral research can be helpful in treatment of neural diseases related to the abnormalities in the neurons communication process. Since, testing of the chip on the neural biological medium is a complicated and expensive procedure, and requires expensive resources and scientific expertise; the chip will not be tested on the neural biological medium.

Since, the cytomorphic and the neuromorphic circuits are generalized for different kinds of organisms; the circuit parameters used in the electronic models are not taken separately for various organisms. Layout details are provided where VLSI fabrication of the circuit is not carried out.

1.5 THESIS ORGANIZATION

This thesis discusses bioelectronic circuit designs and elucidates the contribution of the author in this research field. Taking into consideration the inimitable advantages

of bioelectronic circuits, novel integrated circuit models are proposed for biocellular gene expression regulation mechanisms (cytomorphic circuit) and the synaptic transmission process causing neuron–to–neuron communication (neuromorphic circuit). **Chapter 2** provides a comprehensive review and study of numerous cytomorphic circuits designed by different researchers. Existing neuromorphic circuit designs and development of bioelectronic memristive devices are also illustrated. **Chapter 3** reports a cytomorphic integrated circuit model for biological mechanisms that are involved during gene expression. Since complex biological processes are analysed, their description, which is quite essential, is given at the start of the same chapter. Later, biological to electrical analogies of these processes are determined and modelled followed by simulation results of the VLSI cytomorphic circuit model. **Chapter 4** illustrates the modelling of calcium ion conductance across nerve membrane as a voltage–dependent memristor. Mathematical modelling and simulation results which are carried out in MATLAB environment are discussed. Following this, a novel memristor–based biomimetic (neuromorphic) circuit model for the neuron–to–neuron communication process, i.e. neural synaptic transmission process is presented. **Chapter 5** illustrates a biological experiment performed to examine the gene regulatory mechanism in the bacterium *Escherichia coli*. Analysis and comparison of biological practical results with the cytomorphic circuit simulation outputs not only highlights the design validation, but also emphasizes the circuit application. This chapter also discusses the VLSI fabrication details of the neuromorphic circuit followed by the fabrication test results. In **Chapter 6,** applications of the proposed bioelectronic circuit designs are discussed. Electronic gene oscillators are developed by using the gene cytomorphic circuit, while the neuromorphic circuit is used to model the neural DNA transcription initiation caused by the neuron–to–neuron communication process. The conclusion of the thesis is presented in **Chapter 7** together with a summary of contributions made by the author in the research, and future work suggestions.

CHAPTER 2
LITERATURE REVIEW

2.1 INTRODUCTION

Engineers and scientists are continually striving to develop model and design of bioelectronic circuits that closely mimic the diverse biological processes of living organisms. This chapter provides an overview of various cytomorphic and neuromorphic circuits that have been previously developed.

2.2 CYTOMORPHIC CIRCUITS

Complex interactions among numerous genes and their products control the complicated biological processes of life. DNA sequences follow the processes of transcription and translation and generate gene products such as RNAs and proteins. Different types of RNAs and proteins either produce other biological species or pass through biochemical pathways to control cellular processes. Stages involved in gene expression are also regulated by these gene products [17]. Moreover, biochemical pathways of cellular processes are modulated by enzymatic activities [18]. Cellular circuit models implemented on large scale electronic chips are extremely helpful in cellular behaviour analysis and response prediction. Hybrid analog-digital circuits can model DNA-to-protein biochemical reactions, biochemical pathways, and enzymatic activities. Gene activities and cellular behaviour at the molecular level can be simulated by these cytomorphic circuit models and VLSI chips. Inclusion of stochastic and cellular inconsistency effects makes the simulations more valuable because it shows circuit results under random variation of circuit parameters that can occur in real time environment [3].

2.2.1 Biological Parameters and Electronic Circuit Analogies

Circuit components and the time scale of electrical circuits differ widely from gene circuits. The response time of circuits consisting of transistors, resistors and other electrical components can be in micro seconds, or even less. On the other hand, genetic

processes can take from several minutes to several hours to complete. Due to the dissimilarity in the time scale, the switching rates for protein signals and transistors are different. In spite of these diversities, there are many analogies between electrical and gene operations. Electrical connections are determined by an input signal conducting path. In gene circuits, a biochemical pathway between the sender and receiver of the biological signal establishes connectivity. A Boolean gate can symbolize the behaviour of any electrical process. In the same way, biochemical mechanisms such as the repression or activation of transcriptional promoter elements can also be represented by a Boolean gate [19]. Table 2.1 summarizes some of the features that are comparable in gene and electronic circuits taken from [20].

Table 2. 1. Summary of Gene and Electronic circuit Analogous Parameters as mentioned in [20]

Electronic Logic	Genetic Logic
Collection of charge carriers	Collection of molecules
Resistors	Species decay
Electric Potential	Molecular concentration
Electric Current	Molecular conversion from one specie to another (reaction rate)
Capacitor	Species storage

2.2.2 A Single-Gene Electronic Circuit

Fig. 2.1 shows a cytomorphic circuit model based on a single gene as developed in [20]. It is a model for the gene expression mechanism at a fundamental level. DNA, stands for deoxyribonucleic acid, is molecular specie in which information required for a cell is stored [20]. During the process of transcription, the information stored in DNA is copied into messenger ribonucleic acid (mRNA) strands [20]. From mRNA, protein is synthesized through the process of translation [20]. The authors utilized biological to the electronic analogies mentioned in Table 2.1 and developed mathematical equations for DNA-protein interaction mechanisms based on the law of mass action as follows [20]:

1. Rate of mRNA synthesis from DNA (Transcription process) [20]:

$$\frac{dr}{dt} = -\gamma_R r + \alpha_R \tag{2-1}$$

where r and γ_R denote the mRNA concentration and the decay rate constant respectively. The term $-\gamma_R r$ mimics the mRNA decay rate (hence the negative sign). An enzyme RNA polymerase binds to DNA to produce mRNA. α_R represents the reaction rate of this enzyme.

2. Rate of protein synthesis from mRNA (Translation process) [20]:

$$\frac{dp}{dt} = -\gamma_P p + \alpha_P r \tag{2-2}$$

In the above equation p and γ_P denote the protein concentration and decay rate constant respectively. Protein decay rate is modeled by $-\gamma_P p$. An enzyme RNA polymerase binds to DNA to produce mRNA. α_P represents the rate of protein translation from each mRNA molecule. Simpson *et al.* in [20] designed an electronic model mimicking the DNA-protein interactions by using (2-1) and (2-2) as shown in Fig. 2.1. The capacitors in the figure model storage of these molecular species inside the living cell. It is similar to the hybrid-pi model of a transistor.

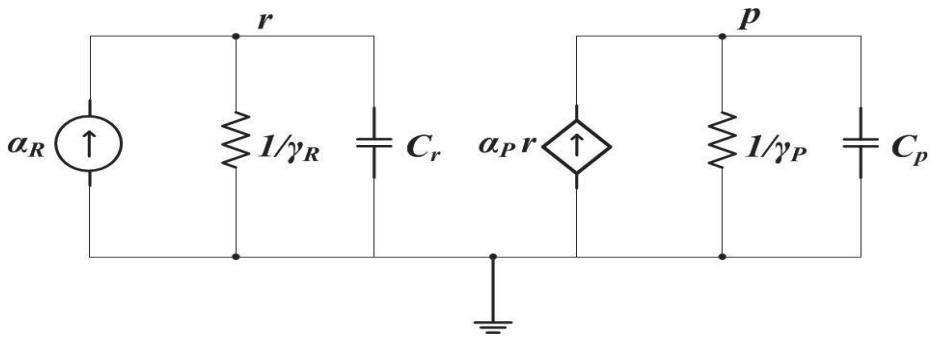

Fig. 2. 1. Electronic circuit model mimicking the DNA-protein interactions of a single gene as shown in [20].

Gene expression is a very complex process involving number of synthesis and degradation stages [21]. Simpson *et al.* in [20] and Hasan in [22] developed electronic model for those stages of the gene expression that only involve synthesis of the molecular specie. The complete gene expression process has not been electronically modelled previously; therefore, there is further scope to model the entire gene expression mechanism, including the synthesis, as well as, the degradation stages. Due to complexity of the molecular mechanisms involved in the gene expression mechanisms, it is very challenging to develop a complete electronic model mimicking the gene expression mechanisms at the molecular level.

2.2.3 Engineered Gene Circuits

Hasty *et al.* [9] explained the correspondence between biological processes and digital logic gates. If the input and output relationship of any gene mechanism follows a logical truth table, the procedure can be regarded as a gene logic gate. An arabinose operon induction process satisfies the AND gate truth table. When AraC proteins and arabinose (inputs) are present, then the arabinose promoter is ON. Absence of any one or both of the inputs keeps the arabinose promoter OFF [9].

External chemical inputs to a living cell can also constitute AND gate logic. For instance, lactose and tetracycline repressor molecules, encoded from LacI and tetR genes respectively, stop gene expression of a green fluorescent protein (*gfp*). Isopropyl-β-D-thiogalactopyranoside (IPTG) stops LacI to repress *gfp* gene transcription, while anhydrotetracycline (aTc) prohibits tetR from inhibiting the transcription process. Hence, ITPG and aTc are essential inducer molecules for *gfp* gene transcription initiation. If any one of these inducer molecules is absent, its corresponding repressor molecule will be in an active state, ultimately repressing *gfp* gene transcription. In this way, *gfp* gene expression controlled by ITPG and aTc inducer molecules follows logic AND gate operation [9]. Hence, in complex gene circuits several molecular interactions can be modelled simply by logic gates.

A regulatory circuit based on the negative feedback path in *E.Coli* was developed by Becskei and Serrano in [23]**.** The tetracycline repressor and the green fluorescent protein were fused together and were placed with two tetracycline operators. This resulted in formation of a negative transcriptional control factor that auto regulated the fused gene. Protein synthesis was more stabilized by the negative auto-regulation as compared to the protein synthesis without feedback path [24]. Although these engineered gene circuits are simple, but by utilizing these simple concepts and approach, extremely complex synthetic gene circuits can be developed. The cytomorphic circuit approach plays a vital role in developing the engineered gene circuits because it helps to simulate the gene behaviour of the synthetic circuit prior to designing it.

2.2.4 Molecular AND Gate Design

Rialle *et al*. [25] have designed a network that can carry out logic AND gate operation by a multi-enzymatic biochemical process. They followed three steps, namely: design, simulation, and experimental validation for developing the network. Design and simulation are carried out by BioNetCAD which is a bioinformatics tool. HSim software and Ordinary Differential Equations (ODE) simulations are supported by BioNetCAD. The AND gate network has two input substrates, which are transformed into one measurable product (output) by an enzymatic pathway consisting of three enzymes. Lactose (input 1) and ABTS (2,2-azino-bis(3-ethylbenzthiazoline-6-sulphonic acid: input 2) are substrates of the β-galactosidase (first) and peroxidise (third) enzymes respectively. The glucose oxidase (second) enzyme is a product of the first enzyme and a substrate of the third one as well [25]. The researchers validated their design by carrying out spectrophotometric analysis.

The AND gate operation is a simple electronic logic that is performed by Rialle *et al*. in [25]. Following their approach, complex electronic circuit functionalities can be simulated by utilizing biological to electronic analogies and the simulation results of biomimetic circuits in VLSI can be validated by spectrophotometric experiments.

2.2.5 Biochemical Feedback Mechanism of Enzyme

Enzymatic reactions take place in response to alterations in cell metabolism (a process that maintains cell's life) and intracellular conditions. Feedback inhibition is categorized as a metabolic control process at the molecular level where an enzyme (a catalyst for chemical reactions) is regulated by a metabolic pathway due to an increase in the pathway product. Catalytic activities of the enzyme are reduced in order to control the metabolism of the cell. Pyrimidine (a biomolecular specie) biosynthetic pathway is a feedback inhibition mechanism that regulates an allosteric enzyme named as aspartate transcarbamoylase (ATCase). Allosteric enzyme is a type of enzyme that changes its binding strength by the action of other molecules [18]. This feedback control process is modelled by Vinoth and Balaji in [18].The electronic circuit representing the complete pyrimidine biosynthetic pathway is shown in Fig. 2.2 [18]. N-carbamoyl-L-aspartate and an inorganic phosphate are produced in the pyrimidine biosynthesis reaction. In this process, carbamoyl phosphate binding along with changes

in ATCase occurs followed by aspartate binding. Cytidine triphosphate (CTP) and Adenosine triphosphate (ATP) are final products of the pyrimidine biosynthetic pathway. CTP inhibits while ATP stimulates the enzyme, ATCase thus forming a feedback control mechanism [18].

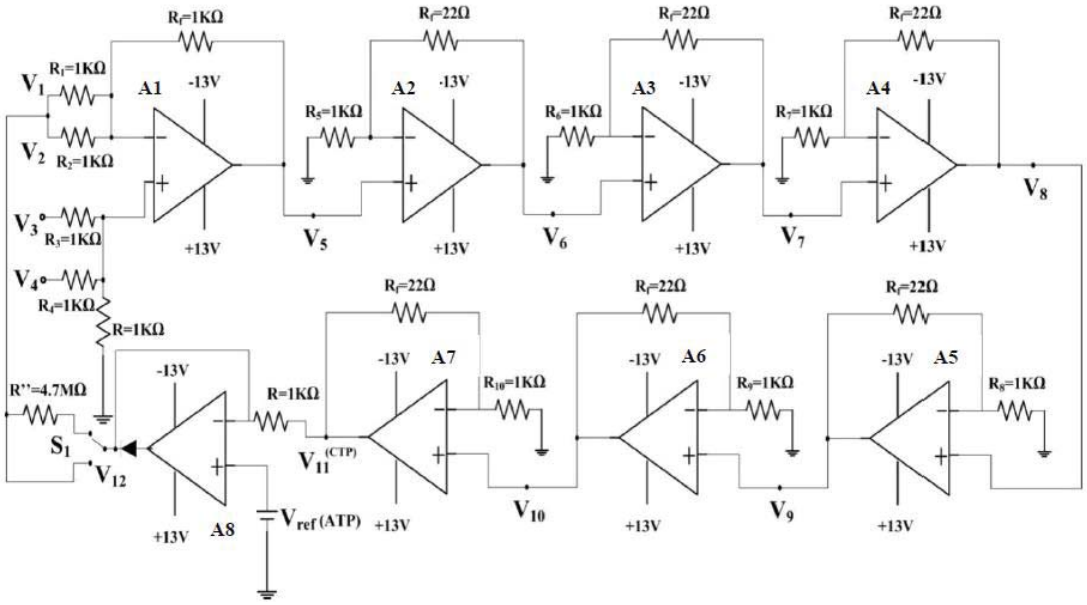

Fig. 2. 2. Complete pyrimidine biosynthetic pathway as developed by Vinoth and Balaji in [18]

2.2.5.1 Parts of Circuit

The circuit can be divided into three parts:

I. The adder- subtractor: Two inputs V_1 and V_2 are connected to the inverting pin of a unity gain amplifier A1 through resistors R_1 and R_2 respectively. These are biochemical inputs ATP or CTP depending on the working of the circuit (explained in section 2.2.5.2) forming a feedback path. V_3 corresponds to carbamoyl phosphate substrate, while V_4 represents aspartate substrate. These two biochemical mimicking inputs are connected to the non-inverting pin of A1 through resistors R_3 and R_4 respectively [18].

II. Non-inverting Amplifier: The adder - subtractor amplifier output goes to the first of six non – inverting amplifiers (A2 to A7) in this part of the circuit. These amplifiers are linked together by connecting the output of each amplifier to the non-inverting pin of next one. Resistors are used to ground the inverting pins of all amplifiers. CTP is the output V_{11} from the sixth non-inverting amplifier, i.e., A7 in Fig 2.2 [18].

III. Precision Clamp : CTP is given as the input to the inverting terminal of another amplifier A8. A resistor R is put in between CTP and A8. The second pin of A8 gets an external input voltage V_{ref} which corresponds to ATP. A diode is placed in the feedback loop of A8 with its cathode facing towards the output side [18].

2.2.5.2 Working Principle

The circuit configuration of a pyrimidine biosynthetic pathway can result in three cases [18]:

I. Case 0: Initially, V_1 and V_2 are set to zero. The enzyme ATCase is neither activated nor inhibited and CTP is the final output of the circuit.

II. Case 1: When $V_{11} > V_{ref}$, then all operational amplifiers produce a negative output which mimics the condition: CTP > ATP : Inhibition of ATCase.

III. Case 2: When $V_{11} < V_{ref}$, positive value appears on the output line of all operational amplifiers. This case corresponds to the following biological situation: CTP < ATP : Activation of ATCase.

CTP and ATP controls ATCase activation through feedback path. The output of amplifier A8 goes to amplifier A1 through V_1 and V_2. When amplifier A8 has ATP as its output, it passes to the input voltage terminals V_1 and V_2 to amplifier A1 as a result ATCase is stimulated and pyrimidine is synthesized. On the other hand, when amplifier A8 has CTP as its output, it passes to the input voltage terminals V1 and V2 to amplifier A1 as a result ATCase is inhibited and pyrimidine synthesis is stopped. Circuit illustrated in Fig 2.2 follows working principle mentioned above and pyrimidine biosynthesis is mimicked. Several complex metabolic and biochemical activities occur during a biological process. Numerous biological processes involve synthesis of chemical/biological products from several reactants controlled by enzymes. Vinoth and Balaji developed the mathematical and electronic relationship among reactants, products and enzymes in [18]. The research presented in this thesis is focused on the cytomorphic and the neuromorphic circuit concepts that will involve complex biological processes concepts; therefore, the model developed in [18] is very useful for mimicking enzymatic reactions for developing the cytomorphic and neuromorphic circuits.

2.3 NEUROMORPHIC CIRCUITS

Neuromorphic analog circuits are able to implement the electronic equivalent of adaption, learning, and memory algorithmic processes efficiently. High density and low power are remarkable features of these VLSI circuit implementations, features which cannot be achieved by digital logic designs [26].

2.3.1 Membrane Electronic Model

Hodgkin and Huxley [27] developed an electronic model of a nerve membrane based on a membrane's electrical behaviour, as shown in Fig. 2.3. They mathematically modelled total membrane current, I, as [27]:

$$I = C_M \frac{dV}{dT} + I_i \tag{2-3}$$

where C_M is the membrane capacitance per unit area, V is the displacement of membrane voltage from its resting value (E_r) and I_i is the sum of ionic currents. I_i is categorized separately according to the type of ion. Ions such as sodium (Na^+), potassium (K^+), calcium (Ca^{2+}), chloride (Cl^-), etc., are present inside and outside a cell membrane [27]. Some of these ions flow from the outside of the cell membrane towards the inside, while others move from the inside to the outside of the membrane [28]. Ionic current components due to sodium and potassium ions are represented by I_{Na} and I_K respectively. Current due to other ions across the cell membrane is modelled by I_L. It is termed as leakage current.

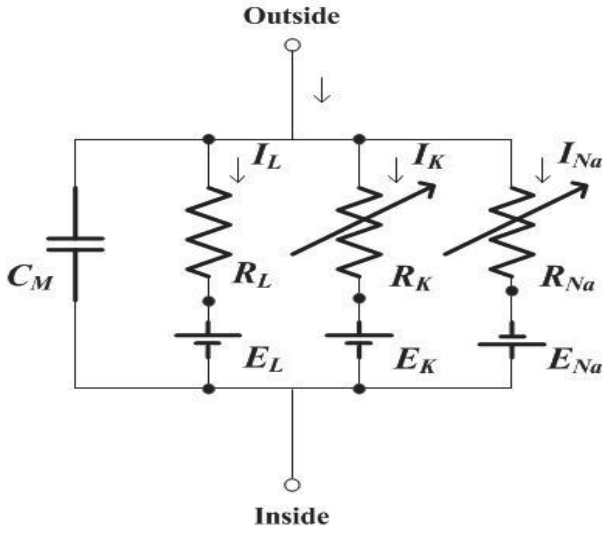

Fig. 2. 3. Electronic Model of nerve membrane proposed by Hodgkin and Huxley in [27]

A product of the driving force and permeability coefficient for a particular ion determines the ionic current through the specific channel, which is only permeable to that ion. The driving force is equal to the electric potential difference across the cell membrane, i.e. the difference between membrane potential and equilibrium potential for a particular ion. A permeability coefficient is analogous to an electric conductance [27],

[29]. In Fig. 2.3 E_{Na}, E_K and E_L denote the equilibrium potential for Na^+, K^+ and other ions respectively. Similarly, g_{Na} (=1/R_{Na}), g_K (=1/R_K) and g_L (=1/R_L) represent the ionic permeability coefficients of Na^+, K^+ and other ions respectively. R_{Na} and R_K are time and membrane voltage dependent [27].

2.3.2 Membrane Electronic Model using Memristors

The three well-known two terminal passive circuit elements are the resistors, inductors and capacitors. Current i, voltage v, charge q and magnetic flux φ are four basic variables which can describe the state of a circuit. Any two of the four circuit variables are linked together in a linear relationship to illustrate the characteristics of each passive circuit element. Leon Chua proposed that there should be another passive circuit element which should satisfy one of the six linear relationships of the basic circuit variables. He named the fourth element as "Memristor" and fitted it into the association between charge and magnetic flux as depicted in Fig. 2.4 [30],

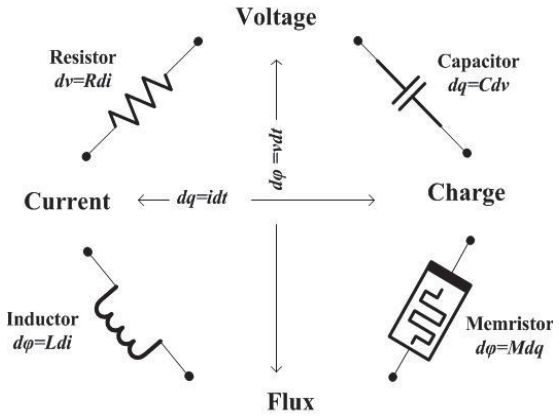

Fig. 2. 4. Placement of Memristor in linear relationship of current, voltage, charge and flux as mentioned in [30]

Chua proposed [31] that the time-varying ionic conductance in the Hodgkin-Huxley membrane electronic model can be efficiently represented by a *memristor*. After decades following Chua's proposal, William and his co-workers recently developed the physical structure of a memristor. TiO_2 is used to build this non-volatile and nonlinear element known as a "Memristor" [32]. According to William and his fellow workers, a memristor has such characteristics which makes it operate in a manner similar to the synapse between two neurons [32].

Chua suggested that conductance across ion channels is analogous to time invariant voltage controlled memristor. By modifying the equations stated for current controlled memristor in [33], a voltage controlled memristor can be mathematically represented by:

$$i = G(w,v)v \tag{2-4}$$

$$\frac{dw}{dt} = f(w,v) \tag{2-5}$$

where i is current through the memristor, v is the voltage across the memristor, the device state variable is symbolized by w, G is conductance which is a function of the device internal state and input voltage and f is a vector function. The memristor can be sketched as a semiconductor film with a thickness of D. The area of semiconductor which is highly doped has low resistance R_{ON}, while the less or almost un-doped region has high resistance R_{OFF}. The size of both regions changes due to a drifting of the charged dopants with an alteration in the value of the external voltage $v(t)$[33]. Frequency dependent voltage versus current graph of a memristor is a close hysteresis loop passing through origin. This frequency dependent graphical representation is known as a Lissajous figure as shown in Fig. 2.5 in [31].

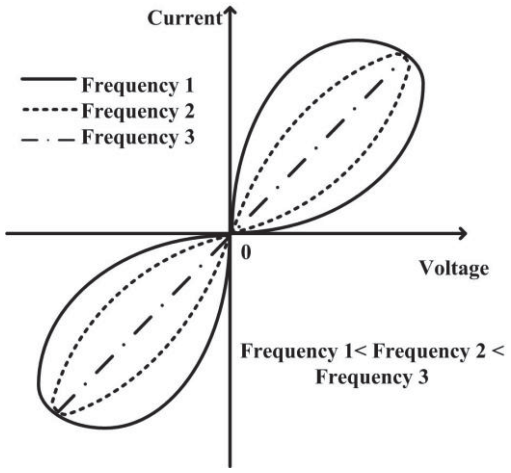

Fig. 2. 5. Lissajous Figure: Frequency dependent voltage versus current graph mentioned in [31]

2.3.3 Synaptic Transmission Model

Hutchison [34] electronically emulated the synaptic transmission process occurring between two neurons. The neuron that transmits the signal is identified as the presynaptic neuron, while the term 'postsynaptic' is used for the receiving neuron.

During the synaptic transmission process, an action potential (an electric signal) stimulates the presynaptic neuron and voltage gated calcium channels are opened. Ca^{2+} influx occurs, which releases neurotransmitters into a region between the presynaptic and postsynaptic neurons known as s*ynapse*, or, more specifically synaptic cleft. As a result, ligand gated ion channels are opened in the postsynaptic neuron, ionic flux occurs, and neuron membrane potential is induced [34]. Hutchison initially presented mathematical equations for synaptic transmission kinetics. Afterwards, the researcher made these mathematical equations a basis for emulating a synaptic transmission process electronically. Current produced due to the Ca^{2+} influx at the presynaptic neuron membrane, I_{Ca} is given by [34]:

$$I_{Ca}=i_{channel}C_o \tag{2-6}$$

where $i_{channel}$ is the Ca^{2+} flow through a voltage gated open channel and C_o is the number of open channels on the membrane. C_o is the product of the number of Ca^{2+} channels, and the probability of a single channel opening $i_{channel}$ is defined by the Goldman-Hodgkin-Katz current equation [34]:

$$i_{channel} = P_{Ca} * \frac{4F^2}{RT} * V * \left[\frac{c_i - c_e \exp\left(\frac{-2FV}{RT}\right)}{1 - \exp\left(\frac{-2FV}{RT}\right)} \right] \tag{2-7}$$

where P_{Ca} is the membrane's permeability to Ca^{2+} ions, F is Faraday constant, R represents the ideal gas constant, T is temperature, V is membrane voltage, and Ca^{2+} ion concentrations internal and external to the presynaptic neuron membrane are denoted by c_i and c_e respectively. Input to the circuit is membrane voltage. Logarithmic feedback of the signal gives the Ca^{2+} ion channel opening probability. The signal is then input to an exponentiation amplifier whose output is integrated with a capacitor. The processed signal is passed through a transistor which is controlled by an action potential signal. A log amplifier receives the output of the transistor. The fed forward signals through the log amplifier are added together. The exponential value of the summed signal represents the current stimulation at the postsynaptic membrane.

Although a thorough mathematical model is provided in [34] for the synaptic transmission process, it lacks a comprehensive explanation of the discrete circuit

components corresponding to each mathematical equation because only description of circuit architecture for emulating the synaptic transmission process is discussed in [34] instead of a circuit diagram. Circuit parameter values are also not mentioned. Moreover, the author did not discuss in detail the electronic emulation of the biological phenomenon taking place at the postsynaptic neuron as it only provides an equation that represents the current stimulation at the postsynaptic membrane.

2.3.4 Memristor Bridge Synapse Circuit

Kim *et al.* [32] proposed a memristor bridge synapse circuit consisting of four memristors forming a Wheatstone bridge and three transistors. Small and thin sized signals are used as input while synaptic weights are programmed by large and extensive pulses. Memristance value is controlled by applying large signals across each memristor. The linear resistive behaviour of a memristor bridge during short time intervals makes the weighing operation linear. A differential amplifier is attached to the right side of the memristor bridge, which is responsible for the voltage to the current conversion. The positive terminals of several memristor synaptic bridges are connected together along with a cell biasing circuitry. This makes a memristor bridge neuron as shown in Fig. 2.6 [32].

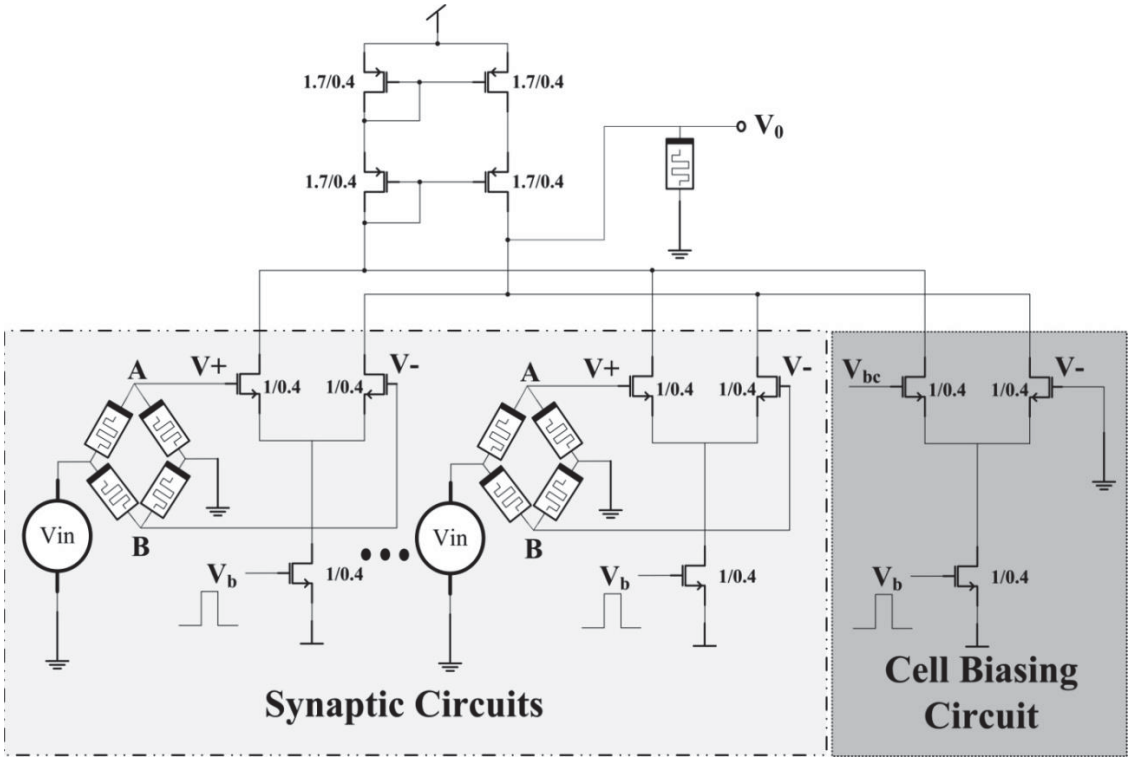

Fig. 2. 6. Memristor Bridge Neuron developed by Kim *et al.* in [32]

The procedure of weighting (multiplication) carried out by a general CMOS circuit is nonlinear and energy consuming. On the other hand, the weighting operation performed by a memristor bridge is linear due to its linear resistive behaviour during short time intervals. The size of the memristor can be less than 5nm, which is far smaller than a transistor's size. Moreover, more transistors are required for making a cell by the cellular neural network approach, while memristor neuron bridge requires fewer transistors. In short, implementation of a neural circuit by using memristors reduces the circuit size, as well as makes it energy efficient [32].

2.3.5 VLSI Neuron Model

Demirkol and Ozogus implemented a low-power VLSI neuron model (as shown in Fig. 2.7) based on the Izhikevich equations mentioned in [35]. The main building block of the model is the first order log-domain filter. An active diode connection is used in one of the two filters present in the design. This reduces current levels resulting in a low power and large time constant circuit design.

The authors modified and rearranged the Izhikevich equations similar to the filter state equations as follows [35]:

$$C_v \dot{I}_v = -I_v(I_a - I_v) * 10^{12} * k\, C_v/\tau + (I_{DC} + I_{in} - I_u) C_v/\tau \tag{2-8}$$

$$C_u \dot{I}_u = -I_u(a\, C_u/\tau) + I_v(ab\, C_u/\tau) \tag{2-9}$$

$$\text{If } I_v >= I_{peak},\ I_v \leftarrow I_c,\ I_u \leftarrow I_u + I_{incr} \tag{2-10}$$

where τ is time constant, k, a and b are dimensionless parameters, and the current required for the DC level shifting of variables I_v and I_u is represented by I_{DC}. I_a , I_{peak} , I_c, I_{incr} and I_{in} stand for shifted threshold value, spike cut off value, I_v reset value, amount of I_u increment at reset time and external input current respectively. C_u and C_v represent capacitances used in the filter. Except for τ, k, a, b, C_u and C_v, all terms are current in pA [35].

Log-domain filter structures implement (2-8) to (2-10). A complete neuron VLSI circuit model including filters and supplementary circuitry representing reset dynamics is shown in Fig. 2.7 [35]. Transistors M1 to M4 represent the equation (2-9), while M7 to M10 and M12 represent equation (2-8). Transistors M13 to M15 form current mirrors

for replicating current I_v. M9 diode connection is provided by a buffer that is formed by a differential pair. Shifted source voltages and active diode connection allow the transistors to work at low current levels and low frequencies, making it a very low power circuit. The firing pattern of real neurons is simulated through the model. Hybrid interface systems can be designed and a VLSI neural networks simulation can be carried out using the neuron model [35].

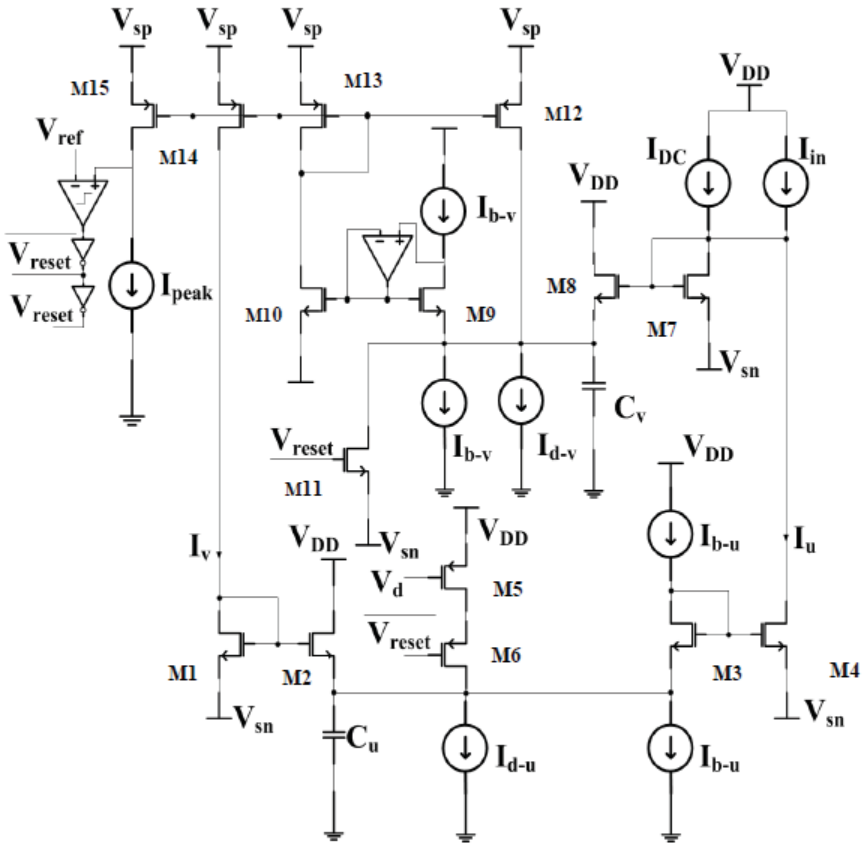

Fig. 2. 7. A VLSI Neuron Model proposed by Demirkol and Ozogus in [35]

2.4 CONCLUSION

In this chapter, an overview of existing cytomorphic gene circuits is discussed including both analog and digital circuit representations of gene – protein interactions and processes involved in between. The biological process which is to be modelled is studied. Afterwards, relevant biological to electrical analogies are determined and analysed. Based on these analogies, electronic circuit models representing the gene activities developed by different researchers are presented. It is elaborated here that integrated circuit modelling can be done for gene expression. Logic gates and oscillators

can mimic different gene mechanisms. Analog modelling of complex processes such as enzymatic activities controlling biochemical pathways is discussed. Moreover, molecular AND gate design carried out by other researchers is also discussed.

A neuron model formerly implemented in VLSI is illustrated. This chapter also throws light on previously designed neuromorphic memristive devices. The unique characteristics of a memristor make it highly distinctive from the other three passive circuit elements, namely resistors, capacitors, and inductors. As a result memristive devices find their place in the currently developing research field of neuromorphic VLSI electronic circuit design.

CHAPTER 3
ELECTRONIC CIRCUIT MODELLING OF GENE EXPRESSION MECHANISMS

3.1 INTRODUCTION

Gene expression regulation directs the development and proper functionality of a living cell. Although there are various types of genes and their products, basic mechanism controlling the gene expression is the same. DNA is the source of all living organisms. DNA directs the process of RNA synthesis, which constitutes one of the core categories of molecules necessary for a cell to possess life [36]. The majority of RNAs take part in the creation of proteins. The process of protein synthesis from its DNA code by passing through several steps is recognized as the gene expression mechanism [37]. In this chapter a brief discussion about the biological stages involved in the gene expression regulation is undertaken. Biological to electronic circuit entities conversion are mentioned, and mathematical equations are developed for every stage. Based on these mathematical equations, a VLSI circuit design is proposed for gene expression mechanisms. Monte Carlo analysis is carried out to prove robustness of the circuit design. The simulation results of the circuit are compared with experimental biologically reported data to validate the design.

3.2 BIOLOGICAL FUNDAMENTALS

Every stage of the gene expression mechanism is different from the other stages in terms of the biological fundamentals involved. A brief description about biological basics of the gene expression mechanism and the stages involved in this mechanism is given in this section.

3.2.1 Gene Expression Mechanism

In Fig. 3.1 the flow of gene expression i.e. protein synthesis from DNA is illustrated and the intermediate stages are indicated by enclosed boxes [36]. After

mRNA transcription from DNA, the gene is either processed in the forward pathway or is stopped from further processing. Translation is the gene expression stage in which mRNA processing is continued. The break down or blockage of the mRNA molecules is controlled by the regulatory action of micro ribonucleic acid (microRNA). In [22], an integrated circuit model of translation for protein formation was provided. However, this model did not include the effect of the post transcription degradation processes. Concentration of a particular protein within the cell is controlled by another important stage known as protein degradation [36],[38]. Biochemical pathways in the gene expression mechanisms are extremely important, as the absence/hindrance of gene regulation factors can cause malfunction in the cell. This breakdown in the cellular biochemical pathway engines can result in many diseases, including cancer [39].

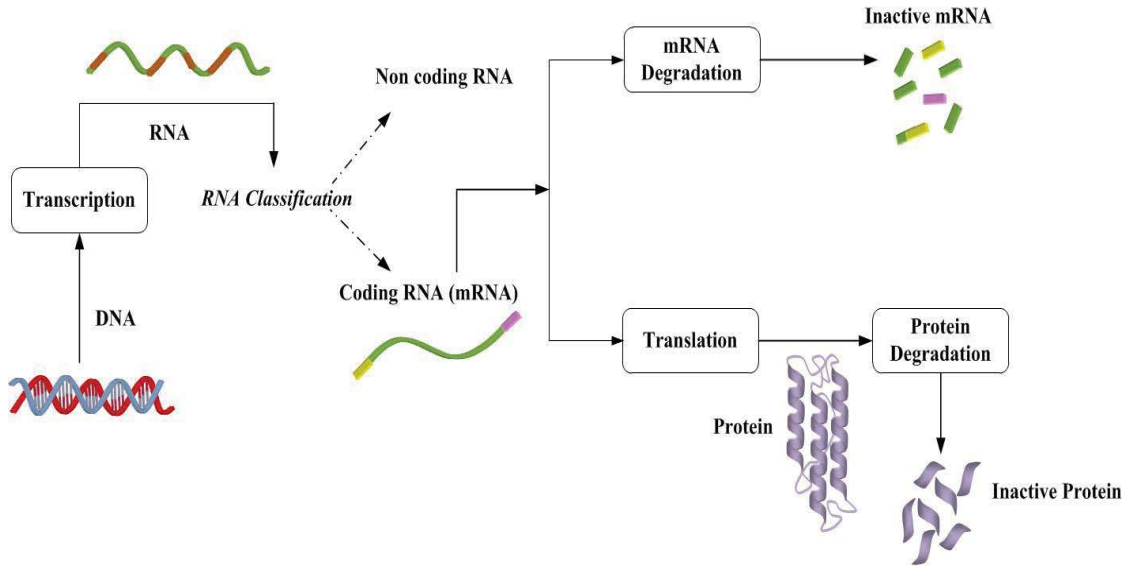

Fig. 3. 1. Gene expression pathway with stages enclosed in square boxes, and input and output of these stages indicated by arrows. The biological representation concept is taken from [36].

3.2.2 Stages of Gene Expression

Gene expression mechanisms play a vital role in developing various characteristics of tissues and cells of all living organisms. Gene expression regulation forms the basis of most of the processes related to the physiology of living organism [40]. During the process of gene expression, a gene releases its biological information to synthesize the required product within a cell [37], [41]. The series of stages involved in the production of protein from DNA [36] are modelled in this chapter. They include the following:

3.2.2.1 Transcription

The RNA molecules are initially produced from the DNA in a reaction catalyzed by an enzyme known as RNA polymerase. The transcript RNA is created as the polymerase progresses down the DNA [36]. Genetic information stored in the DNA molecule is copied to the RNA transcripts [21]. RNAs can be classified into two groups depending on their functionalities: 1) the coding RNA, more specifically, mRNAs that are transcripts of genes containing codes for manufacturing proteins, and 2) the non-coding RNAs that are not directly translated into protein, but are used to carry out various supporting and regulatory roles. This second group of RNAs can be further divided into various types which include transfer RNA (tRNA), ribosomal RNA (rRNA), microRNA (miRNA), and more [36],[41]. There are different types of RNA polymerase enzymes such as RNA polymerase I, II, III. RNA polymerase II mostly transcribes genes into mRNA [21] while RNA polymerase III participates in the miRNA gene transcription [42].

3.2.2.2 mRNA Degradation by miRNA

mRNA breakdown is carried out by the attachment of miRNA to the mRNA complementary sequences. The processes of miRNA synthesis and mRNA degradation by the miRNA are illustrated in Fig. 3.2 [21]. miRNA synthesis involves following two processing steps: 1) the transcription of miRNA genes by the enzyme RNA polymerase to primary transcripts along with the transformation of primary transcripts into miRNA precursors (pre-miRNA) by the Drosha molecule, and 2) slicing of the pre-miRNA by Dicer enzyme [21],[42],[43] . Pre-miRNA is a double stranded transcript. One part of the sliced pre-miRNA is a mature miRNA molecule which attacks the mRNA and degrades it [36].

3.2.2.3 Translation

The genetic information for the protein synthesis copied into the mRNA from the DNA is read by ribosome molecules. Ribosome moves along the mRNA transcripts and protein is synthesized by following the genetic message present in the mRNA. These newly synthesized proteins are termed as final “gene products” [21],[36]. On the

other hand when the DNA is transcribed into non coding RNAs and protein is not the final product of the gene then RNA molecules are known as final gene products [21].

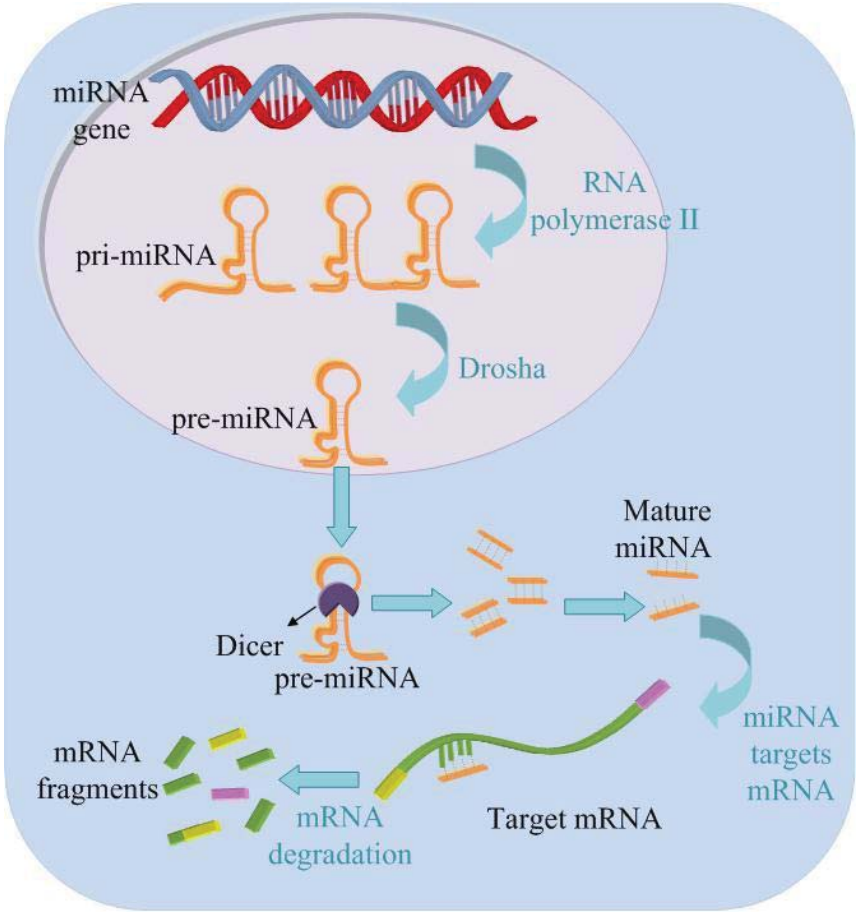

Fig. 3. 2. miRNA synthesis pathway followed by the degradation of the mRNA strands. Double stranded RNA transcripts termed as pri-miRNA are transcribed from DNA which are converted into pre-miRNA by Drosha. Finally, mature miRNA (single strands) are synthesized from pre-miRNA by action of a Dicer enzyme. miRNA attacks the mRNA and degrades it. The biological representation concept is taken from [21], [43].

3.2.2.4 Protein Degradation

Along with the protein synthesis rate, the degradation rate also controls the volume and variety of proteins within a living cell. Protein degradation is crucial for proper functioning of the cell in response to various stimuli and signals [44]. A common mechanism for protein degradation involves the *marker* and *shredder* molecules, ubiquitin and proteasome (large protein complex) respectively. The proteasome identifies the target protein for disposal from its attached ubiquitin molecules ("*flag*

molecules"). The marked protein enters the proteasome, the ubiquitin is detached/released and the protein is degraded [36],[44]. Fig. 3.3 shows the biological process of the protein degradation [36].

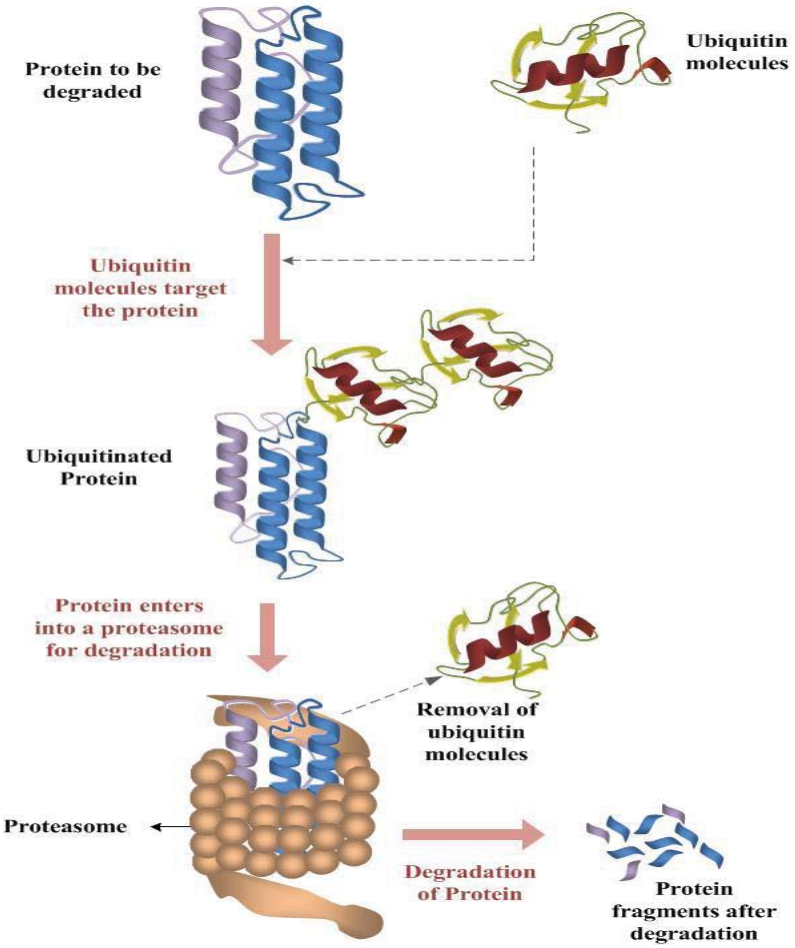

Fig. 3. 3. Biomolecular representation of the protein degradation pathway. Protein to be degraded is targeted by the ubiquitin molecules. Ubiquitinated (marked) protein enters the proteasome where it is degraded. The biological representation concept is taken from [36].

3.2.3 Transcription Control Mechanism

There are two kinds of gene regulation at the transcriptional level: negative gene regulation and positive gene regulation [36]. Negative gene regulation is further classified into two types:

i. Negative gene regulation by inducible operon, and
ii. Negative gene regulation by repressible operon.

In the case of the negative gene regulation by repressible operon, transcription is controlled by *repressor* and *co-repressor* proteins. Generally, only a repressor is present

and it cannot prevent gene transcription alone (i.e. without a co-repressor). When a co-repressor is available, repressor and co-repressor inhibit gene transcription together. During negative gene regulation by inducible operon, gene transcription is repressed i.e. switched off initially. A repressor protein represses transcription unless an inducer molecule is present. In the presence of an inducer molecule, gene transcription is turned ON and RNA transcripts are produced from DNA. In positive gene regulation, a regulatory protein is activated by a small organic molecule that binds to the DNA and turns ON the gene transcription [36]. CMOS models for different types of gene regulations are provided in [22]. Since, all these gene regulation models control RNA synthesis and after the gene regulation control at the transcriptional level; the RNA synthesis process is the same, only negative gene regulation is taken into consideration in this research in order to avoid repetition of the results.

3.3 MATHEMATICAL MODELLING OF GENE EXPRESSION MECHANISMS

An electronic circuit model of the biological gene expression mechanisms discussed above is designed. Initially, mathematical representations of these biological processes are presented. Afterwards, a VLSI circuit model based on the mathematical equations is developed.

3.3.1 Equivalence between Biological Parameters and Electronic Circuit Entities

Representing a gene circuit as an integrated circuit model requires equivalence between biochemical variables and electronic circuit entities. The synthesis and decay of molecules in a biological substrate control the processing of the information that a cell requires. This is analogous to the mechanism of information processing controlled by the transportation of carriers within an electronic system. The chemical concentration of molecules (α) in a gene circuit is comparable to the electrical potential (V) in an integrated circuit. Rate of reaction (χ) and decay rate constant (γ) of the molecular species are similar to electrical current and conductance (1/resistance) respectively. Also, electric charge (q) is similar to the mass (μ) of the molecular species, and hence,

in a gene circuit, capacitance indicates the mass of the biological species that is required to increase the chemical concentration by one unit. The trans-conductance parameter (g_m) of a transistor can be used to represent the rate of transformation of the molecular species from one kind into another [20], [22].

3.3.2 Analogies between Electronic Parameters and the Parameters in miRNA Gene Regulation

The above mentioned biological to electrical parameter equivalences are utilized and mathematical models for the stages of gene expression mechanisms are developed. Let the rate constants for the transcription of gene to RNA be γ_{tc} and the translation of mRNA to protein be γ_{mtl}. Table 3.1 shows the assumed notations for other biological circuit entities.

Table 3. 1. Symbols and units for biological circuit entities utilized in electronic modelling of gene expression stages

GENE EXPRESSION STAGES PARAMETERS				
Biological circuit parameters	**SYMBOL**			
	Concentration $(\alpha)(molL^{-1})$	**Biochemical Capacitance** $(C)\ (gmol^{-1}L)$	**Decay Rate Constant** $(\gamma)(gmol^{-1}Ls^{-1})$	**Rate of Reaction** $(x)(gs^{-1})$
RNA after transcription	α_R	C_R	γ_R	-
mRNA	α_{mR}	C_{mR}	γ_{mR}	x_{mR} (protein translation)
Protein	α_p	C_p	γ_p	-
Pre-miRNA	α_{pre}	C_{pre}	γ_{pre}	-
Pri-miRNA	α_{pri}	C_{pri}	γ_{pri}	-
miRNA	α_{miR}	C_{miR}	γ_{miR}	-
RNA polymerase	α_{rp}	-	-	-
RNA polymeraseII	α_{pol}	-	-	-

By using the variables mentioned in Table 3.1, the resulting equations for the stages of gene expression mechanisms are as follows:

3.3.2.1 RNA Transcription

The rate of change of RNA concentration in a cell is proportional to the sum of:

i. RNA polymerase molecules utilized to transcribe the DNA into the RNA [22]. Mathematically, it is the product of α_{rp} and γ_{tc}
ii. RNA decay (a negative value since it is representing decay) [20],[22]. Mathematically, it is the product of α_R and γ_R . Hence, the rate of change of RNA concentration is (including notations from Table 3.1):

$$\frac{d\alpha_R}{dt} = K_R(-\gamma_R\alpha_R + \alpha_{rp}\gamma_{tc}) \tag{3-1}$$

where K_R is proportionality constant. Electronically, current across a capacitor is $C\frac{dV}{dt}$ and in (3-1) α_R is analogous to voltage, K_R is assumed to be the capacitance reciprocal [22] i.e. :

$$K_R = \frac{1}{C_R} \tag{3-2}$$

C_R represents newly synthesized RNA transcripts storage within a cell. Substituting the value of K_R in (3-1) gives:

$$C_R\frac{d\alpha_R}{dt} = (-\gamma_R\alpha_R + \alpha_{rp}\gamma_{tc}) \tag{3-3}$$

All groups (categories) of RNA (mRNA, tRNA, etc.) are synthesized from DNA by the process of transcription [45]. The RNA decay in (3-3) represents the decay of all groups of RNA molecules except the mRNA (the coding RNA). This is due to the fact that non-coding RNA transcripts are the final gene product, whereas mRNA transcripts are involved in protein synthesis [21]. The decay of the mRNA proceeding towards the protein translation pathway is illustrated in the mRNA degradation and protein translation stages.

3.3.2.2 mRNA Degradation

By back-tracing the biochemical pathway from the mRNA translation (protein formation) towards the transcription stage, the proportional dependencies for the protein formation reaction rate, χ_{mR}, can be approximately given by:

$$\chi_{mR} \propto \alpha_R \tag{3-4}$$

and,

$$\chi_{mR} \propto \left[\frac{1}{\left(\frac{1}{\gamma_{mtl} - \gamma_{mR}} \right) + \left(\frac{1}{\gamma_{miR}} \right)} \right] \tag{3-5}$$

χ_{mR} is directly proportional to the RNA transcripts concentration because protein formation not only depends on mRNA, but also on other types of RNA (rRNA, tRNA) that help in the translation process [21]. The basis for (3-5) is a relationship between protein synthesis (Pr_{synth}) and rate constants (k_1 and k_2) developed by Zinovyev *et al.* in [46], whereby:

$$\mathrm{Pr}_{synth} \propto 1/\left[\left(1/k_1\right) + \left(1/k_2\right) \right] \tag{3-6}$$

The rate constants k_1 and k_2 are species translation and decay rates [47],[48]. The protein formation reaction rate depends on the translation rate and the mRNA decay rate. Thus, $k_1 = \gamma_{mtl} - \gamma_{mR}$ where γ_{mR} is subtracted from γ_{mtl} because decayed mRNA is not available for protein translation [49]. The protein formation reaction rate also depends on the miRNA decay rate because miRNA inhibits mRNA translation; therefore, for the proposed model, $k_2 = \gamma_{miR}$. On combining (3-4) and (3-5) we have:

$$\chi_{mR} = K \left[\frac{\alpha_R}{\left(\frac{1}{\gamma_{mtl} - \gamma_{mR}} \right) + \left(\frac{1}{\gamma_{miR}} \right)} \right] \tag{3-7}$$

Value of the proportionality constant K depends on the fraction of the transcription products (RNA transcripts) which constitute mRNA. By arranging (3-7), the following equation is obtained:

$$\frac{\chi_{mR}}{(\gamma_{mtl}-\gamma_{mR})}=K\left[\frac{(\alpha_R\gamma_{miR})}{(\gamma_{mtl}-\gamma_{mR})+(\gamma_{miR})}\right] \tag{3-8}$$

Next, utilizing the chemical Ohm's law [22] for mRNA, α_{mR} can be expressed as:

$$\alpha_{mR}=\left[\frac{\chi_{mR}}{(\gamma_{mtl}-\gamma_{mR})}\right] \tag{3-9}$$

Substituting (3-9) into (3-8), α_{mR} can be written as:

$$\alpha_{mR}=K\left[\frac{\alpha_R}{1+(\gamma_{mtl}-\gamma_{mR})\left(\frac{1}{\gamma_{miR}}\right)}\right] \tag{3-10}$$

Or,
$$K\alpha_R=\left\{(\alpha_{mR})\left[1+(\gamma_{mtl}-\gamma_{mR})\left(\frac{1}{\gamma_{miR}}\right)\right]\right\} \tag{3-11}$$

By using the analogies between electronic and gene circuit parameters mentioned in section 3.3.1, (3-11) becomes similar to a voltage amplifier gain equation [50].

3.3.2.3 Protein Translation

Similar to RNA transcription, the rate of change of protein concentration in a cell is proportional to the sum of:

i. mRNA transcripts that are translated into the protein [22]. Mathematically, it is the product of α_{mR} and γ_{mtl},
ii. Protein decay (a negative value since it is representing decay) [20],[22]. Mathematically, it is the product of α_p and γ_p. Hence, the rate of change of protein concentration is (including notations from Table 3.1):

$$\frac{d\alpha_p}{dt} = K_p\left(-\gamma_p\alpha_p + \alpha_{mR}\gamma_{mtl}\right) \tag{3-12}$$

where K_p is proportionality constant. Electronically, current across a capacitor is $C\frac{dV}{dt}$ and in (3-12) α_p is analogous to voltage, therefore K_p is assumed to be the capacitance reciprocal [22] i.e. :

$$K_p = \frac{1}{C_p} \tag{3-13}$$

C_p represents newly synthesized protein transcripts storage within a cell. Substituting the value of K_p in (3-12) gives:

$$C_p\frac{d\alpha_p}{dt} = \left(-\gamma_p\alpha_p + \alpha_{mR}\gamma_{mtl}\right) \tag{3-14}$$

3.3.2.4 miRNA Synthesis

Unlike mRNA, primary transcripts of the miRNA are the RNA molecules that are not functional immediately after transcription [21], but the process of formation of these transcripts is similar to the mRNA transcription. Since the synthesis process is the same, the general transcription dynamics given by (3-3) are also applied for primary miRNA synthesis. Let the rate constants for the transcription of the miRNA gene to pri-miRNA be $\gamma_{ptc.}$ Using the notations from Table 3.1, pri-miRNA transcription and pre-miRNA synthesis can be represented as follows:

$$C_{pri}\frac{d\alpha_{pri}}{dt} = (-\gamma_{pri}\alpha_{pri} + \alpha_{pol}\gamma_{ptc}) \tag{3-15}$$

where the term $\alpha_{pol}\ \gamma_{ptc}$ determines rate of reaction for miRNA gene transcription into pri-miRNA. Pri-miRNA is converted into pre-miRNA by the action of the Drosha molecule.

$$\alpha_{pre} = K_{Drosha}\alpha_{pri} \tag{3-16}$$

K_{Drosha} determines the pri-miRNA percentage transformed in pre-miRNA. Slicing of pre-miRNA by the Dicer molecules to produce mature miRNA follows the "law of mass action" [20],[22] given by:

$$\text{Dicer} + \text{pre-miRNA} \rightarrow \text{miRNA} + \text{Dicer} + \text{pre-miRNA} \tag{3-17}$$

The Dicer molecule is not consumed in the miRNA synthesis as it is taking part in the reaction as a catalyst [21]. The rate of change of the miRNA concentration is proportional to the sum of:

i. Pre-miRNA transcripts that are converted into the mature miRNA by the Dicer molecule. Mathematically, it is product of α_{pre} and γ_{dicer},
ii. miRNA decay (a negative value since it is representing decay). Mathematically, it is the product of α_{miR} and γ_{miR}

Hence, (3-17) can be presented in a differential form [20],[22] given by:

$$C_{miR}\frac{d\alpha_{miR}}{dt} = \left(-\gamma_{miR}\alpha_{miR} + \alpha_{pre}\gamma_{dicer}\right) \tag{3-18}$$

where γ_{dicer} is the slicing rate of the Dicer molecule and C_{miR} is the proportionality constant that is the biochemical capacitance corresponding to cellular miRNA storage.

3.3.3 Units for Biological Circuit Entities

Units for biological circuit entities expressed in the mathematical equations presented in section 3.3.2 are determined by following the analogies between biological and electronic circuit parameters [20],[22]. Molarity (M) is the standard unit of chemical concentration (α) which is equal to the number of moles of solute per litre of a solution in mol L^{-1} [51]. A mole contains 6.022 * 10^{23} molecules that is a fixed amount expressed by a universal constant known as the Avogadro's number (N_A). For deriving the unit of biochemical capacitance, mass (μ) in grams of biological species is divided by the concentration (α) in mol L^{-1}, so that the higher molar mass [51] results in a higher storage capacity for the particular species. Rate of reaction (χ), being analogous to current I (=charge/time), can be expressed by the ratio of mass (μ) and time (t) to be μ/t

in gs^{-1}. The decay rate (γ) being analogous to conductance (G) in mho (=I/V), is then expressed by gs^{-1}/mol L^{-1} (= g L/mol s). The resulting units for both sides of equations (3-3),(3-14), (3-15) and (3-18) are then in g/s and hence are consistent. In addition, both sides of the chemical Ohm's law given by (3-9) are also consistent being in mol L^{-1}.

3.4 ELECTRONIC CIRCUIT MODEL MIMICKING GENE EXPRESSION MECHANISMS

Fig. 3.4 shows an electronic circuit model mimicking the mechanisms involved in gene expression stages based on the mathematical equations presented in Section 3.3. Every stage of the electronic model is discussed separately in the following sub sections.

3.4.1 Transcription Control Mechanism

For repressible gene transcription control, repressor (α_{rep}) and co-repressor concentrations (α_{co_rep}) are applied as input to two NOT gates NOT_1 and NOT_2 respectively. These NOT gates operate a NOR gate whose output controls a PMOS switch, S_1. When α_{rep} and α_{co_rep} are HIGH (logic "1") simultaneously, S_1 is OFF which means DNA transcription is not initiated i.e. gene transcription is repressed [22]. For inducible gene transcription control, repressor (α_{rep1}) and inducer concentrations (α_{ind}) are input to a NAND gate. The output of the NAND controls the PMOS switch S_1. When α_{rep1} and α_{ind} are HIGH (logic "1") simultaneously, PMOS is ON and gene transcription is initiated. At any one time, either repressible or inducible transcription control is active for a gene [36].

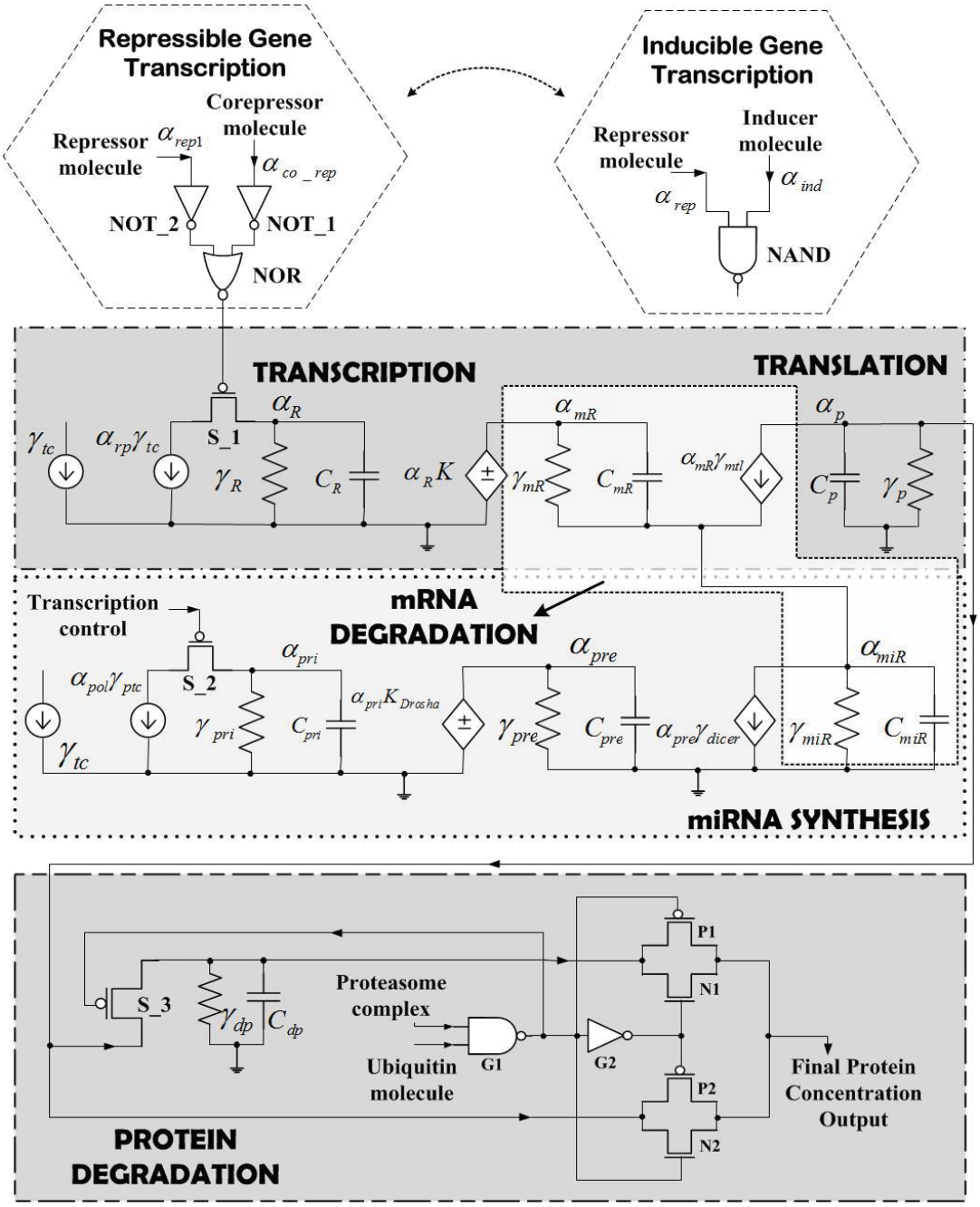

Fig. 3. 4 Electronic circuit model of mechanisms involved in the gene expression stages. All stages are highlighted with in boxes. Repressible and inducible gene regulation mechanisms are also depicted. Either repressible or inducible mechanism is selected at a time to simulate the circuit.

3.4.2 Transcription, Translation and mRNA Degradation

When the switch S_1 is ON, α_R is synthesized from DNA by the action of α_{rp}. γ_R and C_R models RNA decay. Factor K of the voltage source controlled by α_R determines the RNA percentage classified as α_{mR}. mRNA decay within a cell can be represented by

an exponential RC decay circuit [52]. C_{mR} connected in parallel with γ_{mR} models the mRNA decay. By utilizing the analogies between gene and electronic circuit parameters as mentioned in Section 3.3, it is clear that (3-11) becomes equivalent to the following equation:

$$v_{in} = \left\{ v_{\pi} \left[1 + \left(g_m + \frac{1}{r_{\pi}} \right) R_E \right] \right\} \tag{3-19}$$

which represents an expression for the input voltage (v_{in}) in a π-circuit model of the BJT common emitter amplifier with emitter degeneration [53]. In (3-19), v_{π} is the voltage across the base-emitter junction (α_{mR}), the input impedance ($1/\gamma_{mR}$) is denoted by r_{π}, g_m is transconductance of the transistor (γ_{mtl}) and R_E is a resistor attached in series with the emitter ($1/\gamma_{miR}$). The phenomenon of mRNA translation into protein is represented by a voltage controlled current source. Finally, γ_p and C_p models the protein decay.

3.4.3 MiRNA Synthesis

A gene transcription control mechanism (discussed earlier) regulates an MOS transistor switch, S_2, for transcribing a miRNA gene. Pri-miRNA is synthesized when the switch is on. The voltage controlled voltage source models the percentage of α_{pri} that is transformed into α_{pre} by a gain factor of K_{drosha}. The phenomenon of pre-miRNA slicing into mature miRNA by the dicer molecule is represented by a voltage controlled current source in the model because the miRNA concentration depends on action of the Dicer enzyme on pre-miRNA as shown in (3-18). Pre-miRNA and miRNA decays are represented by parallel combinations of "γ_{pre} and C_{pre}" and "γ_{mir} and C_{mir}" respectively. γ_{mir} is common to the mRNA degradation and miRNA synthesis model. In this way miRNA synthesis circuit model is coupled after transcription and before the protein translation stage in Fig. 3.4. Thus, the miRNA carries out the mRNA degradation.

3.4.4 Protein Degradation Process

Protein degradation decision circuitry for the ubiquitin-proteasome pathway [54] is modelled by combined NAND and NOT gates Fig. 3.4. Ubiquitin input at the NAND

gate (G1) having a value of logic "1" means, the synthesized protein is targeted by the ubiquitin molecule for degradation, while a "0" means the newly created protein does not have an attached "*flag molecule*" marker for degradation. The presence or absence of a proteasome complex is represented by a "1" or a "0" respectively, at the other input of G1. For an active protein degradation pathway, the output of G1 is "0" (*active low*) and "1" otherwise. A "0" at G1 output turns on PMOS and NMOS transistors P1 and N1 respectively. PMOS P2 and NMOS N2 are off if degradation is flagged. Thus, the protein concentration after degradation is passed on to the final protein output in this case. P2 and N2 are switched on when G1 gets a "1" at its output. In this case, P1 and N1 are off, therefore, the final protein output is the same as the protein concentration just after translation (i.e., no protein degradation).

The biochemical degradation of the particular protein that is synthesized from mRNA is modelled by an RC exponential decay circuitry [52] formed by connecting γ_{dp} (decay rate constant) and C_{dp} (biochemical capacitance) in parallel. The equivalent protein level after translation is passed to the RC circuit through a PMOS switch (S_3). In the case of protein degradation S_3 is on, while it is off for no degradation.

The electronic circuit in Fig. 3.4 models the interaction between protein coding (mRNA) and non-coding (miRNA) genes. This model bears a resemblance to the π-circuit model of the common emitter BJT amplifier with emitter degeneration [50],[53]. The mature miRNA synthesis process from pre-miRNA is also similar to the π-model of a common emitter BJT amplifier [50],[53]. Table 3.2 shows BJT π-model entities equivalent to the gene expression circuit parameters depicted in Fig. 3.4. Small signal models for NPN and PNP bipolar transistors are the same with no change in polarities [50]. Hence, the BiCMOS equivalent circuit of Fig. 3.4 is developed using PNP as shown in Fig. 3.5. The capacitor C_{ac} in Fig. 3.5 provides the AC ground for equivalence with the small-signal equivalent model for miRNA in Fig. 3.4.

Table 3. 2. Electronic gene expression circuit parameters and BJT π-model parameters entities analogy taken from [50]

S.No.	Gene Expression Circuit Parameters for mRNA and miRNA gene	BJT π-model equivalent Entities
1.	α_{mR}, α_{pre}	Base-emitter potentials
2.	α_{p}, α_{miR}	Collector-emitter potentials
3.	γ_{mR}, γ_{pre}	Input conductances
4.	γ_{p}, γ_{miR}	Output conductances
5.	C_{mR}, C_{pre}	Base-emitter junction capacitances
6.	C_{p}, C_{miR}	Collector-substrate junction capacitances
7.	γ_{mtl}, γ_{dicer}	Transconductances

Since the miRNA decay rate constant (γ_{miR}) is attached to the bottom of the translation model, the two BJT models in Fig. 3.4 are shown cascoded in the transistor diagram of Fig. 3.5. For this cascode topology, the emitter resistance of the BJT amplifier with emitter degeneration (Q1) is provided by the collector resistance of the common emitter amplifier (Q2) Fig. 3.5. M1 and M2 transistors make a current source in Fig. 3.5 which multiplies the RNA transcription rate (γ_{tc}) by RNA Polymerase II concentration (α_{rp}). Similarly, M3 and M4 transistors form another current source which multiplies the miRNA transcription rate (γ_{ptc}) with RNA polymerase concentration (α_{pol}) transcribing the miRNA gene. Bipolar transistors Q3 and Q4 form a bias current source for the circuit.

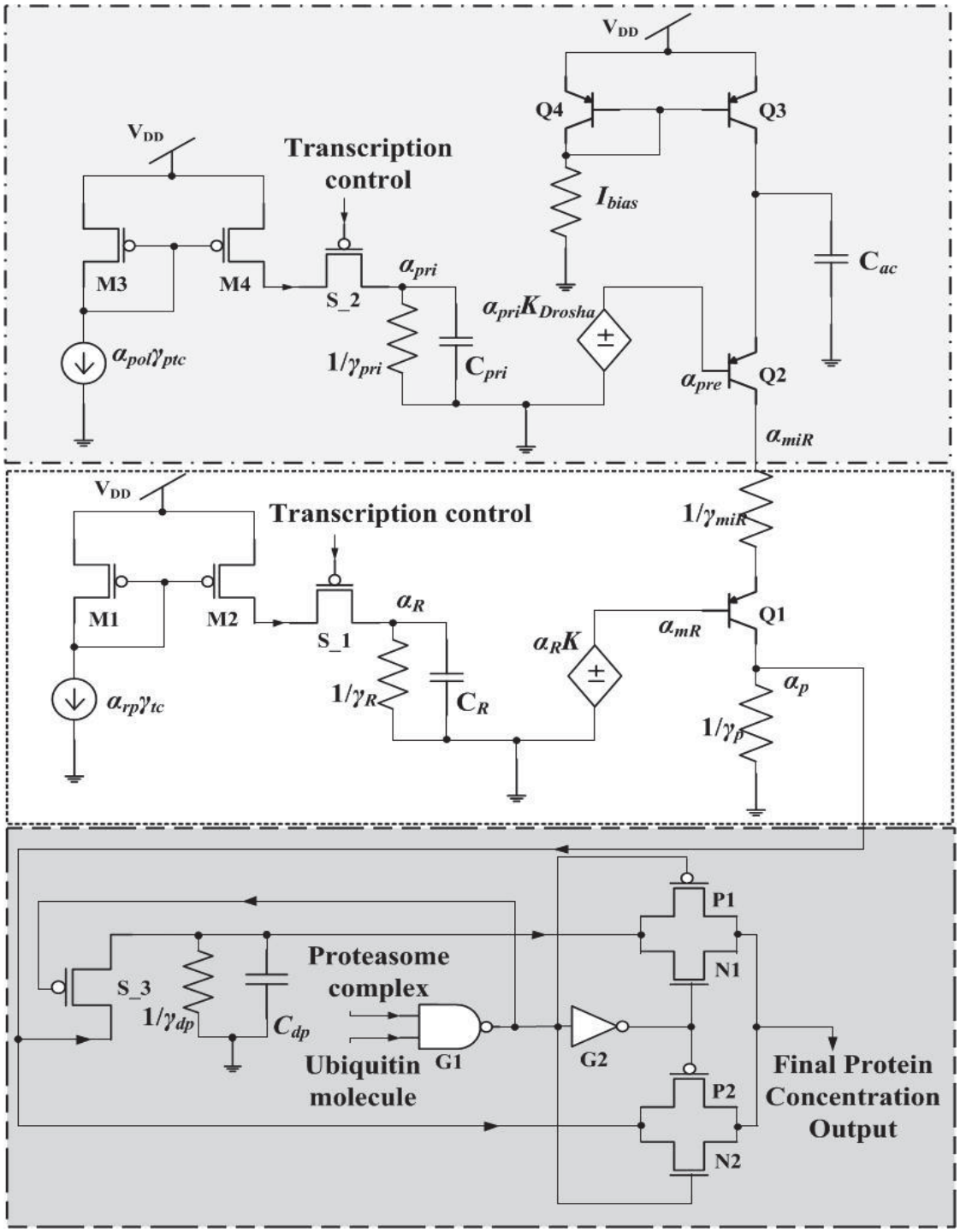

Fig. 3. 5 The equivalent BiCMOS electronic circuit of the gene expression using PNP transistors. $\alpha_{rp}\gamma_{tc}$ controls the reaction rate of RNA transcription from DNA when S_1 is ON. mRNA concentration (α_{mR}) is K times RNA concentration (α_R). α_{mR} is Q1 base input voltage and its output collector voltage is synthesized protein α_p. α_p is controlled by Q2 output at collector, i.e. miRNA concentration (α_{miR}). Q2 base voltage is premiRNA concentration (α_{pre}) which depends on amount of primiRNA (α_{pri}) transformed into α_{pre} by K_{drosha}. α_{pri} is transcribed from the gene with a reaction rate of $\alpha_{pol}\gamma_{ptc}$. Q3 and Q4 form a current source for biasing the circuit.

3.5 RESULTS AND DISCUSSIONS

Fig. 3.5 is simulated in *Mentor Graphics* software. Circuit parameter values and simulation results of the cytomorphic circuit model are elaborated in this section. Monte Carlo analysis is performed to prove robustness of the circuit. Circuit design validation is carried out by comparing electronic simulation outcomes with biological experimentally reported data.

3.5.1 Circuit Parameter Values

The input electric potentials of 1.2 V and 0 V are used to represent logic "1" and logic "0" states respectively for the proteasome complex and ubiquitin molecule concentrations. Repressor (α_{rep1}) and corepressor (α_{co_rep}) concentrations control repressible gene transcription, while repressor (α_{rep}) and inducer (α_{ind}) concentrations control inducible gene transcription [36]. Input voltage sources for (α_{rep1} and α_{co_rep}) or (α_{rep} and α_{ind}) [one transcription regulation scheme is simulated at a time for a gene] are taken as pulsations of 1.2 V and 0 V with a pulse period of 0.2µs. The high and low values of the pulse represent the presence or absence of these molecules. A pulse period is selected randomly. It can be more or less since it only changes the output signal frequency. V_{DD} is set to 1.2V (for 0.13µm technology [55]). Considering that vast portions of DNA consist of non-coding genes, the percentage of RNA transcripts attributable to the mRNA (protein coding) concentration is 30% in living cells of larger organisms such as humans, while 80% of RNA results in mRNA in smaller organisms such as bacteria [56]. Since, the electronic model proposed in this chapter is generalized to represent the gene expression mechanisms taking place inside various organisms (irrespective of the organism type); an average value of 55% (RNA attributable to mRNA) is considered and the transcription constant K is set to a fractional value of 0.55 for the gene model. K_{Drosha} is set to 1 assuming that all pri-miRNA are transformed into premiRNA transcripts.

A BJT current mirror formed by *Q3-Q4* PNP transistors is used for DC biasing. After iterative simulations, $\alpha_{rp}\gamma_{tc}$ and $\alpha_{pol}\gamma_{ptc}$ are set to 5mA each and 100Ω value is chosen for R_{bias} in order to ensure that BJT amplifier transistors are in active mode (necessary for transistor to act as an amplifier [50],[53]). A minimum default MOS

channel width to length ratio 0.16µm/0.13µm (for 0.13µm technology) is set for all MOS transistors. γ_R and γ_{pri} are assigned a value of 0.05mS, while capacitances are set to 0.1 nF. A 0.5mS value is chosen for γ_p , while γ_{miR} is 0.01S.

3.5.2 Simulation Results

The presence of miRNA strands degrades mRNA transcripts, thus with an increase in the concentration of miRNA, the mRNA translation is affected, thereby resulting in reduced protein concentration. This behaviour is observed when the electronic circuit model of gene expression depicted in Fig. 3.5 is simulated. Fig. 3.6 demonstrates the phenomenon of mRNA degeneration through an inverse relationship between the miRNA concentration and the protein concentration.

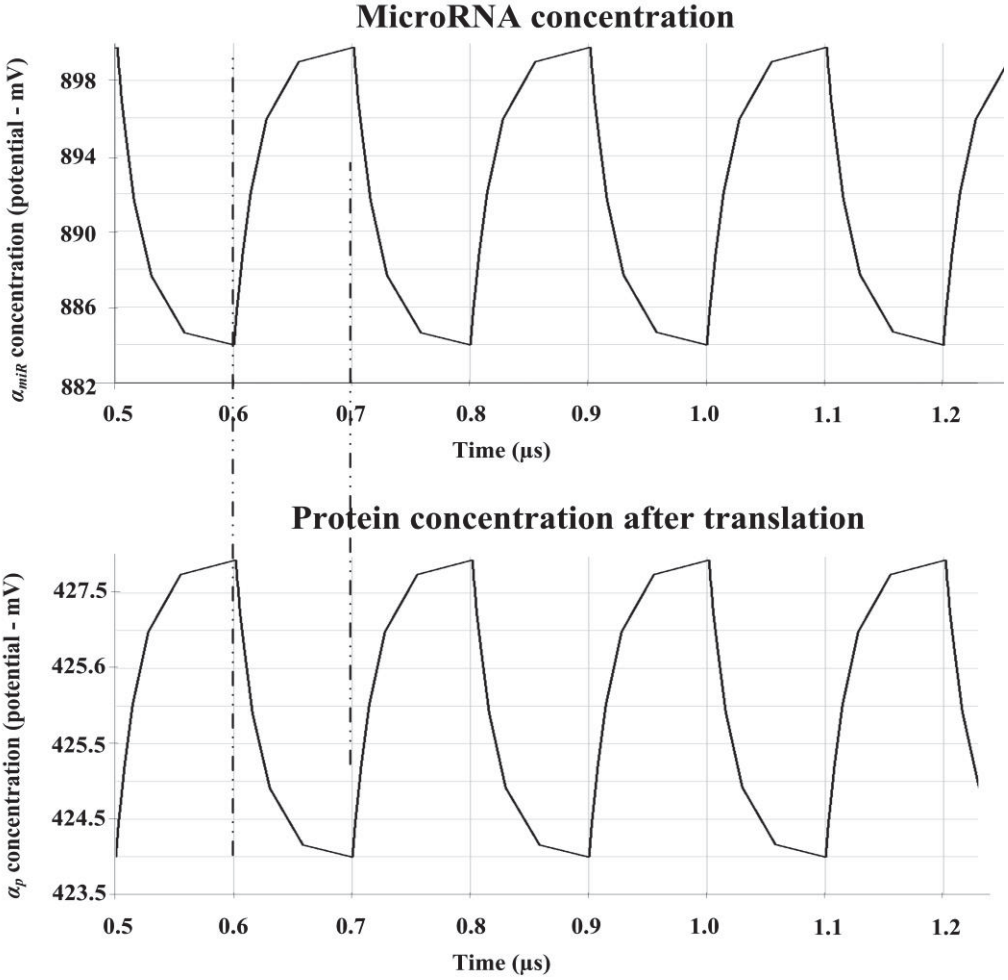

Fig. 3. 6. Simulated miRNA and protein concentrations (potentials). The dotted vertical lines indicate the simulated effect of miRNA concentration on protein. Upper plot: miRNA concentration (α_{miR}), lower plot: protein concentration after translation (α_p). Potentials are taken on x-axes, while time scales are plotted on y-axes.

The upper plot depicts the miRNA concentration, α_{miR}. The protein concentration after translation, α_p is shown in the lower plot of Fig. 3.6. α_{miR} and α_p are expressed in mV on the y-axes of upper and lower plots respectively. The time scale is in µs. α_{miR} and α_p have a time period of 0.2 µs each because gene transcription control time periods for both miRNA and mRNA genes are 0.2 µs. It is clear from the simulated output that an increase in α_{miR} lessens the protein translation, resulting in α_p being reduced and vice versa, as shown by vertical dotted lines in Fig 3.6. Fig. 3.7 depicts the final protein concentration outputs of the gene expression model after the translation and degradation stages.

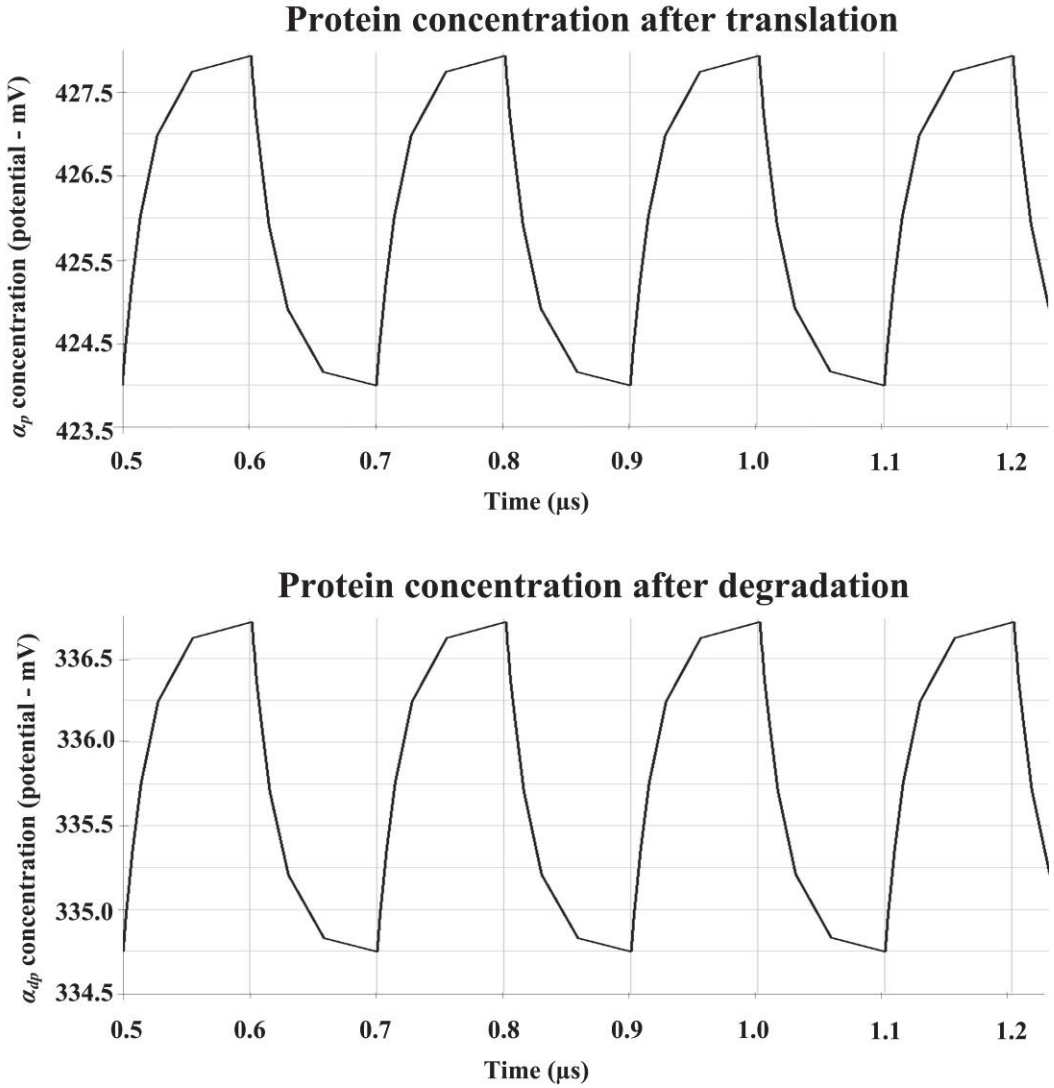

Fig. 3. 7. Simulated final protein concentrations after translation and degradation stages. Upper plot: protein concentration after translation, lower plot: protein concentration after degradation. For protein degradation output, ubiquitin and proteasome inputs are high (1.2V), while for protein translation these inputs are low (0V).

When proteasome and ubiquitin inputs are low, switch S_3 is off and the final protein concentration is the same as the translated protein concentration. On the other hand, the presence of proteasome and ubiquitin at the same time causes protein degradation by turning on S_3. As shown in Fig. 3.7, the protein degradation is noticeable by a decrease in the output potential (protein concentration level) in the presence of the proteasomic mechanisms compared to the "no protein degradation" processes. The upper plot depicts a protein concentration after translation. The protein concentration after degradation is shown in the lower plot of Fig. 3.7. Protein concentrations are in mV, while the time scale is in μs for both plots of Fig. 3.7.

3.5.3 Robustness of the Composite Gene Circuit Model

At the gene level many biochemical reactions are stochastic due to random process variables. Thus, in order to verify the robustness of the simulated electronic gene circuit model in an environment of stochastic parameter variations, Monte Carlo analysis is carried out. Biochemical capacitances, decay rates and transistor operations are swept in this Monte Carlo simulation. A built-in Gaussian probability distribution function is selected during the simulation to explore the stochastic process [57]. Fig. 3.8 depicts the effect of miRNA on the protein level through this Monte Carlo analysis set-up. It is clear from this figure that even after stochastic variation in the model components, cellular protein concentration is inversely proportional to the miRNA concentration as illustrated previously.

In Fig. 3.9, protein levels with and without degradation are shown after stochastic variations. Translated protein concentration is higher as compared to degraded protein during the Monte Carlo analysis. This proves the robustness of the proposed electronic gene circuit model in an environment of stochastic biochemical variations.

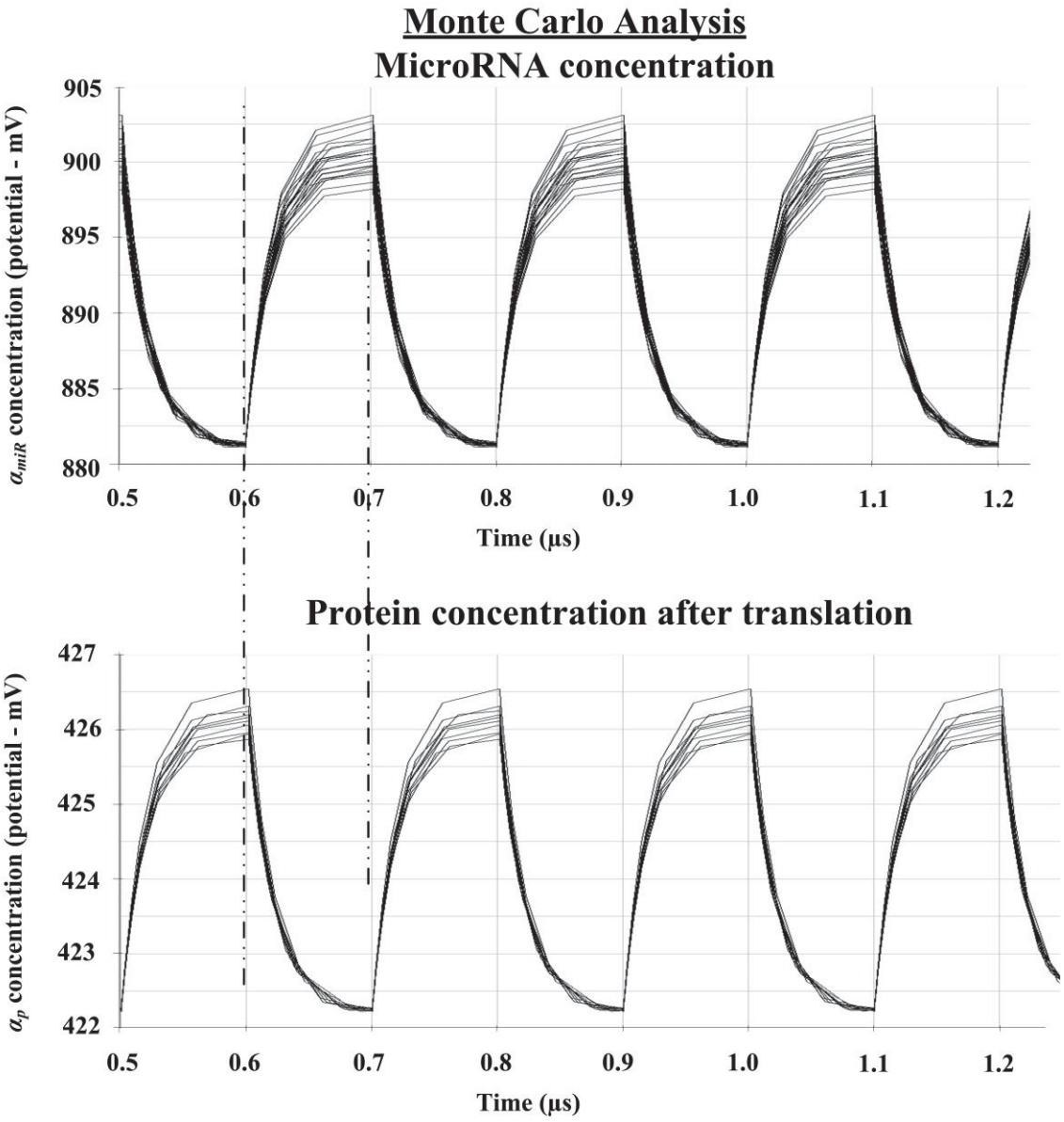

Fig. 3. 8. Monte Carlo simulation illustrating stochastic effect of the miRNA on the protein level. Gaussian probability distribution function is selected for varying circuit parameters of Fig. 3.5. Vertical dotted alignments show the inverse relationship between α_{miR} and α_p.

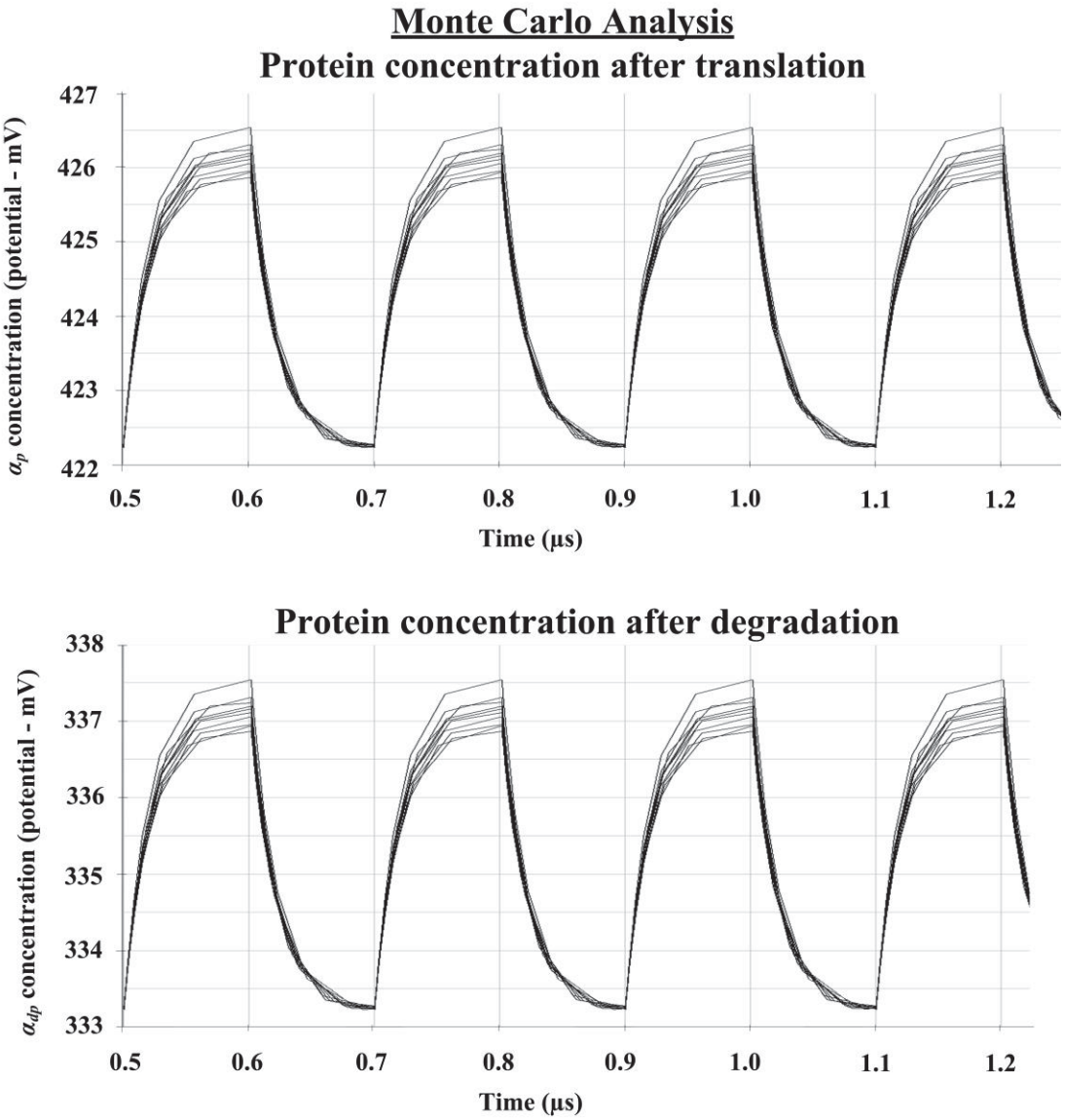

Fig. 3. 9. Monte Carlo simulation illustrating protein concentration after translation (without degradation) and after degradation stages of gene expression. Gaussian probability distribution function is selected for the varying circuit parameters of Fig. 3.5.

3.5.4 Scaling and Calibration of Axes Quantities

The voltage to concentration conversion and electrical time to biological time scaling are carried out as follows:

3.5.4.1 Time Scale

The time domain of a staged gene expression process is characterized by a circadian clock [58]. Gene expression mechanisms are synchronized by the circadian

rhythms having a period of approximately 24 hrs [58], [59]. Within each circadian period, the DNA expression mechanism engages at least one gene that transcribes mRNA from which a protein is translated. It is also noted that synthesized protein takes part in negative feedback on the gene expression mechanism from which that protein was originally generated [59] thus affecting the circadian rhythm as a consequence. The time scale of cellular biochemical process dynamics is thus slower compared to the faster SPICE time scale in μs. Hence, in order to scale and calibrate the SPICE based simulation for the gene expression integrated circuit model of Fig. 3.5 into cellular dimensions, let τ_{cp} and τ_e be respectively the circadian and the electrical time periods. Also, let τ' be the scaling factor for converting an electrical period into a cellular cycle. τ_{cp} is 24 hr and τ_e is set to 0.2 μs because gene transcription control has a pulse period of 0.2 μs as can be seen in Fig. 3.6 and Fig. 3.7. By applying the common unitary calculation method, τ' is given by:

$$\tau' \approx \frac{\tau_{cp}}{\tau_e} = \frac{24hr}{0.2\mu s} = 120hr/\mu s \qquad (3\text{-}20)$$

The biological time span is obtained by multiplying the electrical time scale with τ'. Although the various gene expression periods may vary and fluctuate in the biological time scale, a common biological time base is used to compare the concentration variation of different gene products that interact. Complex processes of the gene expression cycle such as transcription, translation, protein-protein interactions, and protein degradation occur within the molecular time cycle, the "*circadian clock*" [60]; therefore, cellular biochemical quantities are compared on this 24 hr periodic time scale.

3.5.4.2 Voltage Scale

There are $2.6*10^9$ proteins in a cell [61]. $4*10^6$ proteins are translated per minute [61]. Thus total translated protein level in 24 hr is $5.76*10^9$, but after degradation and utilization of protein for other processes with in a cell, the final protein amount after 24hr is maintained at $2.6*10^9$ [61]. A mole contains $6.022 *10^{23}$ molecules, a fixed amount expressed by Avogadro's number (universal constant) [51],[62]. The protein amount ranges from $4.32*10^{-15}$ moles to $9.6*10^{-15}$ moles in a cell (calculated by dividing total amount of protein by Avogadro's number). Concentration expressed in molarity is the number of moles of solute per litres of solution. Intracellular volume is $4*10^{-12}$ litres [63]. Thus protein concentration lies in a range of 1.1mM ($4.32*10^{-15}$/

$4*10^{-12}$) to 2.4mM ($9.56*10^{-15}$/ $4*10^{-12}$) in a 24 hr time cycle. miRNA concentration lies in a range of 0 – 0.025nM [64].

Simulated protein concentration is 424 mV to 428 mV, while miRNA concentration ranges from 884 mV to 900 mV. These voltage values are scaled to the corresponding concentration scale by using the following formula [65],[66]:

$$C(val) = \frac{C_{\max} - C_{\min}}{V_{\max} - V_{\min}}\left(val - V_{\min}\right) + C_{\min} \tag{3-21}$$

where *val* is voltage value for which the concentration is to be determined, C_{max} and C_{min} are maximum and minimum concentration value respectively. V_{max} and V_{min} are maximum and minimum voltage scale values respectively. In Fig. 3.10, an inset view from Fig. 3.6 is depicted. Voltage and electrical time scale are scaled to concentration and biological time scale respectively by following the method discussed in this subsection. The miRNA level is shown on the left y-axis of Fig. 3.10, while the protein level is illustrated on the right y-axis. Potential value is followed by its biologically analogous parameter i.e. concentration. On the x-axis, both electronically simulated time and biological time scales are depicted.

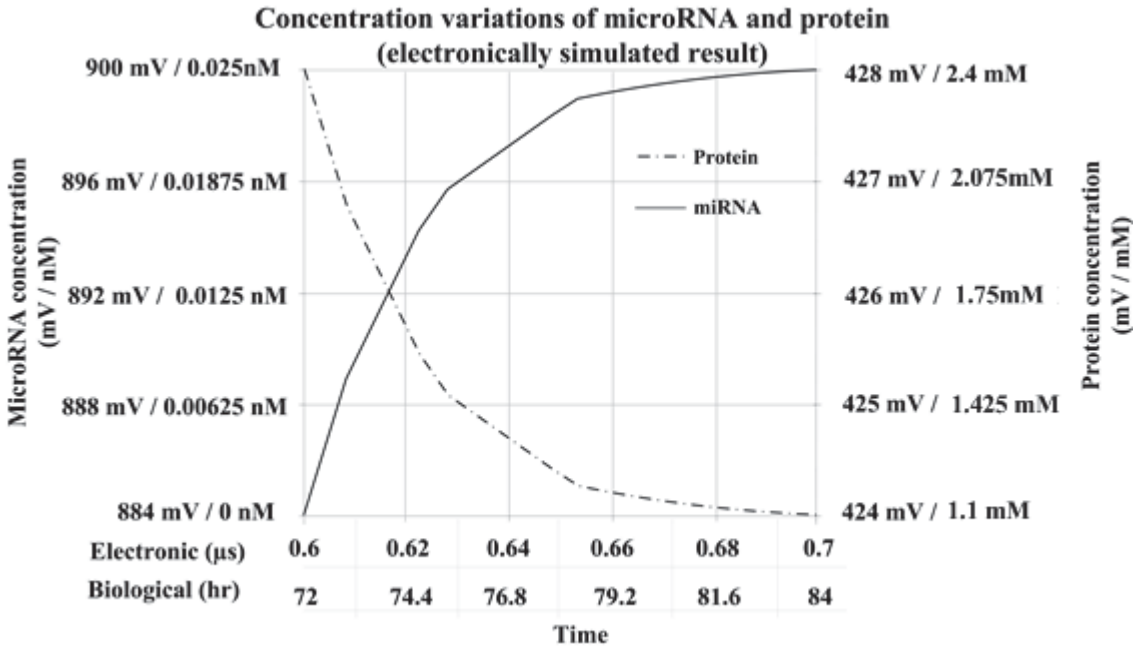

Fig. 3. 10. Inset views of electronically simulated protein and miRNA concentrations from Fig. 3.6. miRNA and protein levels are shown on left right y-axes respectively. Potentials are scaled to a biologically analogous parameter, i.e. concentration. Electrical time is also scaled to a biological time period.

3.5.5 Comparison between Electronically Simulated Outputs and Experimentally Reported Data

As the miRNA concentration (potential) increases, the protein concentration (potential) decreases and vice versa. These simulation results from the electronic gene expression model are similar to the actual biological gene expression process of mRNA degradation by miRNA [67],[68],[69]. Researchers in [69] carried out experiments to quantify *miR-133* (miRNA gene) and *henna gene protein* levels in a biological medium. They observed an inverse relationship between *miR-133* and *henna protein* concentrations. Increase in *miR-133* concentration forced the *henna protein* level to decrease [69]. Similarly, the researchers experimentally observed decrease in *miR-133* concentration followed by an increase in the *henna protein* concentration [69]. The electronically simulated protein-miRNA concentration relationship in Fig. 3.6 is comparable with the experimentally derived graph reported in [69], as shown in Figs. 3.11 and 3.12. Protein and miRNA concentrations were experimentally measured and expressed in terms of relative expression [69]. Relative expression is determined through the relative expression quantification method [70]. In this method, the target transcripts are treated with different chemicals and their levels are compared with the untreated controlled transcripts [70]. In Figs. 3.11 and 3.12, there are two different plots in each figure. One graph shows the comparison between the electronically simulated and the biologically observed miRNA concentration, while the other graph illustrates the electronically simulated and the biologically observed protein concentration. In Figs. 3.11 and 3.12, the electronically simulated concentration levels (scaled from voltage to Molarity as discussed in section 3.5.4) are shown on left y-axes and their graphs are plotted by solid lines, while the biologically observed concentrations in terms of relative expression are illustrated on the right y-axes and their graphs are plotted by dotted lines. In Figs. 3.11 and 3.12, electronic time durations (scaled from μs to hrs as discussed in section 3.5.4) are mentioned on the lower x-axes, whereas the biological time durations are mentioned on the upper x-axes. In the biological experiment, the input bio-chemicals were injected into the cell and the cell behaviour were observed after several hours. As a result gene transcription was not stopped for during that time duration until negative control was applied to control the transcription process. On the other hand, the simulation results have accurate time period of ‘ON’ and ‘OFF’ transcription states. Due to this reason the biological time scale is not as accurate as the

simulation time scale. In Fig. 3.11, the effect of increasing miRNA level on the protein concentration is depicted.

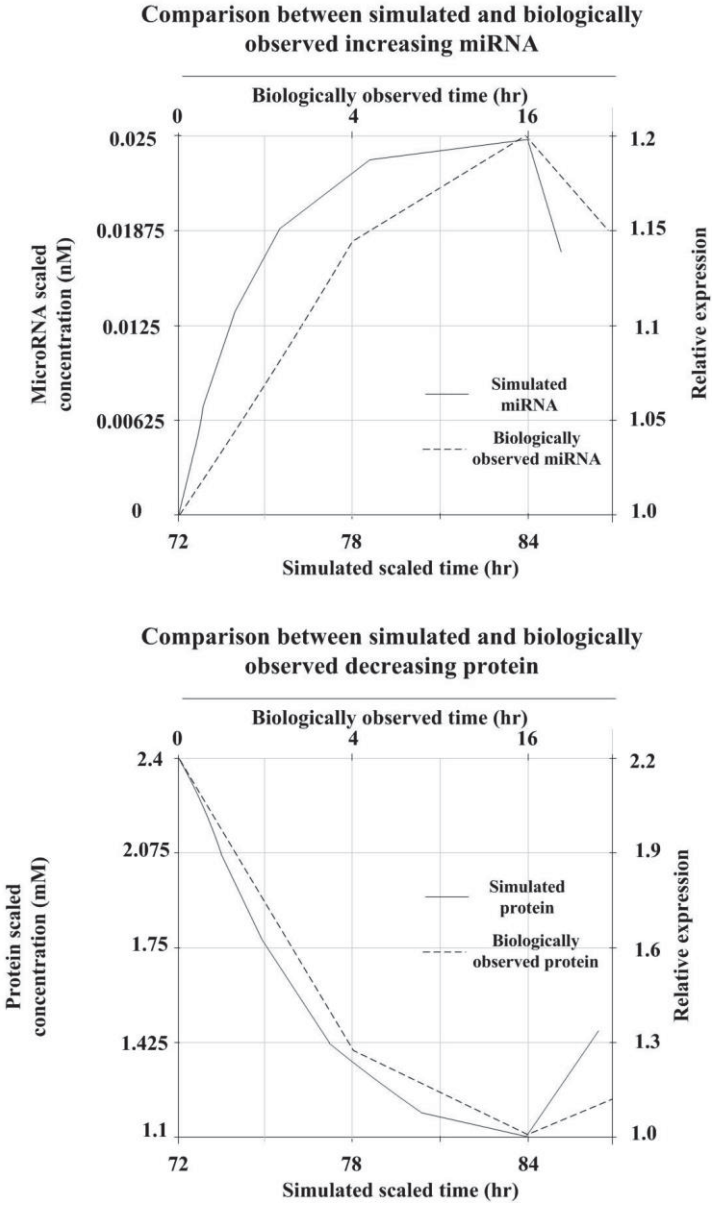

Fig. 3. 11. Comparison between the electronically simulated and experimental biological results for miRNA (upper plot) and the protein (lower plot) concentrations. Solid lines indicate the electronic results that are generated from the electronic cytomorphic circuit of the gene expression mechanisms, while the dotted lines indicate the biologically observed results that are taken from the research mentioned in [69]. These two plots also show the effect of increasing miRNA concentration on the translated protein level. Protein level is high in the absence of miRNA. Once miRNA is transcribed, mRNA translation was affected ultimately resulting in a decrease in protein concentration.

As the miRNA concentration increases, it starts to degrade mRNA due to which translation is repressed and the protein level starts to fall. In Fig. 3.12, the effect of decreasing miRNA level on the protein concentration is shown. Lower level of miRNA

is not sufficient to stop the mRNA from protein translation, as a result the protein concentration rises. It can be seen from Fig. 3.11 and Fig. 3.12 that the electronically simulated and biologically observed responses are similar and the inverse relationship between the miRNA and the protein concentrations is also the same.

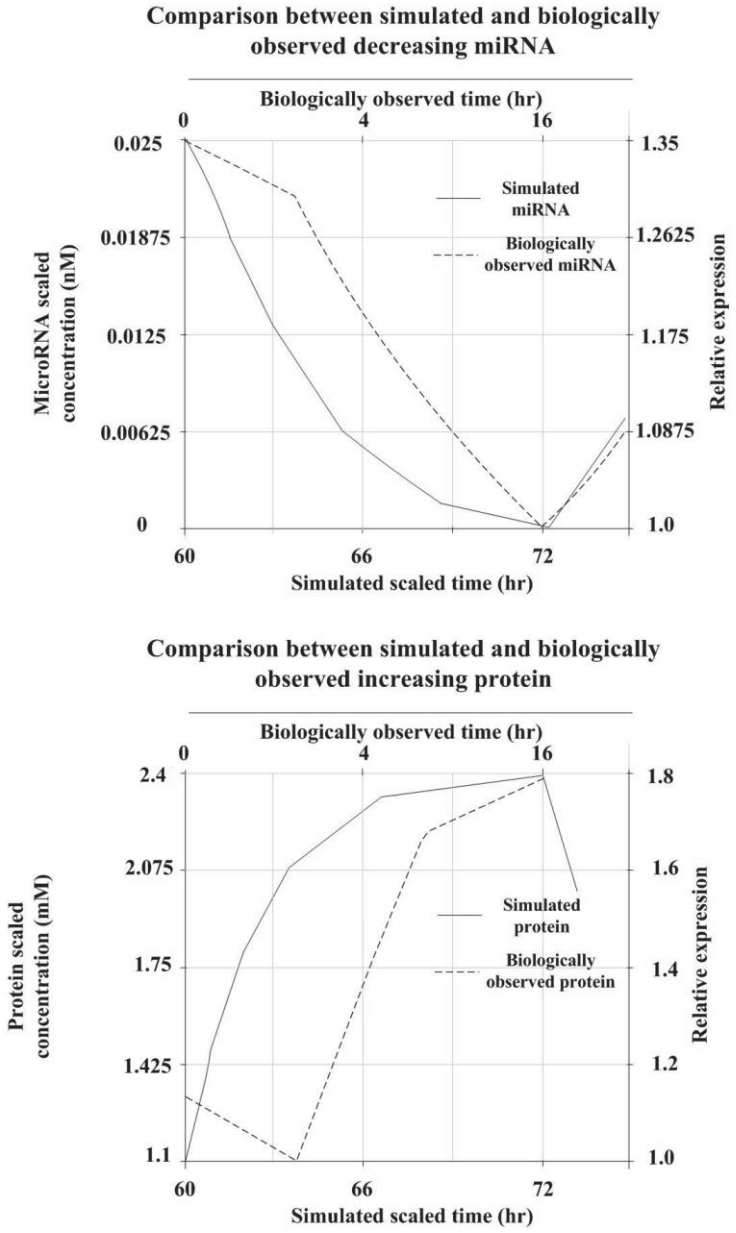

Fig. 3. 12. Comparison between the electronically simulated and experimental biological results for miRNA (upper plot) and the protein (lower plot) concentrations. Solid lines indicate the electronic results that are generated from the electronic cytomorphic circuit of the gene expression mechanisms, while the dotted lines indicate the biologically observed results that are taken from the research mentioned in [69]. These two plots also show the effect of decreasing miRNA concentration on the translated protein level. Protein level is low when miRNA level is high. When miRNA starts to decrease, mRNA translation was affected ultimately resulting in a decrease in protein concentration.

The simulated response of an electronic gene circuit model and an experimentally reported response are similar. Moreover, the experimental time duration is 16 hrs [69] and the biologically scaled time duration of the gene circuit is 12 hrs. This difference is because electronic μs scale is normalized to an average scale of 24 hours that can vary a bit depending on the experimental conditions and the biological medium. Considering that the experimental concentration in [69] using relative expression quantification is an approximate value, and that the quantitative estimates of cellular species even in experimentally studied biological systems are not completely accurate [22],[59],[71], this comparison of an experimental graph with a simulation is validating the correct functioning of the gene expression model.

The post translation gene regulation by the ubiquitin-proteasome pathway was experimentally verified in [72],[73] for a protein called "survivin." On insertion of a proteasome inhibitor within a cell, a higher concentration level of protein is observed as compared to the protein concentration in the absence of the inhibitor, which confirms that survivin is degraded by the ubiquitin-proteasome pathway [72],[73]. Fig. 3.13 is a bar chart showing the relative survivin (protein) amount with degradation and without degradation (due to the presence of the proteasome inhibitor) from experimentally reported data in [72],[73]. Survivin was observed through immunoblotting experiments. The species level appears as light or dark lines in immunoblots corresponding to comparative low or high levels respectively [72],[73]. Hence, the protein level on the bar chart of Fig. 3.13 is expressed as a comparative scale of low and high. Fig. 3.14 is another bar chart illustrating the simulation results of the electronic gene model for a relative protein concentration (voltage) after translation (without degradation and with degradation). Similar to experimental data, simulated protein levels are expressed in terms of comparative low and high scales. Comparison of the two bar diagrams validates the electronic gene circuit model, particularly considering the quantitative uncertainty of biocellular species even in experimentally verified systems [22],[59],[71].

The Monte Carlo analysis as illustrated in Fig. 3.8 is also in agreement with the experimentally reported inverse relationship between miRNA and protein concentrations as shown in Figs. 3.11 and 3.12. Moreover, protein concentrations with and without the degradation of the Monte Carlo simulations in Fig. 3.9 are also following experimental behaviour.

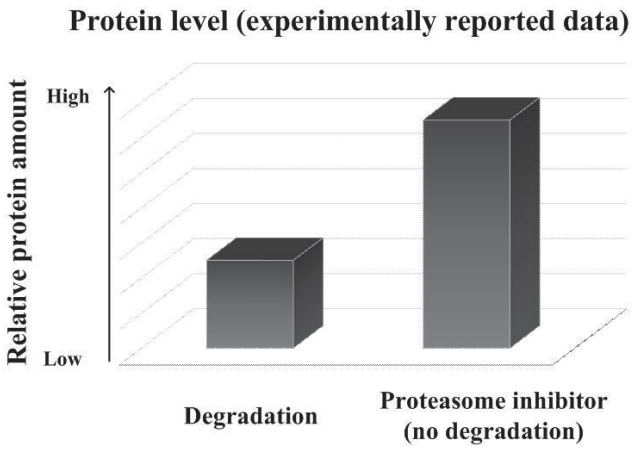

Fig. 3. 13. Relative protein level from experimentally reported data as mentioned in [72],[73] with and without degradation. For observing protein level without degradation, proteasome inhibitor was injected in the cells under observation.

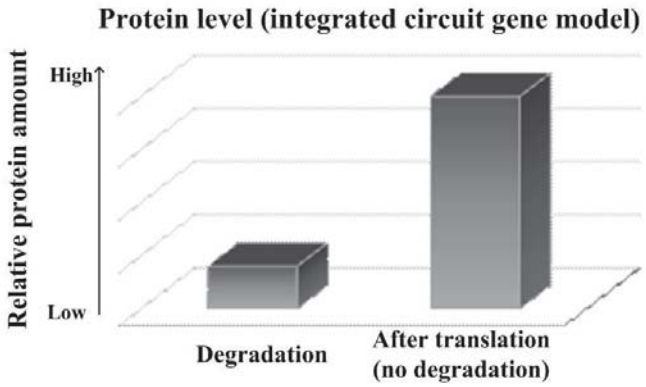

Fig. 3. 14. Relative protein concentration output of gene expression circuit model before and after the protein degradation process.

3.6 CONCLUSION

A robust VLSI circuit model has been presented for the stages in the regulation of the gene expression mechanisms within a living cell. Details of the biological mechanisms involved in gene expression stages have been explored. Analogies between gene circuit parameters and electrical circuit entities are applied to develop an electronic model which mimics the process of gene expression. An electronic model of protein synthesis from mRNA and mRNA degradation by miRNA resembles the π-model of a common emitter BJT amplifier with emitter degeneration. Mature miRNA synthesis from pre-miRNA mimics a common emitter BJT amplifier π-model. Simulation results

are provided as a proof of the appropriate functionality of the integrated circuit model in correspondence with biological domain entities. Simulations with random fluctuations in the circuit model entities due to the stochastic biochemical reactions are also performed through Monte Carlo analysis. The simulation results agree with the reported experimental outcomes of gene expression stages, considering that, quantitatively, there is wide variation in the concentrations of molecular species within the mechanisms of biocellular processes. By modelling particular genes and their products, together with parts of genetic networks and biochemical pathways, the objective of understanding complex genetic activities and biological processes can be enhanced [74].

CHAPTER 4
ELECTRONIC CIRCUIT MODELLING OF NEURAL SYNAPTIC TRANSMISSION PROCESS

4.1 INTRODUCTION

Hodgkin and Huxley in [27], and Morris and Lecar in [75] developed two well-known electronic models of a neuron membrane in which the flow of Na^+, K^+ and Ca^{2+} ions across the membrane were modelled by variable resistors. Chua [31] proposed that Na^+ and K^+ ions conductance across ion channels are analogous to a time-invariant voltage controlled memristor. Following Chua's approach, this chapter shows modelling of the Ca^{2+} ions variable conductance through a neuron membrane as a time invariant voltage controlled memristor. Several neuron electronic circuits have been developed by different researchers in the past. Some of the significant circuits are hardware implementation of spiking neurons [13], voltage dependent ion channel analog circuit [76] and bio-physically inspired silicon neuron [77]. Moreover, memristor based synapse circuits have also been developed [78], [79], [80]. Development of these innovative electronic circuits diversifies neuromorphic field into *memristor based neuromorphic* research that utilizes memristors for mimicking the neural biological mechanisms. Inspired by these remarkable neuromorphic researches, this chapter presents a complete *biomimetic* circuit model for the bio-molecular mechanisms occurring during the chemical synaptic transmission between two neurons (*a neuromorphic circuit at the molecular level*). Synaptic transmission is a process in which neurons communicate among each other through synapses [81] using bio-molecular signals. It is an extremely complex and vital process dealing with brain functionality [28]. The circuit is capable of generating excitatory currents, potentials and summed excitatory potentials. The summed potential is essential to propagate the neuron-to-neuron communication process. Ca^{2+} ions conductance through ionic channels (across a neuron membrane) is essential for transmission initiation [28]. Ca^{2+} ions conductance can be modelled by a memristor. Unlike other circuit elements such as resistors, capacitors, etc., memristor is not supported by simulation software due to its novelty. Several researchers have proposed memristor models [82], [83], [84]. The model proposed by Hyongsuk *et al.* (Chua, pioneer of the memristor concept is one of

the co-authoer) in [82] is modified for 0.13μm VLSI technology and is used to represent Ca^{2+} ions conductance in this research.

4.2 TRANSMISSION AT SYNAPSE – BIOLOGICAL PROCESS

At rest, the neural cell membrane maintains a constant voltage across it, known as the *resting membrane potential*. External stimuli can either increase or decrease the potential across the cell membrane. The earlier phenomenon is known as *hyperpolarization* and the later one is known as *depolarization*. In the depolarization state, a certain membrane voltage is known as the *threshold potential*. When a triggering stimulus causes the membrane to depolarize above the threshold, an action potential is generated [28]. An action potential is a rapid and transient electrical impulse which occurs as an all-or-none signal. The external stimulus does not affect the magnitude of the action potential. It is the frequency of the action potential which increases with (is *modulated* by) a rise in amplitude or duration of the stimulus [28],[36].

Electrical signals are communicated through neurons over long distances within the nervous system. The information conveyed by the action potential is communicated from one neuron to the succeeding neuron via *synapses*. A biological representation of the neural synaptic transmission process that occurs between the presynaptic and the postsynaptic neurons is illustrated in Fig. 4.1 [28],[29],[85]. For circuit modelling, the synaptic transmission biological phenomenon is divided into several stages. These stages are discussed in the following sub sections.

4.2.1 Presynaptic Neuron

When the presynaptic neuron receives an action potential signal, the membrane potential is changed. Extracellular Ca^{2+} ions penetrate into the neuron through voltage dependent Ca^{2+} ionic channels which open due to the membrane depolarization. Flow of ions from the exterior to the interior of the neuron (ion current into the neuron) is due to the higher external Ca^{2+} concentration, as compared to the internal concentration at rest. As a result, the presynaptic neuron releases neurotransmitters at the synapses. These neurotransmitters are chemical messengers stored in synaptic vesicles present inside the neuron membrane.

During the transmission process, neurotransmitters' secretion at the synapses is accountable for the neuron to neuron communication [28],[85]. There are different types of neurotransmitters based on their chemical composition such as acetylcholine (ACh), glutamate, and dopamine neurotransmitters. Each type of neurotransmitter (signal molecule) has different functionalities and receptors (capture molecules) at the postsynaptic neuron membrane and has a different function [29]. In this chapter ACh neurotransmitters are taken into consideration, while the role of glutamate neurotransmitter is discussed in later chapter.

During the synthesis of ACh, choline reacts with acetyl coenzyme A (acetyl CoA) in an enzymatic reaction. In this reaction choline acetyltransferase (CAT) acts as a catalyst. After synthesis, ACh neurotransmitters are stored in vesicles within the presynaptic neuron [28],[85]. In contrast to other ions, Ca^{2+} ions are more effective at releasing neurotransmitters [86]. Hence, a substantial accumulation of Ca^{2+} ions inside the presynaptic neuron causes the synaptic vesicles to fuse at the membrane and release ACh into the synaptic cleft [29],[87].

4.2.2 Postsynaptic Neuron

Ligand-gated ion channels are opened at the postsynaptic neuron when ACh attaches to specific receptors. Ligand-gated ion channels are the channels that are opened by the action of ligand, i.e., chemical messengers to allow flow of ions. Here, neurotransmitters act as ligands [28]. As a result, ionic flow takes place and produces *end plate current* (***EPC***) which either depolarizes or hyperpolarizes the postsynaptic neuron. Ionic conductance occurs through voltage-gated ion channels permeable to particular ions (Na^+, K^+, Cl^-, Ca^{2+}) due to which the neuron membrane potential changes. This potential is known as *excitatory postsynaptic potential* (***EPSP***) if it contributes to generation of the action potential and further continuation of neuron-to-neuron communication. The opening and closing states of ligand-gated channels are controlled by neurotransmitters (i.e. ligand) attachment with receptors present on these channels, while for voltage-gated channels these states are controlled by a change in membrane voltage [28],[87].

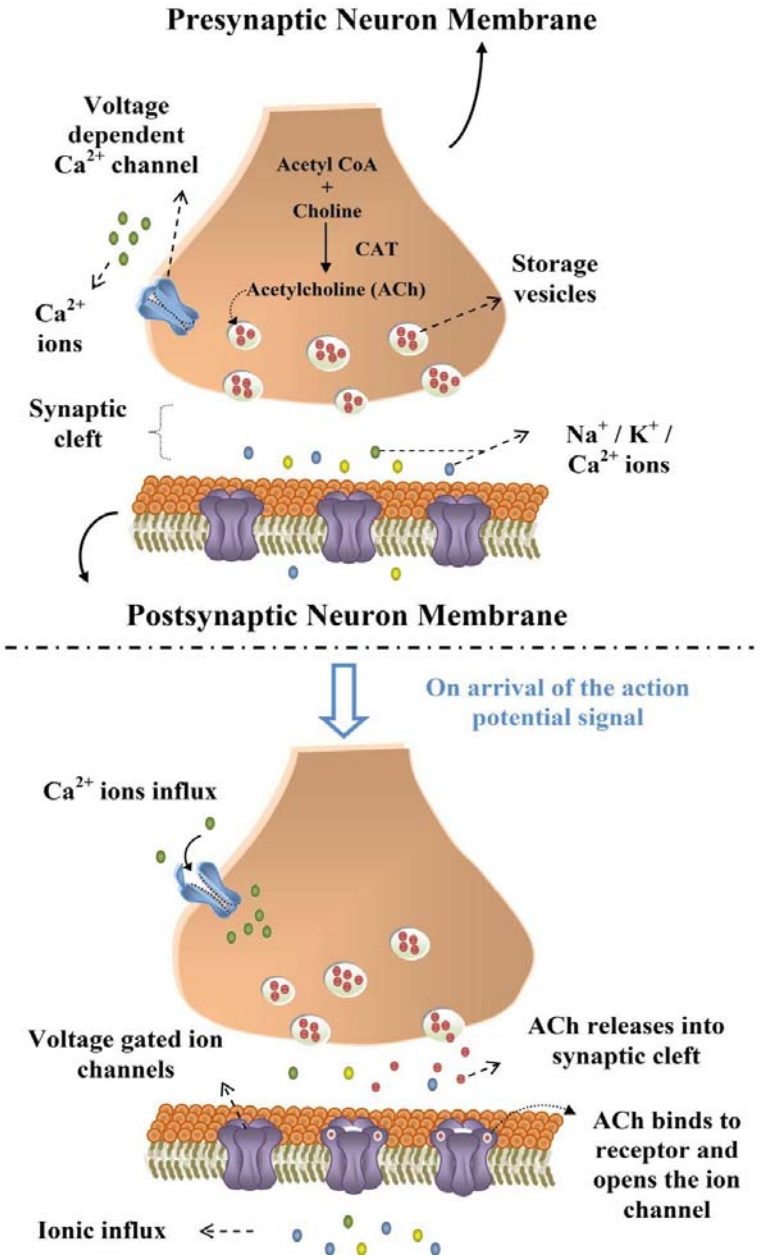

Fig. 4. 1. Biological representation of the neural synaptic transmission process taking place between the presynaptic and the postsynaptic neurons. The biological concept is taken from [28],[29],[85].

Usually a single *EPSP* is not sufficient to elevate the membrane potential above the threshold value. As a consequence, the postsynaptic neuron would not be able to generate the action potential and neuron-to-neuron communication would not be able to proceed further. To overcome this, a summation of the *EPSPs* occurs at the postsynaptic membrane which raises its potential above the threshold value and a postsynaptic action potential is generated [28],[88]. *EPSPs* are added together in two different ways [29],[88]: (i) successive action potential signals at a presynaptic neuron generate rapid and consecutive *EPSPs* at the same synapse. The addition of these *EPSPs*, which occur

within very short time intervals, is known as temporal summation, and (ii) when concurrent excitatory inputs occur at different regions of the presynaptic neuron membrane, individual *EPSPs* corresponding to each action potential signal are generated simultaneously. The accumulation process for these postsynaptic potentials producing a larger *EPSP* is known as spatial summation [29],[88].

For certain neurotransmitters such as GABA, *inhibitory postsynaptic potential* (*IPSP*) is produced instead of *EPSP*. *IPSPs* hyperpolarize the neuron membrane potential due to which they decrease the likelihood of postsynaptic action potential firing. Even the summation of *IPSPs* will further decrease the potential and the postsynaptic neuron will not take part in the neuron-to-neuron communication process [28]. Due to this reason, excitatory neurotransmitters are considered for the proposed model in order to represent neuron-to-neuron communication process.

4.3 Ca^{2+} IONS CONDUCTANCE ANALOGOUS TO MEMRISTOR

Morris and Lecar mathematically represented Ca^{2+} ions current across a neuron cell membrane [75]. Keeping in view the role played by Ca^{2+} ions in neuron–to–neuron communication, the variable Ca^{2+} ions conductance in the Morris and Lecar nerve membrane model has been proved to be equivalent to a voltage–controlled memristor in this chapter. The physiological characteristics acquired by this mathematical representation and by actual Ca^{2+} ions channels in neurons are understood to be similar [89].

4.3.1 Mathematical Representation of Ca^{2+} Ions Conductance across a Neuron Membrane

Ca^{2+} ionic current, I_{Ca} is expressed mathematically by the following equation in the Morris and Lecar model [75]:

$$I_{Ca} = \left[g_{Ca\max} * M(V,t)\right] * (V - V_{Ca}) \tag{4-1}$$

where g_{Camax} is a constant value, being maximum conductance Ca^{2+} ions, V is the membrane potential, $M(V, t)$ represents the fractional opening of the Ca^{2+} ion channel

for the membrane potential V, and at a certain time t, while V_{Ca} is the equilibrium potential corresponding to Ca^{2+} ions conductance. The term $g_{Camax}*M(V,t)$ in (4-1) represents calcium ion conductance, g_{Ca} ;

$$g_{Ca} = g_{Ca\max} * M(V,t) \tag{4-2}$$

Memristive behaviour of the Ca^{2+} ionic channel can only be visualized in its transient state, which was not closely explored by Morris and Lecar. The set of equations that are accountable for memory effects created by the Ca^{2+} channels were not taken into consideration before and thus are focused upon in this research. These equations are related to $M(V,t)$ as mentioned in Morris-Lecar research in [75] and were originally based on the nerve membrane equations developed by Hodgkin and Huxley in [27]. The equations are mentioned below [75]:

$$\frac{dM(V,t)}{dt} = \lambda_M(V)[M_\infty(V) - M(V,t)] \tag{4-3}$$

$$M_\infty(V) = \frac{1}{2}\left\{1 + \tanh\left[\frac{(V - V_1)}{V_2}\right]\right\} \tag{4-4}$$

$$\lambda_M(V) = \bar{\lambda}_M \cosh\left[\frac{(V - V_1)}{2V_2}\right] \tag{4-5}$$

where $M_\infty(V)$ represents a fraction of the channel opening at a steady state for membrane voltage V, V_1 is the potential at which the steady state opening is 50% [$M_\infty(V_1) = 0.5$] and V_2 is the reciprocal of the slope of $M_\infty(V)$ voltage dependence ($V_2 = 1/[dM_\infty(V)/dV]$). Rate constant and the maximum rate constant for the Ca^{2+} channel opening are denoted by $\lambda_M(V)$ and $\bar{\lambda}_M$, respectively [75].

4.3.2 Voltage Controlled Memristor

In [31], Chua represented a voltage controlled memristor by the following equations:

$$\frac{dx}{dt} = f(x,v,t) \tag{4-6}$$

and,

$$i = G(x,v,t)v \tag{4-7}$$

where x is the state of the system, v represents voltage applied as an input, G is a continuous scalar function, i denotes port current, and t is time. A memristor is time invariant if the functions f and G are not explicit functions of time [31]. A time-invariant voltage controlled memristor can be mathematically represented as follows [31]:

$$\frac{dx}{dt} = f(x, v) \tag{4-8}$$

and,

$$i = G(x, v)v \tag{4-9}$$

Equation (4-3) illustrates that the time differential of the variable M is a function of M and membrane (input) voltage V. On the other hand, (4-1) shows that the voltage current relationship of Ca^{2+} ions conductance in the nerve membrane depends on the state of the system, M. Equations (4-1) representing Ca^{2+} ions conductance and (4-3) representing the voltage-current relationship are satisfying Chua's criteria specified for a memristor in (4-9) and (4-8), respectively, which had not been considered or observed before. To conclude, the flow of Ca^{2+} ions at the synapse has the ability to be modelled as a voltage controlled memristor.

4.3.3 Memristive System Equations for Ca^{2+} Ions Channel

A non–homogeneous first–order linear differential equation with a constant forcing function is given by [90]:

$$\frac{dx(t)}{dt} + ax(t) = b \tag{4-10}$$

where x is the variable which is to be determined, t is time, a is constant with respect to t, and b is the constant forcing function. The general solution [90] of (4-10) is of the form given by:

$$x(t) = x_f(t) + x_n(t) \tag{4-11}$$

or,

$$x(t) = \frac{b}{a} + Ae^{-at} \tag{4-12}$$

where $\left[x_f(t)=\frac{b}{a}\right]$ is the forced or steady state response and $\left[x_n(t)=Ae^{-at}\right]$ is the natural response of the system [90]. The solution (4-12) of (4-10) is applied to (4-3) as it is also a non–homogeneous first-order linear differential equation. The steady state response becomes equal to:

$$Steady\ State\ response = M_\infty(V) \tag{4-13}$$

The natural or transient is equal to:

$$Transient\ Response = \left[M_0(V) - M_\infty(V)\right]e^{-\lambda_M(V)t} \tag{4-14}$$

As a result, the solution of the Morris – Lecar Ca^{2+} ion memristive system equation (4-3) is written as:

$$M(V,t) = M_\infty(V) + \left[M_0(V) - M_\infty(V)\right]e^{-\lambda_M(V)t} \tag{4-15}$$

where M_0 is the fractional channel opening state at t = 0 (at resting potential). A step–by–step solution of (4-3) is illustrated in Appendix A.

4.3.4 Implementation and Results

The mathematical model based on equations (4-1), (4-2), (4-4), (4-5) and (4-15) is implemented in a MATLAB environment. This model represents Ca^{2+} ions conductance as a voltage controlled memristor. To check the dependence of the conductance on the initial state, two different values are used for the channel's fractional opening at time = 0, M_0 = 0.007 and M_0 = 0.1 (although equations were simulated for several M_0 values, but results are only shown for two values because results were similar for all M_0 values and were meeting criteria. So, in order to avoid repetition results are only shown for two M_0 values). The equilibrium potential of Ca^{2+} ions, V_{Ca} is set to 123 mV [29] and membrane voltage, V is set as a sinusoidal wave with different amplitudes and frequencies. V_1 and V_2 in (4-4) and (4-5) are set to 10 mV

and 15 mV, respectively, as specified in [75]. The maximum conductance g_{Camax} is a constant scalar quantity and it is clear from (4-1) and (4-2) that it only amplifies (scales) the output signal; therefore, an arbitrary value of 1mS/cm^2 is assigned to g_{Camax}. $\overline{\lambda}_M$ is 0.1 as specified in [75].

When a sinusoidal voltage signal is applied as input to a memristor, the graph obtained between the excitation voltage and the periodic current response is a Lissajous figure. It consists of double current values corresponding to each voltage value and it passes through origin [91]. This is a unique property of a voltage controlled memristor. By applying 1V, 8Hz sinusoidal membrane voltage input to the mathematical model of a Ca^{2+} ions channel memristive system, a double valued Lissajous figure is obtained between the voltage and current across a memristor as shown in Fig. 4.2. Since, 2 – 20Hz is the normal frequency for neurons [92], 8Hz is chosen because it lies within the normal frequency range. Conductance of a memristor becomes time invariant and linear on application of a very high frequency (approaching to infinity with respect to the specific environment) periodic voltage signal [91]. This unique characteristic of a memristor is also satisfied by this mathematical model. When a periodic voltage signal with a 130Hz frequency (130Hz is a high frequency value for neurons [92],[93]) is applied, the voltage-current graph obtained is equivalent to a time-invariant linear resistor. On the other hand, when the input frequency is set low (2Hz and 8Hz), the system does not act linearly anymore. This frequency dependent behaviour of the voltage controlled memristor is depicted in Fig. 4.3.

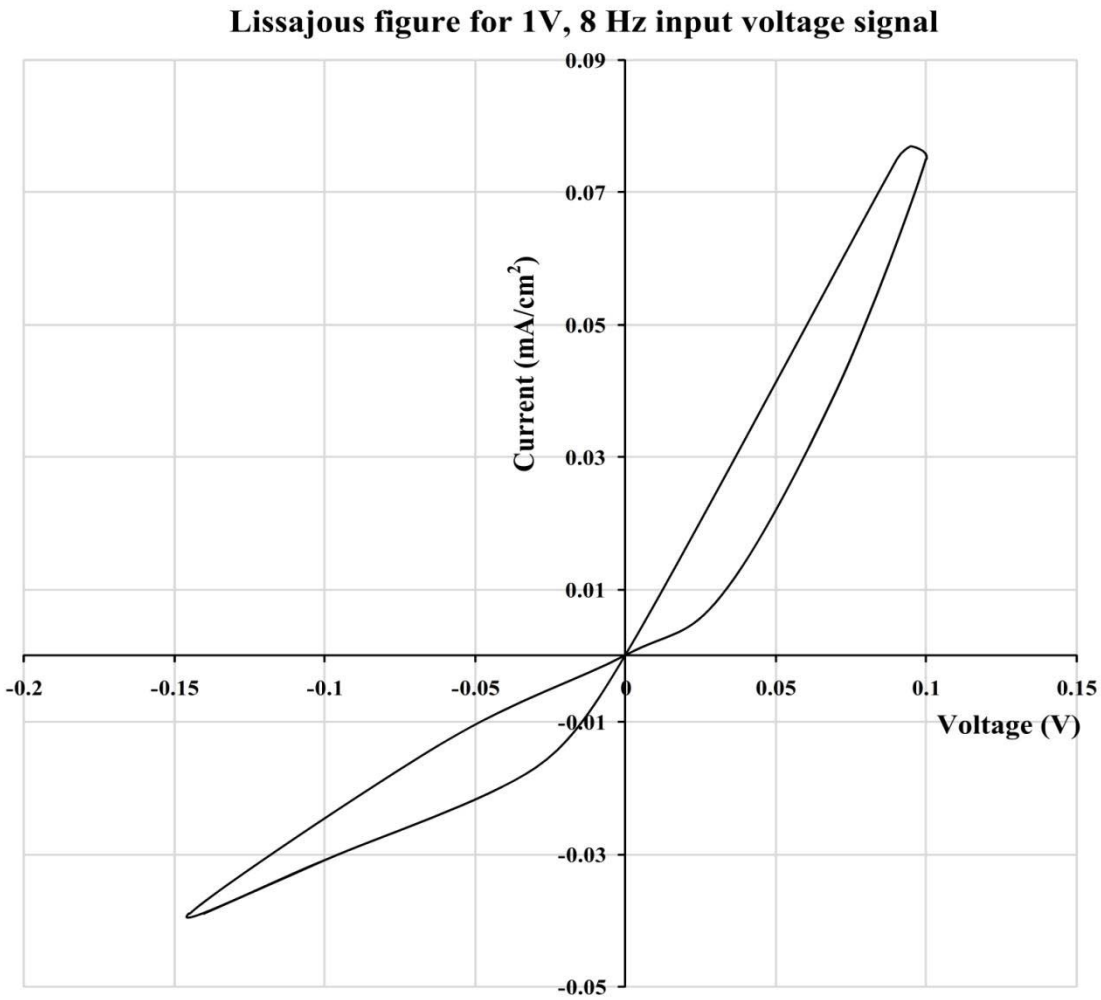

Fig. 4. 2. The Lissajous figure associated with the input membrane voltage (1V, 8 Hz) and the current response of the memristor.

The time invariant linear conductance value depends on the initial state of a system [91]. In this model, M_0 is the initial state of the Ca^{2+} ions channel. In Fig. 4.4, two time invariant conductance lines are shown for two different initial states M_0, whereas the periodic input voltage with a high frequency is the same (1V, 130Hz sinusoidal voltage signal). The solid line shows the conductance for $M_0 = 0.007$, while the dotted line indicates the value for $M_0 = 0.1$. In Fig. 4.5, conductance for these two values of M_0 i.e. 0.007 and 0.1 are plotted but the applied input is a 1.15 V, 130Hz sinusoidal signal. By comparing these two graphs it is clear that for a high frequency the conductance is dependent upon the initial state M_0 and not on the applied input (membrane) voltage, while for a low frequency the conductance is a nonlinear voltage dependent element.

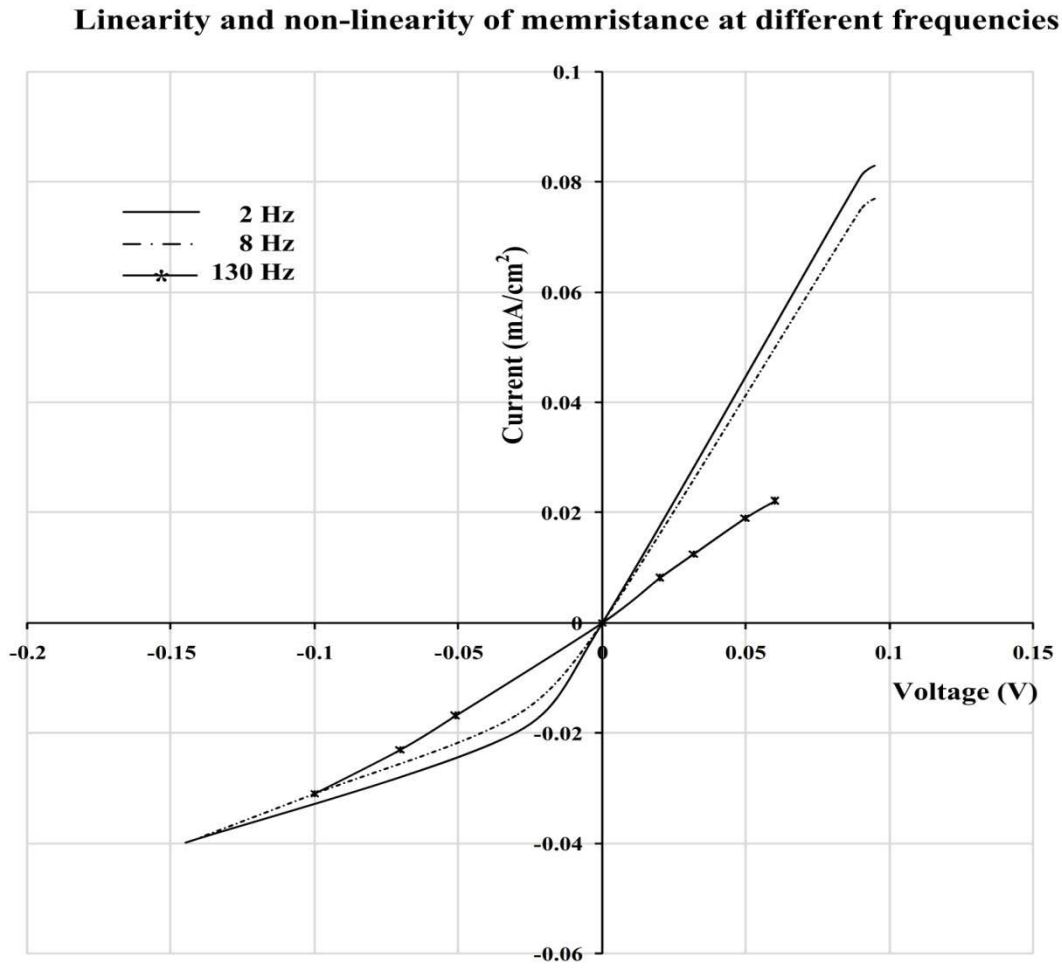

Fig. 4. 3. Voltage-Current relationship at different input frequencies. Memristance is a non linear curve at low frequencies (2Hz and 5Hz) and becomes linear at a very high frequency (130 Hz).

The Lissajous figure associated with input voltage and current response shrinks to a straight line with the frequency of the input signal approaching to infinity (with respect to the specified environment) [31]. This property is also satisfied by a memristive model of Ca^{2+} ions conductance across a neural membrane. 1V sinusoidal voltage signals with 2Hz, 8Hz and 130Hz frequencies are applied and MATLAB simulated results are plotted in Fig. 4.6. It is clear from the graph that the Lissajous figure becomes a straight line at a very high frequency, i.e. 130Hz (approaching to infinity with respect to the neural environment). These results show that the mathematical model of the Ca^{2+} ions conductance satisfies the properties of time invariant voltage controlled memristor as specified by Chua in [31] (pioneer of the memristor concept).

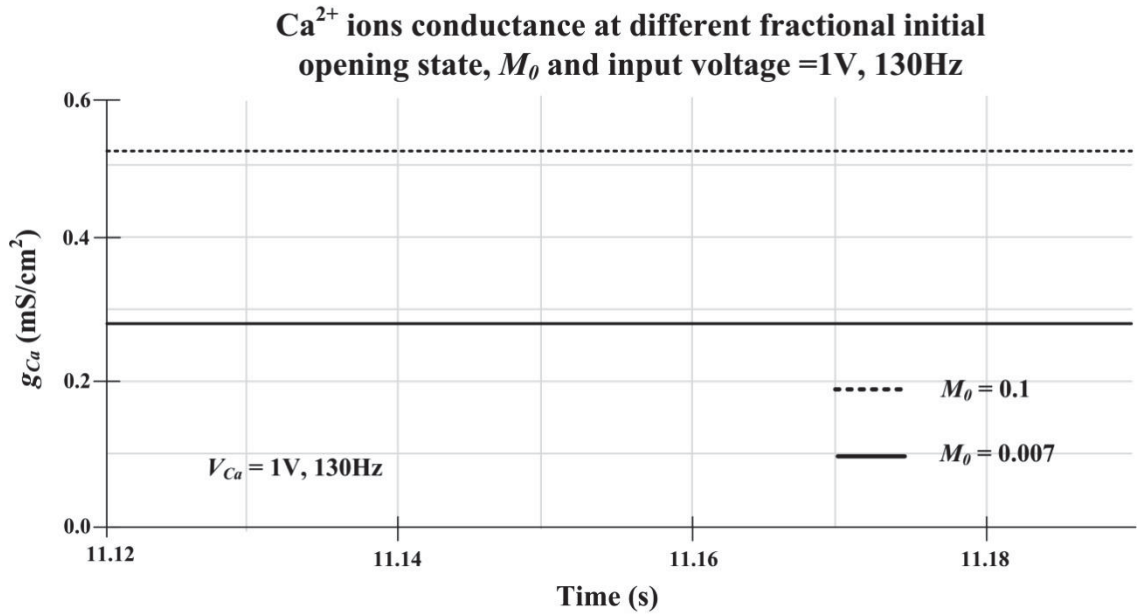

Fig. 4. 4. g_{Ca} value for 1 V and 130Hz input voltage signal. Two fractional initial channel opening states, M_0 values are taken i.e. 0.1 and 0.007.

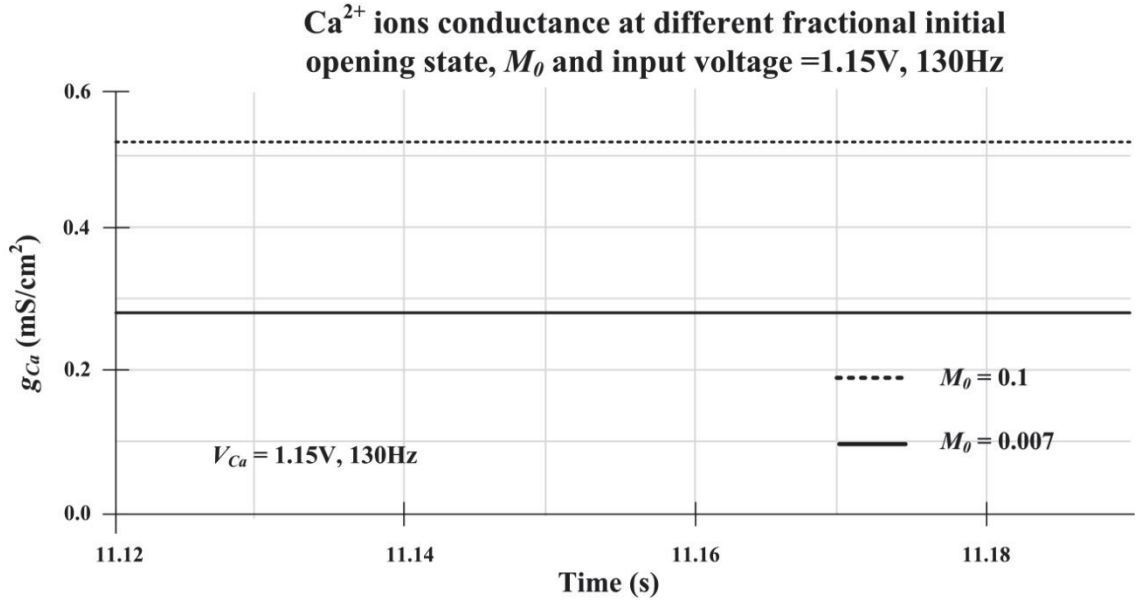

Fig. 4. 5. g_{Ca} value for 1.15 V and 130Hz input voltage signal. Two fractional initial channel opening states, M_0 values are taken i.e. 0.1 and 0.007.

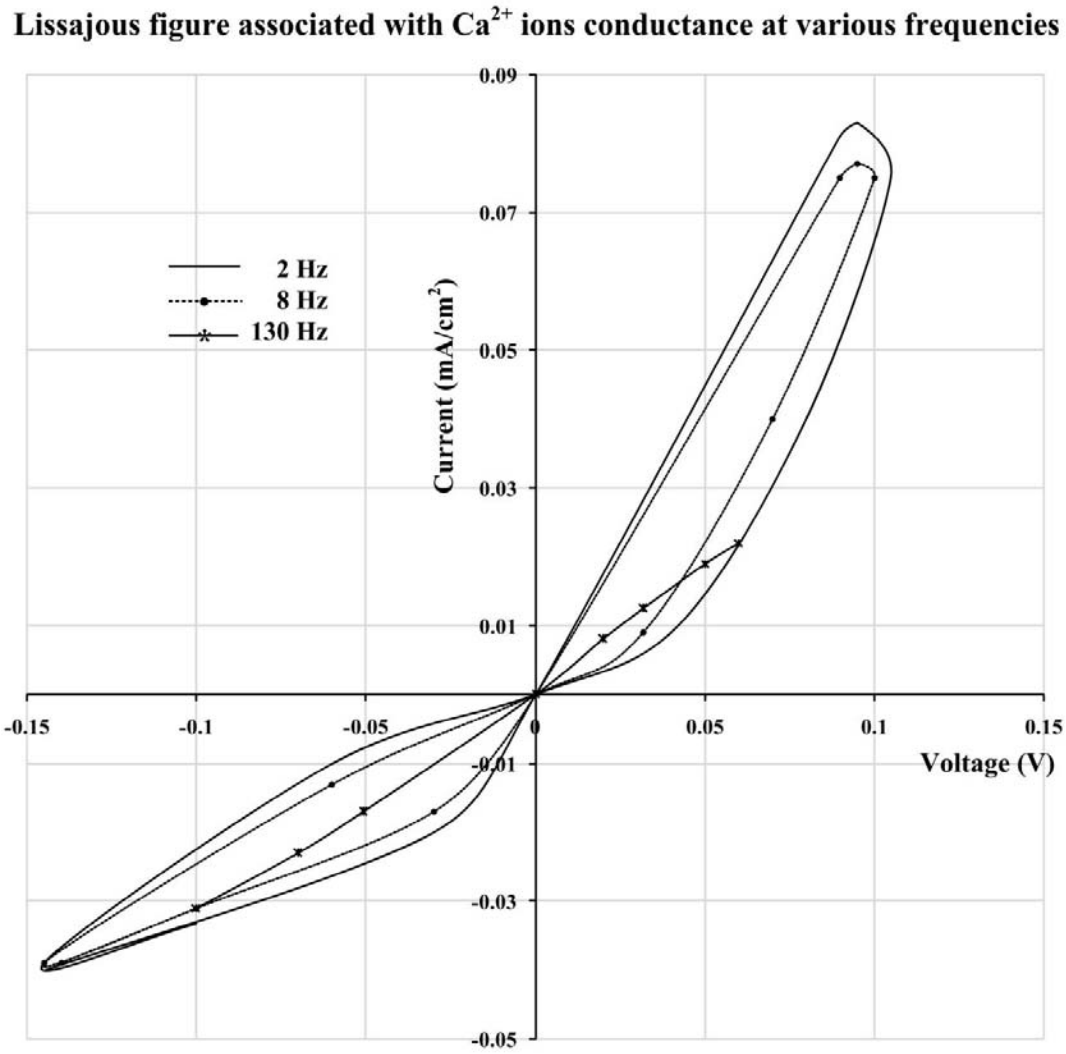

Fig. 4. 6. Lissajous figures related to the excitation voltage and the current response of the memristor equivalent to the Ca^{2+} ions conductance

4.4 ELECTRONIC CIRCUIT MODEL FOR THE NEURAL SYNAPTIC TRANSMISSION PROCESS

In order to mimic a biological process by an electronic circuit model, it is necessary to determine the link between the electronic circuit entities and the biological parameters. Decay is usually represented by a resistor (or conductance). Rate of reaction is similar to electrical current. Chemical concentration of molecular species is analogous to voltage at a circuit node [20],[22]. By utilizing the analogies between biological parameters and electronic entities, a VLSI neuromorphic model for the neural synaptic transmission is presented in Fig. 4.7.

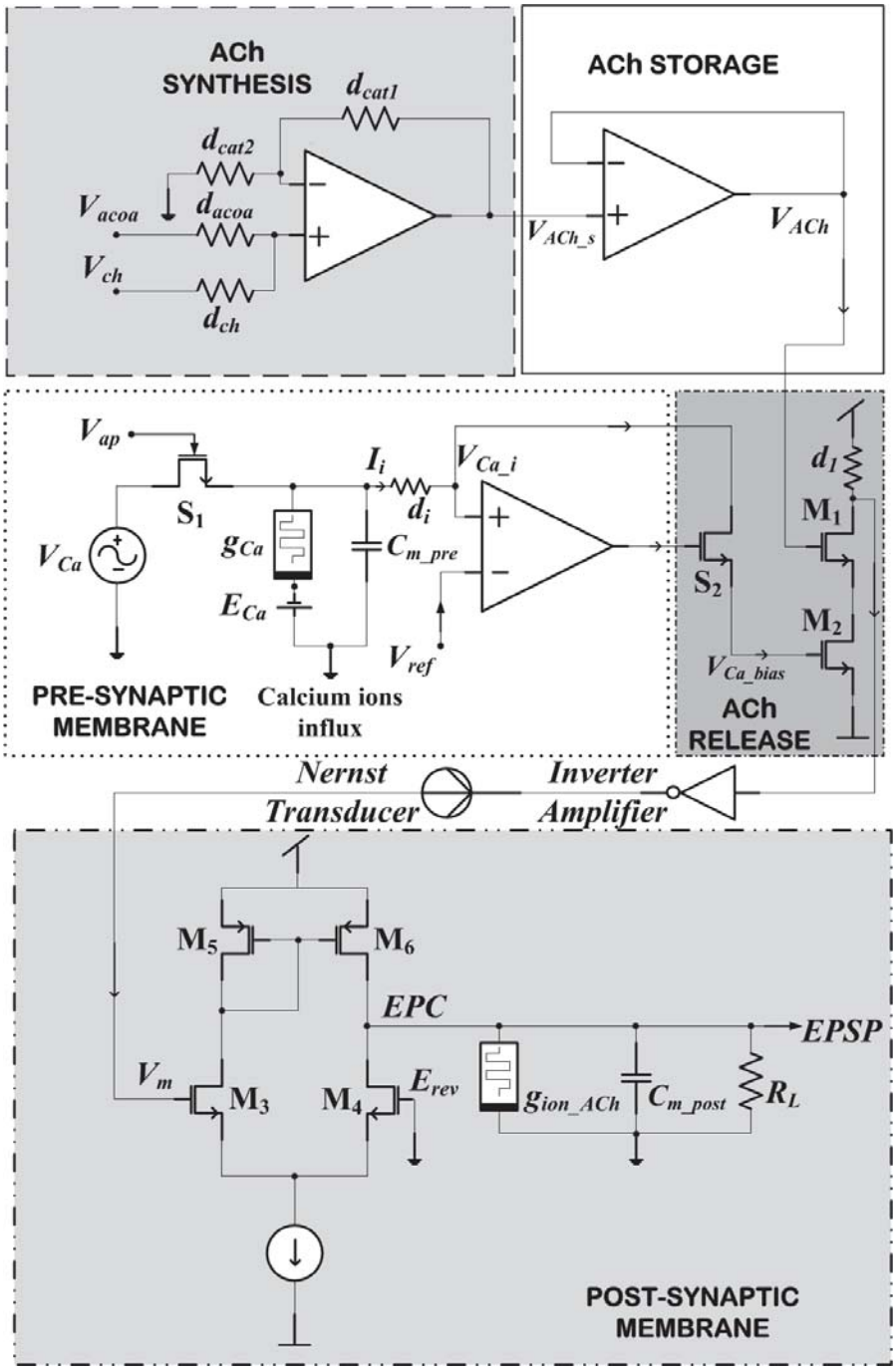

Fig. 4. 7. An electronic circuit model mimicking the neural synaptic transmission process. Stages involved in the transmission process are highlighted in square boxes. Inputs to the circuit are voltages V_{acoa}, V_{ch} and V_{Ca} analogous to acetyl coenzyme A, choline and extracellular Ca^{2+} ion concentrations respectively. Action potential input signal, V_{ap} acts as a triggering event for initiating the synaptic transmission process from presynaptic to postsynaptic neuron. Circuit output is temporally summed *EPSP* due to continuous pulses V_{ap} occurring at the same synapse of the presynaptic neuron membrane.

Every stage of the synaptic transmission process (shown in Fig. 4.7) is discussed separately along with mathematical equations representing the phenomenon involved in that stage.

4.4.1 ACh Synthesis

Phenomena involved in enzymatic reactions and functionality of non-inverting operational amplifiers are proven to be analogous in [18]. A mathematical model for the enzymatic reaction is given by:

$$\frac{1}{V_{in}} = \frac{1}{V_0} + \frac{R_f}{V_0} * \frac{1}{R_1} \tag{4-16}$$

where, V_{in} and V_o mimic substrate (*reactant*) and output product concentrations respectively. R_f and R_1 are decay constants which control enzymatic activity. The ACh synthesis process, which is an enzymatic reaction, is modelled by an Op-Amp. Acetyl CoA and choline are the reactants while CAT is the catalyst in this process. Voltages V_{acoa} and V_{ch} representing the concentration levels of acetyl-CoA and choline respectively, are provided as inputs at the non-inverting terminal of the Op-Amp. The amplifier operates as a non-inverting weighted summer [50]. As species decay is analogous to conductance, V_{acoa} and V_{ch} are applied through the decay rate constants d_{acoa} and d_{ch} respectively. The enzymatic activity of CAT is controlled by the conductances (decay rate constants) d_{cat1} and d_{cat2} which direct the rate of ACh synthesis. In molecular reactions, two or more reactant species are utilized (*decayed*) to form a product. By utilizing (4-16) and setting d_{acoa} and d_{ch} to 1m mho (to simplify the equation), ACh synthesis process can be mathematically modelled as:

$$\frac{1}{V_{acoa} + V_{ch}} = \frac{1}{2}\left[\frac{1}{V_{ACh\_s}} + \frac{1/d_{cat1}}{V_{ACh\_s}} * \frac{1}{1/d_{cat2}}\right] \tag{4-17}$$

where V_{ACh_s} mimics the ACh concentration after synthesis. d_{cat1} and d_{cat2} control the output concentration gain.

4.4.2 ACh Storage

ACh neurotransmitters are moved to storage vesicles after the synthesis process. They are transferred from the presynaptic neuron to the synaptic cleft without direct interconnection of the cleft and the neuron terminal. Electronically, voltage transfer from one point to another without any alterations or direct interconnection of these points can be carried out by a voltage buffer [94]. It connects a high input impedance circuit to a low impedance load. In this way, the load cannot vary the desired operation of the input circuit [50]. Hence, a unity gain voltage buffer or voltage follower is used to mimic ACh storage. The ACh stored (*buffered*) concentration, V_{ACh} is given by:

$$V_{ACh} = V_{ACh\_s} \tag{4-18}$$

where V_{Ach_s} is the ACh concentration after synthesis.

4.4.3 Chemical Synaptic Transmission Process

Extracellular Ca^{2+} ions concentration is represented by a sinusoidal input voltage source, V_{Ca} which is connected to the circuit model through an NMOS switch S_1. The action potential signal V_{ap} is provided as a control signal to the gate of S_1. As discussed earlier in this chapter, a voltage dependent memristor g_{Ca} is used to model the Ca^{2+} ion conductance through a neuron membrane. To model the membrane characteristics of a neuron, Hodgkin and Huxley [27] mentioned that a capacitor is needed in parallel with the resistance to allow ion current to pass through the membrane. Hence, a capacitor C_{m_pre} is connected in parallel with g_{Ca}. A constant voltage source E_{Ca} in series with g_{Ca} represents the internal potential of the neuron caused by the equilibrium concentration of Ca^{2+} ions [27],[29],[75]. The total membrane current is the sum of capacitive and ionic currents [27]. Due to the large extra-cellular ion reserve, the Ca^{+} ion source in Fig. 4.7 acts almost like an ion-current source which is equivalent to a V_{Ca} with high internal impedance; therefore, presynaptic membrane current I_i can be expressed as [75]:

$$I_i = C_{m\_pre}\frac{dV_{Ca}}{dt} + g_{Ca}\left(V_{Ca} - E_{Ca}\right) \tag{4-19}$$

ACh storage vesicles fuse at the neuron membrane when the intracellular Ca^{2+}

ions concentration reaches a certain range of value [95]. For this purpose, an Op-Amp comparator is utilized to compare the actual presynaptic internal Ca^{2+} ions concentration with the required threshold amount. Extracellular Ca^{2+} ions concentration of the neuron is very high compared to the internal concentration [28] (outside to inside concentration ratio 10,000:1 [29]). On the arrival of the action potential, ionic conductance through g_{Ca} causes the intracellular ion level, V_{Ca_i} to rise. The voltage V_{Ca_i} is compared with a reference voltage V_{ref} analogous to the required intracellular Ca^{2+}. Comparator output is as follows:

$$\text{Comparator Output} = \begin{cases} 0 \text{ for } V_{Ca\_i} < V_{ref} \\ 1 \text{ for } V_{Ca\_i} > V_{ref} \end{cases} \quad (4\text{-}20)$$

The output of the comparator controls an NMOS switch S_2 whose function is to regulate the transfer of the synthesized ACh concentration that proceeds towards the postsynaptic circuitry. The drain terminal of the NMOS transistor (switch S_2) is connected to V_{Ca_i}, while its source controls a transistor M_2. Transistor M_1 that is biased by M_2 regulates ACh release to the post synaptic neuron. An inverter is connected at the output terminal of M_1 in order to retain the polarity of V_{ACh} that was reversed by M_1. The Nernst transducer symbolizes the electro-chemical transduction caused by V_{ACh} flow towards the postsynaptic neuron.

4.4.4 Postsynaptic Neuron Circuit Model

ACh neurotransmitters' release changes the resting neuron membrane potential [28] symbolized by V_m. Binding of the neurotransmitters to postsynaptic receptors, i.e. output of transistor M_1, causes the ligand gated ion channels to open. As a result, *EPC* is generated. By applying Ohm's Law, the *EPC* magnitude is given by [28],[29]:

*EPC = (ionic conductance due to ACh) * (Electrochemical driving force for trans-membrane ion flow)* (4-21)

where,

Electrochemical driving force = Neuron Membrane Potential (V_m) – Reversal Potential (E_{rev}) (4-22)

Hence,

$$EPC = g_{m3,4}.(V_m - E_{rev}) = \left[\frac{EPSP}{R_L} + g_{ion\_ACh}.EPSP + C_{m\_post} \frac{d\ EPSP}{dt} \right] \quad (4\text{-}23)$$

The electrochemical driving force for trans-membrane ion flow/transfer, $V_m - E_{rev}$ can be modelled by using a MOS differential pair formed by matched transistors M_3 and M_4 with V_m and E_{rev} as its two differential inputs [50],[53]. The transconductance $g_{m3,4}$ of M_3 (M_4) can be used to represent the ionic conductance due to ACh (g_{ACh}) through ligand-gated ion channels because the ionic *EPC* is dependent on ACh flow external to the membrane. Any active load imposed on a differential pair can be a diode–connected load or a current–source load, or their combination. An active current mirror [32] formed by M_5 and M_6 [50] is used to transfer the *EPC* into the membrane. The active current mirror thus provides the single–ended *EPC* from the differential electrochemical driving force.

EPC generates postsynaptic membrane potential (*PSP*). The potential is termed as 'excitatory postsynaptic potential' (*EPSP*) if there is a chance that action potential will be generated in a postsynaptic neuron, otherwise it is known as 'inhibitory postsynaptic potential' (*IPSP*). Due to the change in postsynaptic membrane potential, voltage–gated ion channels are opened at the membrane and a flow of ions occurs. In the case of ACh neurotransmitters, the ions that flow across the membrane through these channels are usually Na^+ and K^+ [28]. Hence, the ion channel conductance g_{post_Na} and g_{post_K} caused by Na^+ and K^+ respectively, at the postsynaptic neuron membrane, are represented by voltage–controlled memristors [31]. A voltage source connected in series with each memristor represents the equilibrium potential for that particular ion, i.e. E_{Na} for Na^+ and E_K for K^+. A capacitor C_{m_post} connected in parallel with the memristor and equilibrium potential voltage source corresponds to the postsynaptic membrane capacitance.

4.4.5 Concurrent Synaptic Transmissions

For spatial *EPSP* summation, a single V_{ap} pulse should occur concurrently at different synapses of a neuron. In order to model the concurrent transmission phenomenon, a single V_{ap} pulse should occur at more than one circuit model presented in Fig. 4.7 at the same time and their final outputs (*EPSP*) should be added together. In

Fig. 4.8, two blocks "Syn_1" and "Syn_2", correspond to the same circuit model mimicking the neural synaptic transmission at synapse 1 and synapse 2 respectively. V_{ap_1} and V_{Ca_1} are the inputs to Syn_1 representing the action potential and the extracellular Ca^{2+} ions concentration respectively, while V_{ap_2} and V_{Ca_2} are the corresponding inputs for Syn_2. Outputs $EPSP_1$ and $EPSP_2$ of these two synapses are added together by a non-inverting weighted summer [50]. The inputs V_{acoa} and V_{ch} are the same for both blocks. The resistances R_1 and R_2 contribute to the *EPSP* summation gain factor, while R_3 and R_4 correspond to the weight constants for the synapses participating in the generation of spatially accumulated *EPSP*.

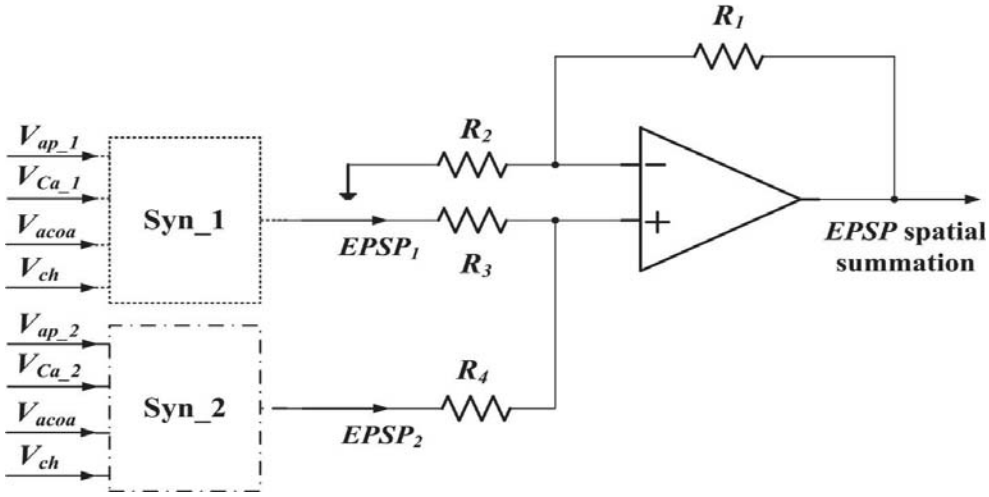

Fig. 4. 8. An electronic model of the concurrent synaptic transmission process generating spatially summed *EPSP*. "Syn_1" and "Syn_2" correspond to circuit model mimicking the neural synaptic transmission process (from Fig. 4.7) for synapse 1 and synapse 2 respectively. Extracellular Ca^{2+} ions concentrations for Syn_1 and Syn_2 are analogous to V_{Ca_1} and V_{Ca_2} respectively, while V_{ap_1} and V_{ap_2} are their action potential signals. Outputs $EPSP_1$ and $EPSP_2$ of these two synapses are added together by a non-inverting weighted summer.

4.5 SIMULATION RESULTS AND DISCUSSION

VLSI circuit models presented in Fig. 4.7 and Fig. 4.8 are simulated in *Mentor Graphics* software using 0.13µm IBM CMOS technology. The operational amplifier circuit design that is used for Fig. 4.7 and Fig. 4.8 is mentioned in Appendix B. Circuit parameters, conversion of chemical values into analogous electrical values, simulation results, circuit design validation and robustness of the circuit are discussed in subsequent subsections.

4.5.1 Circuit Parameters and Input Voltages

Quantitative biochemical parameters of the species involved in the synaptic transmission phenomenon are studied. In Fig. 4.7, these parameters are represented by their electrically analogous circuit entities as follows:

4.5.1.1 Chemical Concentrations and Equivalent Voltage Values

The standard unit of chemical concentration is Molarity (M) [51],[62]. Acetyl CoA concentration in [96] for a yeast metabolic cycle is reported to be approximately 30 μM while the concentration of choline is around 10 mM [28]. The extracellular Ca^{2+} ion concentration before the arrival of the action potential on the presynaptic membrane is approximately 1mM [28],[95]. There should be 0.1mM (or more) Ca^{2+} ions inside the neuron in order to fuse vesicles to the membrane for neurotransmitter release [95]. For a standard 0.13 μm CMOS technology, V_{DD} (positive supply voltage) and V_t (threshold voltage) have values of 1.2 V and 0.41 V respectively [97]. Hence, the required chemical concentration range (0.03mM – 10mM) for the proposed circuit model is scaled to voltages ranging from 0.41V to 1.2V by using [65],[66];

$$V(val) = \left[\frac{(1.2 - 0.41)}{(10 - 0.03)} (val - 0.03) + 0.41 \right] \text{V} \qquad (4\text{-}24)$$

where *val* is the chemical concentration in mM which is to be converted to its corresponding electronic analog in volts. Following (4-24), the nominal input voltage values for V_{acoa}, V_{ch}, V_{Ca} and V_{ref} are 0.41V, 1.2V, 0.49V and 0.416V respectively. V_{ap} (*an actual electric signal*) is set to a value of either 0V (*no action potential*) or 1.2V (*arrival of the action potential*) since it occurs as an all-or-none signal [28],[36]. E_{Ca} is set to 0.123V [29]. The binding of ACh to specific receptors opens ion channels that are permeable either to only one specific type of ion or to multiple types of ions. For the proposed circuit model, the case for which ACh activated channels are equally permeable to both Na^{+1} and K^{+1} [28] is considered. For this condition, E_{rev} is set to 0 V (standard reversal potential for Na^{+1} and K^{+1}).

4.5.1.2 Conductances and Capacitances

Cell membrane capacitance value per cm^2 is typically 1μF, thus C_{m_pre} and C_{m_post} are assigned nominal values of 1μF each [27],[85]. For simplicity, values of the decay constants (conductance equivalents) d_{acoa}, d_{ch}, d_{cat1} and d_{cat2} are set to 1m mho each so that V_{ACh} is equal to the sum of the concentrations V_{acoa} and V_{ch} with a gain factor of 1 (to correspond to a balanced chemical equation).

4.5.1.3 Memristor

Unlike other electronic circuit components, the memristor model is not supported by Mentor Graphics and other popular simulation software vendors owing to its novelty. Hence, a model discussed in [82] is modified for emulation on the 0.13 μm (for very large scale integration) CMOS process and is used in this work as shown in Fig. 4.9. V_{Ca} (representing periodic variation of Ca^+ ion concentration) is set to 100 Hz being a suitable value for the memristor model [82]. V_{ap} is either a single pulse for generating a single *EPSP* or is a continuous pulse wave for producing several *EPSP*s resulting in temporal summation. Ionic conductance through the synaptic membrane falls in an approximate range of 0.1 – 20 mS/cm^2 [28] which corresponds to a resistance of 50Ω.cm^2 to 10 KΩ.cm^2, R_{ON} and R_{OFF} of the memristance in Fig. 4.9 are thus set to 50 Ω and 10 KΩ respectively. Ionic conductance and capacitance values measured experimentally are per cm^2 area, while the electronic design is for μm^2. These values are not scaled for the μm^2 area because the concentration values that are taken from different resources result in these conductance and capacitance values per cm^2. Concentrations (in molarity units) are not changed, but the total concentration range is scaled to an electronic circuit voltage range. The current equation (4-19) taken from Morris-Lecar [75] mentioned that current, capacitance and conductance are measured per cm^2. Since, current is on the left side of equation (4-19) and capacitance and conductance are on right side of the equation, the area factor will be cancelled out. Hence, the area factor is ignored for all circuit parameters, i.e. current, voltage, resistance and capacitance.

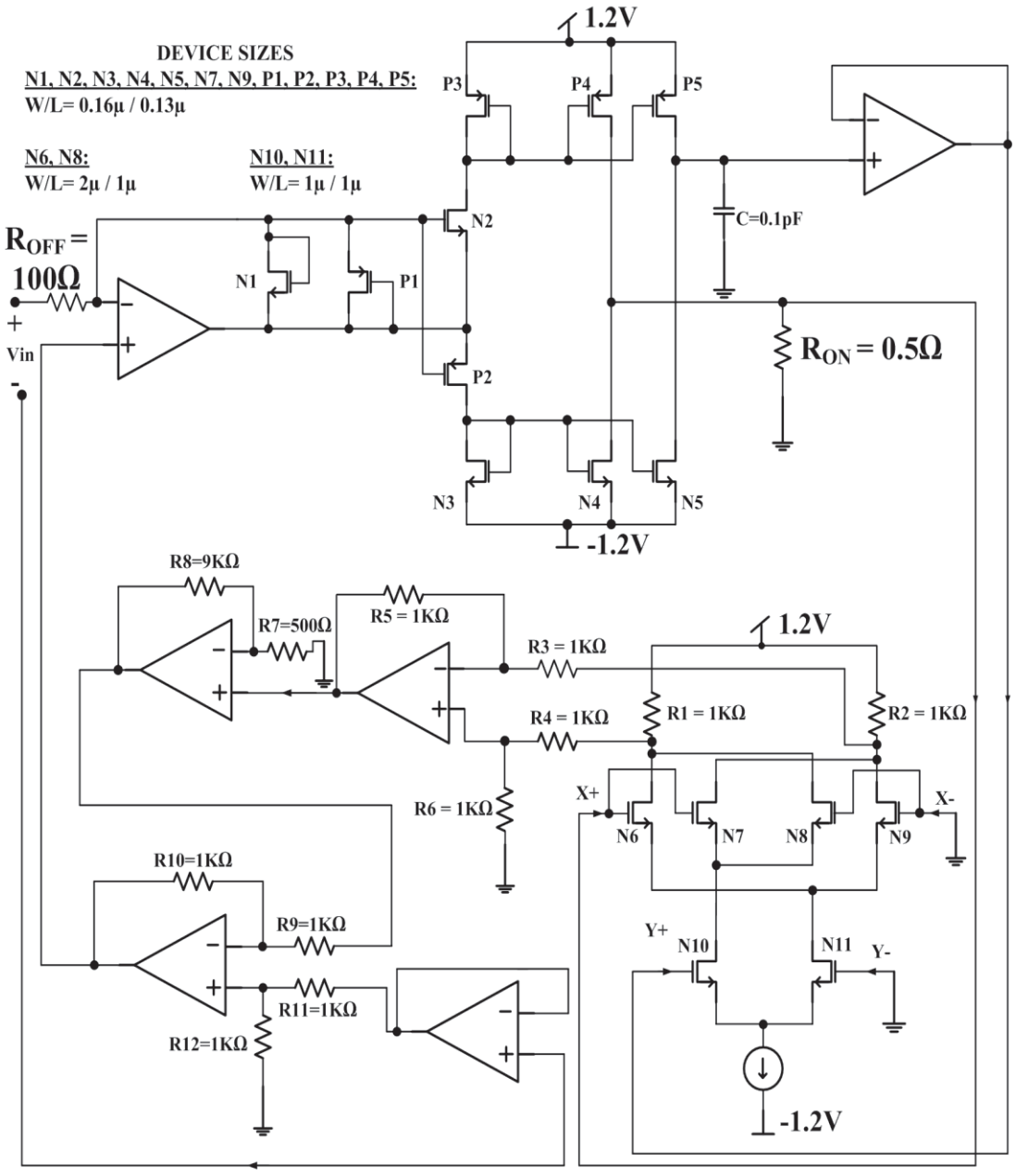

Fig. 4. 9. Memristor emulator developed by researchers in [82] is modified for 0.13 µm technology. It is used to model ionic conductance in the simulation of Figs 4.7 and 4.8.

4.5.2 Simulation Results

The memristor emulator redesigned for 0.13µm technology is simulated initially before proceeding towards the complete neuromorphic circuit simulation. The memristor emulator shown in Fig. 4.9 is connected in series with a 123mV voltage source (equivalent to equilibrium potential). The memristor and voltage source series combination is connected in parallel with a 1µF capacitor. A 1V, 100Hz voltage signal

is applied across this memristor, voltage source and capacitor combination. Fig. 4.10 illustrates that the emulator meets the unique Lissajous figure characteristics of the memristor. Hence, it is used further to model the ionic conductance during the neural synaptic transmission circuit.

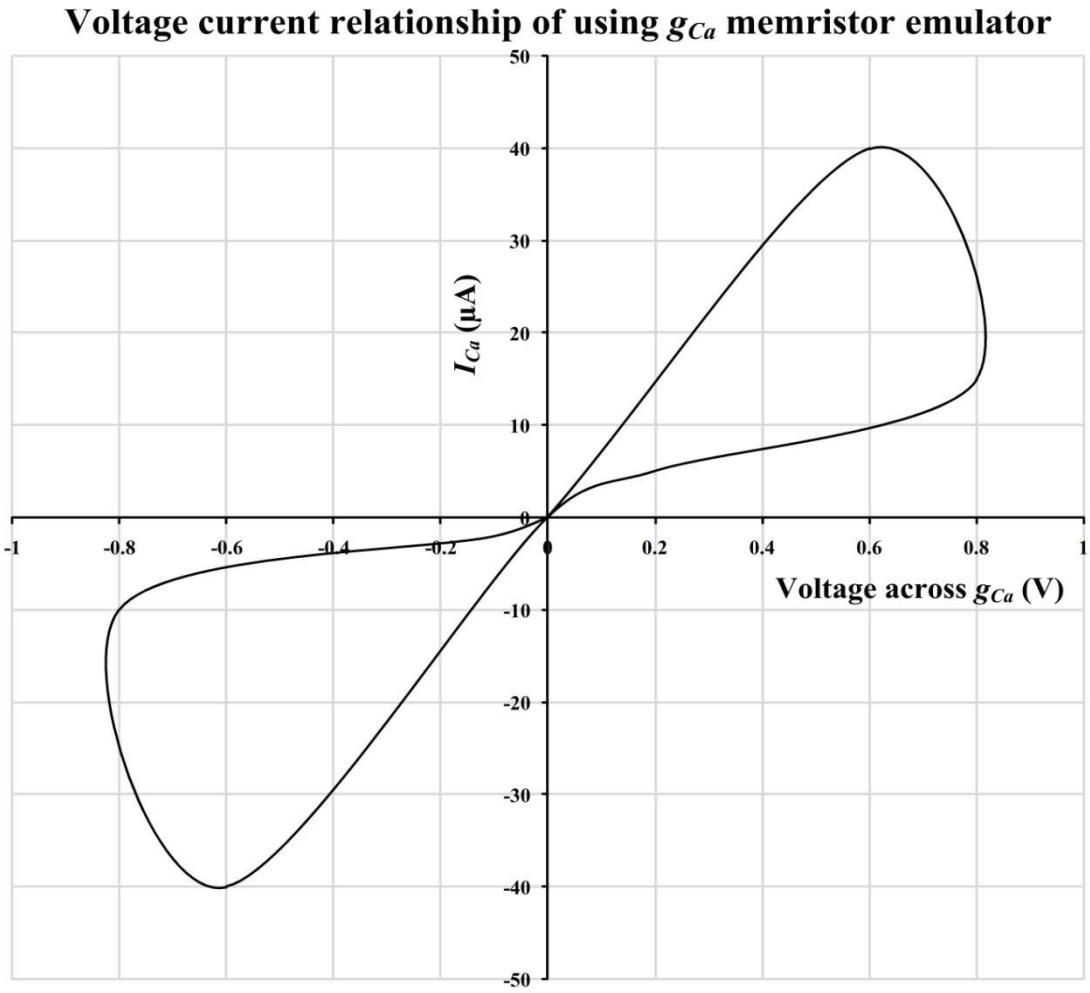

Fig. 4. 10. Lissajous figure obtained for Ca^{2+} ions conductance using the memristor emulator depicted in Fig. 4.9.

Fig. 4.7 is simulated in *Mentor Graphics* software using 0.13µm IBM CMOS technology. V_{Ach_s}, the output of the ACh synthesis circuitry, is held in the storage vesicles (*voltage buffer*). The storage buffer output V_{ACh} is ready to pass on to the postsynaptic circuitry as soon as switch S_2 is on. When the action potential reaches the presynaptic cell membrane (V_{ap} is high), S_1 is switched on and the conductance of Ca^{2+} (ion flow) occurs from the outside to the inside of the cell. The output of the comparator registers a "high" when V_{Ca_i} becomes greater than $V_{ref.}$ At this point switch S_2 turns on

and V_{Ca_i} is passed on. V_{ACh} is then transferred (in proportion to the intra-cellular Ca^{+} ion concentration, V_{Ca_i} in the positive feedback path) towards the postsynaptic membrane resulting in electro-chemical (*Nernst*) transduction (indicated by the transducer symbol in the model). As a consequence the postsynaptic membrane electro-chemical potential V_m is changed. Electrochemical driving force $(V_m - E_{rev})$ is thus produced on the Na^{+1} and/or K^{+1} ions which results in the generation of the *EPC*. The resultant postsynaptic membrane potential (*EPSP*) due to *EPC* flowing through the memristive channel opening and membrane capacitance is measured across the load resistor (membrane resistance) R_L. With V_{ap} pulsating continuously at the same synapse for time period of 2ms, the accumulation of *EPSP* is a temporal summation as shown in Fig. 4.11. An individual *EPSP* is obtained through a single stroke of V_{ap}.

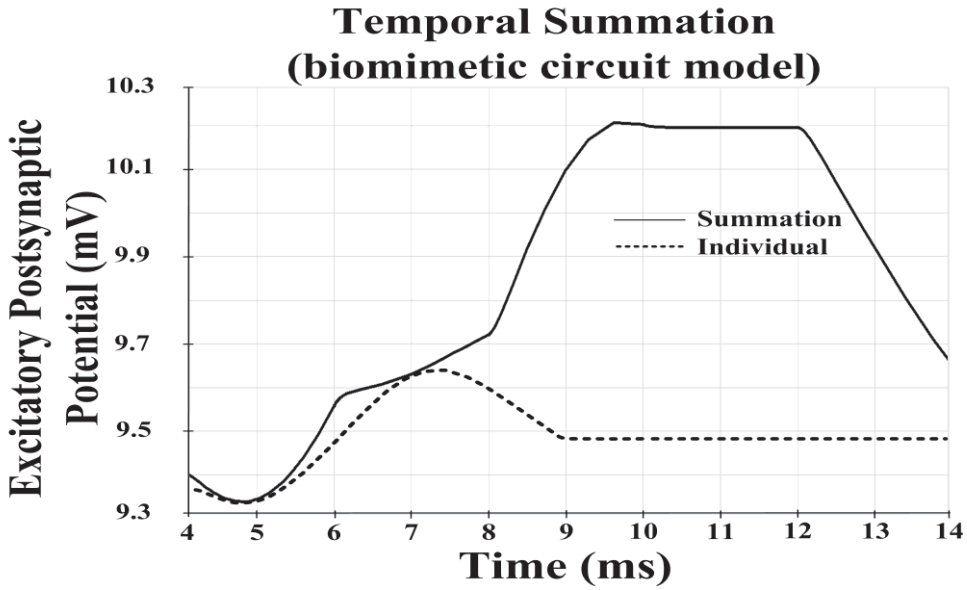

Fig. 4. 11. Temporal summation of *EPSPs* at the postsynaptic neuron. Solid line indicated the summed *EPSPs*, while the individual *EPSP* is represented by the dotted line.

Next, two single pulse action potentials V_{ap_1} and V_{ap_2} are applied to Syn_1 and Syn_2 of Fig. 4.8 and concurrent synaptic transmission is observed. Single pulse is generated by using a "pattern voltage source" and its pattern is set to 010000. When "1" occurs, a pulse is generated. Spatial summation occurs and the summed *EPSP* amplitude is increased. Spatially summed *EPSPs* are illustrated in Fig. 4.12. It is clear from these plots that the amplitudes of the individual *EPSP*s are lower than the

aggregate *EPSP*. Hence, spatial or temporal summation should occur for increasing the likelihood of action potential generation at the postsynaptic neuron [28].

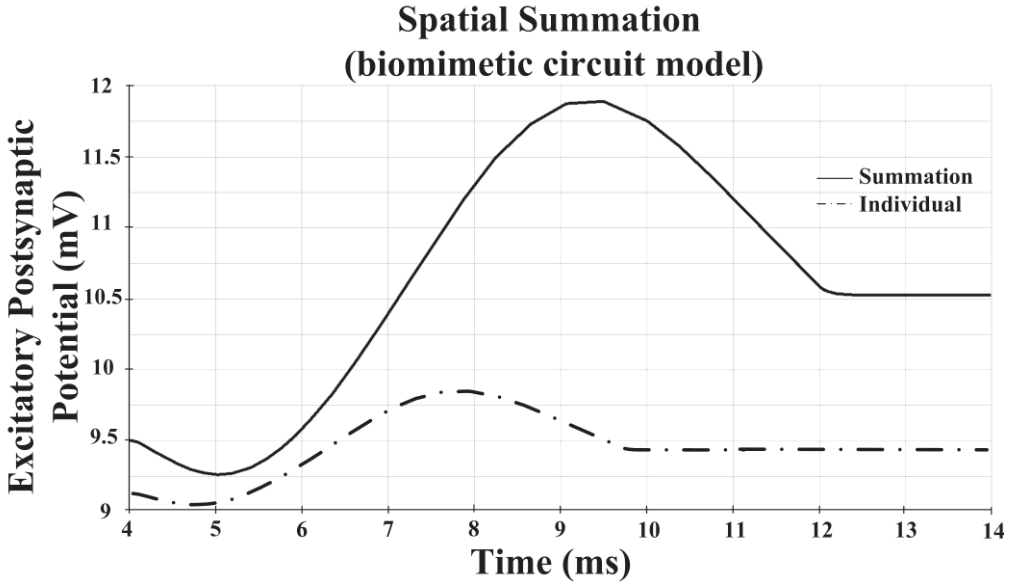

Fig. 4. 12. Spatial summation of *EPSPs* at the postsynaptic neuron. Solid line indicates the summed *EPSPs*, while the individual *EPSP* is represented by the dotted line.

The amplitude and polarity of *EPC* can vary with change in V_m [28]. The direction of the synaptic current is in the extra-cellular direction for $V_m <$ 0 mV and its amplitude is higher for higher negative values of the membrane potential. For positive values of V_m, *EPC* is in the intra-cellular direction and its amplitude rises with increase in the V_m magnitude [28] [85]. V_m is modulated by the released ACh neurotransmitters concentration, while the intra-cellular Ca^{+2} ion concentration controls the quantum of ACh to be release [28]. Hence, V_m can be varied by changing the amplitude of V_{Ca}. In addition, it can also be varied by changing ACh concentration through d_{cat1} fluctuations in the circuit model. Thus, the ACh concentration variation in the nominal range of 0.5 V to 1.0 V is *transduced* into simulated V_m in the range of -960 mV to +1.099 V. The resulting simulated synaptic current (*EPC*) is then determined for different values of V_m and plotted in Fig. 4.13. Synaptic current recorded through biological experimentation for membrane potentials between -95 mV to +38 mV are plotted in Fig. 4.14 taken from [85].

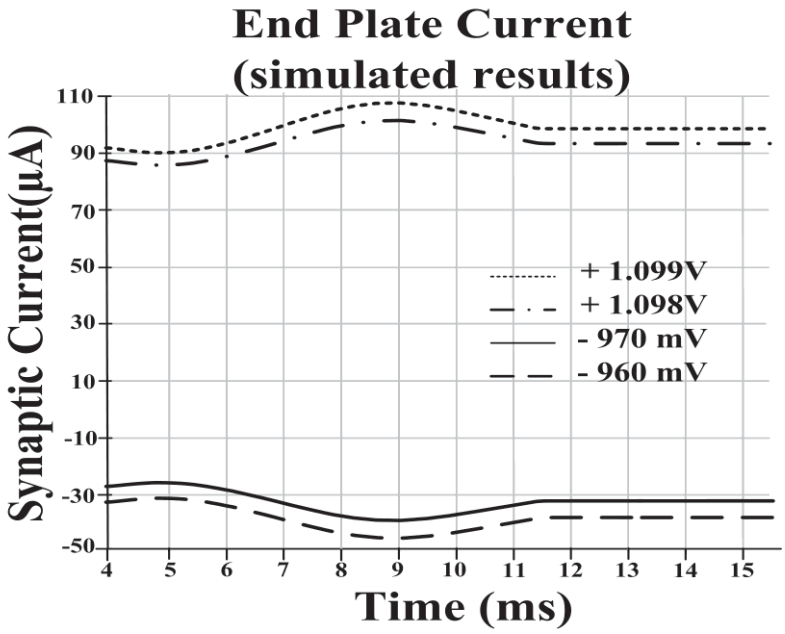

Fig. 4. 13. Circuit model simulation outputs for synaptic current at various V_m values.

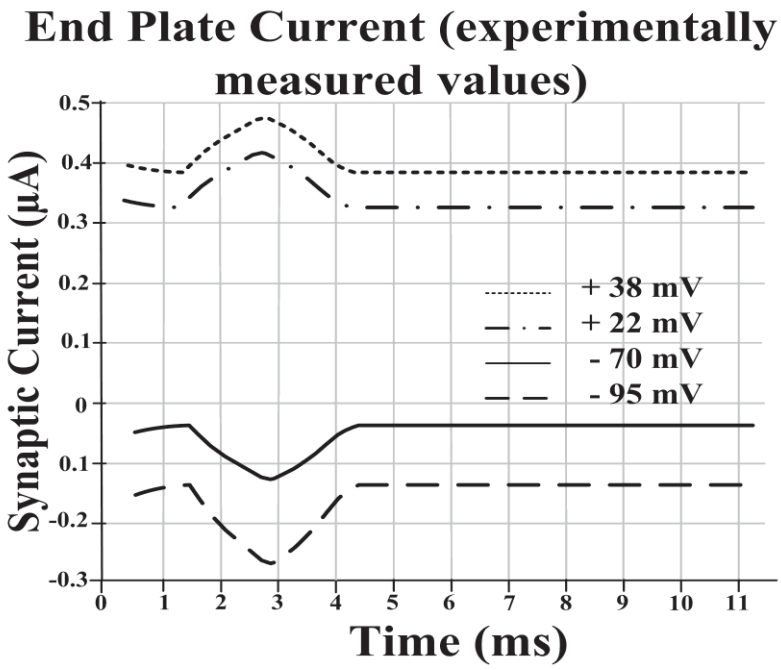

Fig. 4. 14. Data recorded from neuro-biological experimentation mentioned in [85] for the synaptic current at various V_m values.

4.5.3 Monte Carlo Analysis

In order to verify the robustness of the VLSI electronic circuit model mimicking the neural synaptic transmission process, Monte Carlo analysis is carried out in *Mentor Graphics*. A random parameter variation is carried out on all memristors, capacitors and resistors in Fig. 4.7 by selecting a built–in Gaussian distribution function from the software. Monte Carlo analysis of Fig. 4.8 is also performed by randomly varying Syn_1 and Syn_2 through the Gaussian distribution function. Since the purpose of the emulator is to verify behavior due to variations in bio-molecular concentrations, only those variables in the circuit model equivalent to the bio-chemical pathway parameters, that fluctuate the bio-molecular concentrations, and hence, effect the *EPSP*, are included in the Monte Carlo analysis. Conductances are known to be key factors that affect synaptic transmission output [98], [99]. On the other hand, supply voltage (VDD) in the circuit sets a fixed maximum for scaling the biological quantities being emulated, so that their variations can be modeled. Also, majority of neurons (>70%) are insensitive to temperature variations [100]. Hence, supply voltage and temperature are not considered for these Monte Carlo simulations. It is clear from the Monte Carlo analyses that the temporal and spatial summations of *EPSPs* are not affected by variations in the circuit parameters. Hence, the circuit robustness is verified by the Monte Carlo simulation results. Monte Carlo analysis for *EPSPs'* temporal summation and spatial summation are illustrated in Figs. 4.15 and 4.16 respectively. Study of the physiological behavior [101] indicates that the neural *EPSP* summation can vary by several mVs. Also, electrophysiological recordings indicate that stochastic fluctuations in *EPSP* due to random neurotransmitter release can be up to 67% of the normal value [102]. Hence the simulated stochastic variations in Figs. 4.15 and 4.16 are not significant. The pattern (envelope) of the *EPSP* summation appear similar despite variations in the value of the *EPSP*.

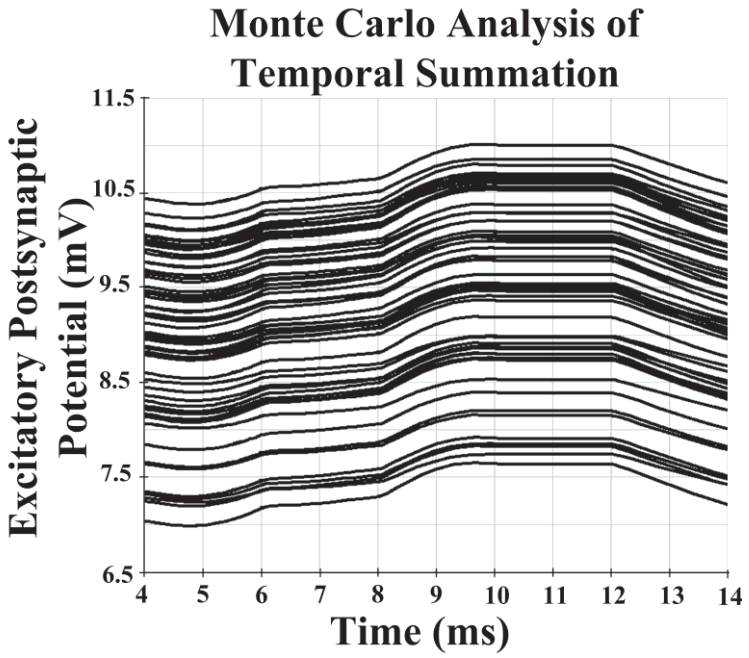

Fig. 4. 15. Monte Carlo analysis result for *EPSPs'* temporal summation. Memristors, capacitors and resistors in Fig. 4.7 are randomly varied by Gaussian probability distribution function.

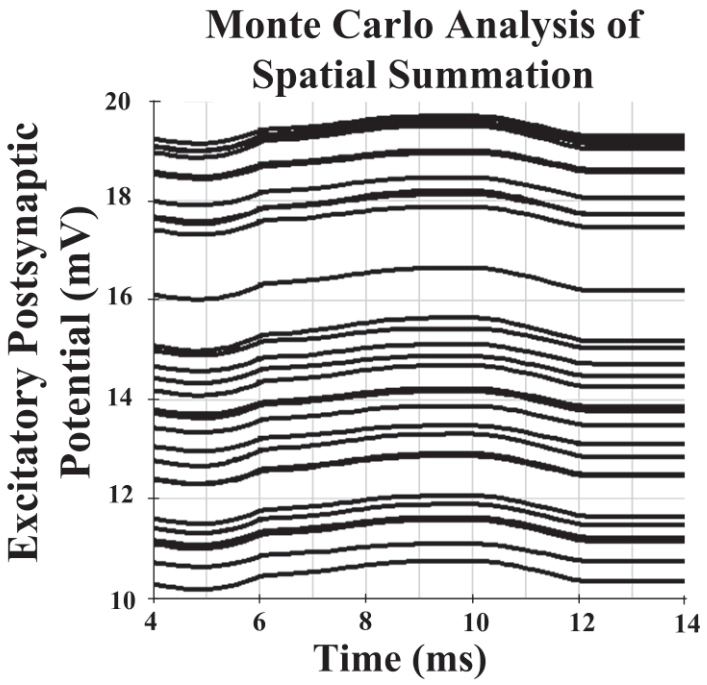

Fig. 4. 16. Monte Carlo analysis result for *EPSPs'* spatial summation. Syn_1 and Syn_2 in Fig. 4.8 are randomly varied by Gaussian probability distribution function.

4.6 CONCLUSION

A VLSI neuromorphic circuit model has been developed mimicking the biological neural synaptic transmission process. The chapter focuses on ACh neurotransmitter. However, the proposed circuit may only need to be slightly modified for other bio-chemical pathways/synapses with a different neurotransmitter. Any neurotransmitter that can initiate ion current and alter membrane potential can be considered. In addition, instead of variable resistors (e.g., in cellular level neural communication model in [103]), memristors have been utilized to accurately model the membrane Ca^{+2} ion channel conductance. Operational amplifiers with different configurations as well as simple CMOS amplifier stages have been found to bear a resemblance to several stages of the molecular level chemical synaptic transmission.

CHAPTER 5
BIOLOGICAL EXPERIMENTATION AND VLSI FABRICATION

5.1 INTRODUCTION

The cytomorphic circuit model of gene expression mechanisms presented in Chapter 3 is validated through biological experimentation. The circuit design is used to predict the cellular behaviour of a living organism with minimal effort and time, and the results are elaborated in this chapter. For this purpose, gene regulation in bacteria *Escherichia coli* is examined experimentally and the biological results are compared with the electronically analogous simulation results of the gene circuit model.

VLSI fabrication of the neuromorphic circuit mimicking the synaptic transmission process presented in Chapter 4 has been carried out. Fabrication details and the oscilloscope outputs of the fabricated chip are discussed in this chapter.

5.2 CYTOMORPHIC CIRCUIT VALIDATION THROUGH BIOLOGICAL EXPERIMENTATION ON BACTERIA

Examining a bacterium's response to alterations in its surroundings and changes in environmental conditions is one of the best ways to study the regulation of gene expression. *Escherichia coli (E.coli)* is a kind of bacteria and is highly adaptive to environmental changes because it regulates its gene expression accordingly. Protein synthesis from an *E.coli* gene and translation inhibition processes are observed experimentally. Afterwards, the results obtained from biological experiments are illustrated. Finally, to validate the electronic circuit model of the gene expression, the experimental outcomes are compared with the simulation results of the cytomorphic circuit model designed for gene expression regulation shown in Fig. 3.5, Chapter 3.

5.2.1 Regulation of Gene Expression of Individual Bacteria for Environmental Changes Adaption

E.coli cell residing inside the human colon depends on its host's diet. From human host intakes such as milk, cheese, cream [104], *E.coli* bacteria cells get lactose (β-galactoside sugars) [36]. During the catabolism process, lactose (β-galactoside sugar) is metabolically broken down into simpler molecules [105]. Glucose and galactose are produced from lactose hydrolysis [36]. This metabolic breakdown is a chemical process which is essential for maintaining the life of a living cell or organism [106]. Catabolism of complex sugars, such as lactose, needs enzymes to carry out this process. β-galactosidase enzyme is responsible for the catabolism of lactose. It means that with an increase in the amount of lactose, the β-galactosidase enzyme concentration should also increase in *E.coli* so that lactose can be broken down and the life of *E.coli* is maintained. In this way, lactose acts as an inducer molecule for the genes' coding for the β-galactosidase enzyme [36].

5.2.2 Spectrophotometric Analysis of β-galactosidase Activity

β-galactosidase activity in the bacterium *E.coli* is studied and analysed through spectrophotometry. The name of this technique is derived from the name of the instrument used - the *spectrophotometer*. There are several ways in which spectrophotometry is performed. In this experiment, the "absorption technique" is followed in which light rays are passed through a solution/sample for which spectrophotometric analysis is carried out. The amount of light absorbed by the sample depends on the sample concentration [107]. The absorbing sample's concentration can be calculated by applying *Beer-Lambert Law*. It defines a relationship between light absorbance and the absorbing sample's concentration. The Beer – Lambert law can be mathematically stated as [108],[109]:

$$A=\varepsilon*b*c \tag{5-1}$$

where A is the absorbance measured through a spectrophotometer, ε (M^{-1} cm^{-1}) is the molar absorption coefficient which is dependent on wavelength, the path length of light through the absorbing sample is denoted by b (cm), and c (M) is the sample

concentration. Path length is the width of the spectrophotometric cuvette. *A* has no unit because it is a logarithm ratio of light intensities given by [109]:

A = -log (Initial light intensity/Intensity of light radiated through the sample) (5-2)

The main objective of this experiment is to observe the β-galactosidase enzyme level (concentration) in *E.coli* after its gene transcription initiation under different conditions and in various time frames. Since, β-galactosidase enzyme activity is directly related to the β-galactosidase enzyme protein level [110]; absorbance spectrophotometry which measures β-galactosidase enzyme activity [111] is a standard way to determine the β-galactosidase enzyme level in *E.coli*. Different concentrations of various sugars and their combinations as mentioned in "Material/Reagents" section 5.3.1 are added into *E.coli* separately and the β-galactosidase enzyme activity is observed at different time intervals. Hydrolysis of *o*-nitrophenyl-β-galactoside (synthetic substrate) is used to carry out the spectrophotometric assay as mentioned in [105]. Chemically, *o*-nitrophenyl-β-galactoside (ONPG) hydrolysis process is:

_o_-nitrophenyl-β-galactoside + H_2O → _o_-nitrophenol + galactose (5-3)

The standard quantitative assay involves the measurement of *o*-nitrophenol spectrophotometrically [111]. The colour of *o*-nitrophenol is yellow and can be determined at 420nm wavelength by using spectrophotometer [105], [111]. The absorbance value measured from the spectrophotometer shows the amount of *o*-nitrophenol produced from ONPG hydrolysis which is directly related to β-galactosidase enzyme activity [111]. Higher β-galactosidase enzyme activity means more ONPG is hydrolyzed by β-galactosidase into *o*-nitrophenol. An increase in β-galactosidase enzyme activity corresponds to an increase in the β-galactosidase enzyme protein level [110].

β-galactosidase enzyme activity unit as determined by standard quantitative spectrophotometric assay is expressed as 1μmol of *o*-nitrophenol produced from ONPG hydrolysis per minute under specific assay conditions [111]. In this experiment, the spectrophotometric analysis is carried out on 1mL of *E.coli* cell culture [105], that makes it the specific assay condition for this experiment, i.e. ONPG hydrolysis per

minute per 1 mL of the cell culture [105]. Therefore, the activity unit is expressed as "1µmol of *o*-nitrophenol produced per mL of cell suspension per minute".

5.3 BIOLOGICAL EXPERIMENT FOR OBSERVING ESCHERICHIA COLI GENE BEHAVIOUR

A list of chemical reagents and instruments used for observing *E.coli* gene behaviour through spectrophotometric analysis, and a detailed biological procedure are mentioned in the following subsections.

5.3.1 Materials / Reagents

The following biological materials and chemical reagents are used in this experiment:

1. *E. coli* cells grown on a basal medium i.e. devoid of any extra sugar, but containing amino acids and mineral salts.

2. *o*-nitrophenyl-β-galactoside ($C_{12}H_{15}NO_8$)[106] (Sigma)
   Quantity: 0.02 M [105] (M stands for Molar – representing molarity which is a standard unit of concentration defined by the number of moles of solute per litre of solution [51]). The molar solution preparation method is illustrated in Appendix C)

3. Assay Buffer
   It consists of 0.1 M phosphate buffer with a pH value of 8.0 as described in [112]. The chemical composition of the buffer is depicted in Table 5.1. The pH of the solution is adjusted to the required value by using a pre-calibrated pH meter as described in [109]. Assay buffers are used because they are capable of maintaining pH values of the solutions at a constant level and prevents bio-molecules from destabilization [109]. Phosphate buffers are used because of their high buffering capacity [109]. High buffering capacity means that the phosphate

buffers have higher efficiency as compared to other buffers to maintain pH value at a constant level during the experiment [109].

Table 5. 1. Chemical components of phosphate buffer taken from [112]

S.No.	Chemical Name	Chemical Formula	Quantity	Company Name
1.	Potassium dihydrogen orthophosphate	KH_2PO_4	13.76g/L	Ajax FineChem
2.	Disodiumhydrogen phosphate anhydrous	Na_2HPO_4	14.2g/L	Scharlau

4. Chloramphenicol ($C_{11}H_{12}Cl_2N_2O_5$) [106](Sigma)
   The translation step is inhibited by chloramphenicol during the gene to protein synthesis process [105].
   Quantity: 1mg per 1mL [105].

5. Different sugar solutions:
   a. Lactose ($C_{12}H_{22}O_{11}$) [106]: 5% solution [105] (Ajax FineChem)
   b. Glucose ($C_6H_{12}O_6$) [106]: 5% solution [105] (Ajax FineChem)

6. Chemical Ingredients for *E.coli* culture medium:

In a cell culture or culture medium, cells taken from original tissues are established and maintained for further use [108]. The amount of β-galactosidase enzyme is very less when *E.coli* cells are grown without lactose. With the lactose supply in the bacteria's surrounding environment, the β-galactosidase concentration rises rapidly in the *E.coli* cells [36],[105]. Chemicals required for the basal culture medium listed in Table 5.2, are based on the chemical composition described in [113],[114]. The percentage weight by volume solution preparation method mentioned in Appendix C is applied where needed. Peptone is also included for the basal medium (not used in [113]) because it boosts *E.coli* growth [115]. Chemical formulae, the quantity of each chemical, and the company name from which the chemicals were bought are also mentioned in Table 5.2.

Table 5. 2. Chemical Reagents used for *E.coli* basal medium preparation

S.No.	Chemical Name	Chemical Formula	Quantity	Company Name
1.	Potassium dihydrogen orthophosphate	KH_2PO_4	0.4g/400mL	Ajax FineChem
2.	Dipotassium hydrogen phosphate	K_2HPO_4	0.4g/400mL	MERCK, Germany
3.	Trisodium citrate	$Na_3C_6H_5O_7.2H_2O$	0.2g/400mL	Ajax FineChem
4.	Ammonium Sulphate	$(NH_4)_2SO_4$	1.6g/400mL	VWR International Ltd.
5.	Peptone	Peptone from casein	2.0g/400mL	MERCK, Germany
6.	Sodium Chloride	NaCl	0.4g/400mL	Ajax FineChem
7.	Magnesium Sulphate heptahydrate	$MgSO_4.7H_2O$	7g/100ml	Ajax FineChem

5.3.2 Instruments/Apparatus

Instruments and apparatus (with appropriate volume) used in the biological experiment are listed below:

1. Novaspec III visible spectrophotometer, Amersham Biosciences, Sweden.
2. SI-300 incubated shaker, Jeiotech, Korea.
3. Isotemp hot water bath, Fisher Scientific Inc., USA.
4. ML204/0 weighing balance, Mettler Toledo, Switzerland.
5. RIOS 30M, Reverse Osmosis (RO) water purification system, Merck Millipore.
6. ARE heating magnetic stirrer, VELP Scientifica.
7. Bench top autoclave, Astell, UK.
8. NN-ST641W Panasonic inverter microwave.
9. Spectrophotometer cuvettes
10. Gilson pipetman automatic pipettor, Eppendorf Research, Physiocare Concept.

11. Pipette tips. Pipettor specific numbers, tip colour to be used with that pipette and volume range that can be measured by using those pipettors [105] are mentioned in Table 5.3.

Table 5. 3. Pipettor description [105]

Pipetman	Pipette tip colour	Measuring Volume
P200	Yellow	20 – 200 µL
P1000	Blue	100 – 1000 µL
P5000	White	1 – 5 mL

12. Schott bottles: 2-3 (400mL)
13. Timer
14. Conical Flasks (100mL,1Litre)
15. Measuring cylinder (100mL, 500mL)
16. Sterile test tubes
17. Inoculation loop and needle
18. Spatula
19. Cotton wool
20. Tin/aluminium foil

5.3.3 Biological Experimental Procedure

5.3.3.1 *E.coli* Culture Medium Preparation

Step one, first and foremost, when performing a biological experiment, is to follow the safety precautions. Standard safety procedures are followed as illustrated in [116]. The step–by–step process of culture medium (basal) preparation is described in Appendix C. One week prior to performing the practical, the Nutrient Agar/ Luria Broth plate is streak plated with *E.coli* colonies that were stored in glycerol stock. Appropriate *E.coli* storage is essential for maintaining bacterial cells and glycerol stock is the best means of storage [117]. Agar is a suitable medium for streak plating and developing bacterial colonies [116]. Agar plate and glycerol stock containing *E.coli* are obtained from Massey University Watson Science Laboratory, Albany. Streak plating is done

because bacterial isolated colonies can be created from it. These isolated colonies help to detect various biochemical characteristics of the micro-organism. Moreover, bacterial culture is also purified from unwanted contaminations by streak plating [116]. The streaking technique followed from [116] is discussed in Appendix C.

The bacterial–isolated colony is transferred into the culture medium through inoculation. The inoculation procedure described in [118] is mentioned in Appendix C. The basal medium is heated in a microwave oven. 20mL of the medium is transferred into a sterilized test tube and inoculated with the *E.coli* colonies developed on the streaked plate. It is incubated at 37^{o}C for 6-8 hours and placed in a cold room afterwards for later use. Five hours prior to performing the experiment, 6mL of the incubated basal medium is transferred into a 1 litre flask containing 300mL of water. It is incubated for 5 hours at 37^{o}C. Three aliquots of 22.5mL *E.coli* grown on the basal medium are transferred into three 100mL flasks separately.

5.3.3.2 Spectrophotometric Assay

Initially, a mixture of *o*-nitrophenyl-β-galactoside (18mL) and assay buffer (12mL) is stirred and then equilibrated at 40^{o}C in an Isotemp water bath. The temperature selected is 40^{o}C because at this temperature β-galactosidase enzyme activity is optimal. Once the temperature of the *o*-nitrophenyl-β-galactoside and assay buffer mixture reaches 40^{o}C, 2.5mL of this mixture and 1.0mL of specific cell suspension are directly added into the spectrophotometer cuvette [105].

The first reading is taken at 420nm from the spectrophotometer. Further readings are recorded at the same wavelength for five minutes with a one minute time interval. The cuvette is returned to 40^{o}C water bath each time so that the assay mixture temperature is maintained for the next reading. After recording five readings, the assay mixture in the cuvette is discarded, the cuvette is washed with tap water and is dried for the next use [105].

5.3.3.3 Inducing β-galactosidase Enzyme Activity by Sugar Addition in *E.coli* grown on Basal Medium

Three conical flasks are taken to observe the effect of lactose, glucose, and lactose + chloramphenicol separately on β-galactosidase activity. Each flask is filled

with 22.5 mL of ***E.coli*** bacterial culture medium grown on the basal medium. The flasks are placed in the incubated shaker whose temperature is set to 37^{o}C. The cells present in the cell culture are kept aerated by continuous shaking of the flasks containing the culture at 140rpm (revolutions per minute) by means of the incubated shaker. The flasks are covered with cotton wool and tin foil during shaking to avoid contamination.

A P5000 pipetman is used to add 2.5mL of lactose (5% solution) to one of the three conical flasks. Immediately after the addition of lactose to the cell culture, an assay mixture is prepared in a clean spectrophotometer cuvette. For the assay mixture, 1mL of cell culture with added lactose is transferred in the cuvette with the help of a P1000 pipetman. Then, 2.5mL of the mixture, prepared in section 5.3.3.2, containing o-nitrophenyl-β-galactoside and assay buffer, is added in the cuvette containing the *E.coli* culture. β-galactosidase activity is assayed through absorbance spectrophotometry by following the assay procedure mentioned above (section 5.3.3.2). After every fifteen minute interval, the assay procedure is repeated for the *E.coli* culture with a 5% lactose solution, and the absorbance is noted down.

As with the 5% lactose solution, the assay procedure is repeated for glucose and lactose + chloramphenicol in separate conical flasks. When measuring the effect of chloramphenicol on β-galactosidase activity, the 5% lactose solution is initially added in the flask at time zero and the first three assays are performed. Then, at 45 minutes, 200 µl of chloramphenicol is added, by using a P200 pipetman into the third flask containing 5% lactose solution, and the remaining four assays are performed at 45, 60, 75 and 90 minutes [105]. Chloramphenicol is a translation inhibitor [114]; therefore, β-galactosidase activity is reduced as observed from the absorbance plots in the next section.

5.3.4 Results

Five absorbance values of *o*-nitrophenol are noted down at fifteen minute intervals for each solution (lactose, glucose, lactose+chloramphenicol) during spectrophotometric analysis. Figs. 5.1 – 5.7 depict absorbance versus time plots of each assay for 0 – 90 minutes with 15 minute time intervals. Although chloramphenicol was added at 45 minutes, but Fig 5.1 to Fig 5.3 show plot for lactose+chloramphenicol for times earlier than 45 minutes. This is because β-galactosidase enzyme activity is plotted

by taking the slope of the absorbance graph lines and in order to understand the effect of chloramphenicol on β-galactosidase it is necessary to measure enzyme level before chloramphenicol addition. Equations mentioned on the graphs represent line of best fit or the linear trend of the absorbance value (selected from Microsoft Excel). A(L), A(G) and A(L + C) represent the absorbance linear trend for lactose, glucose, and lactose + chloramphenicol respectively. Time is denoted by 't'.

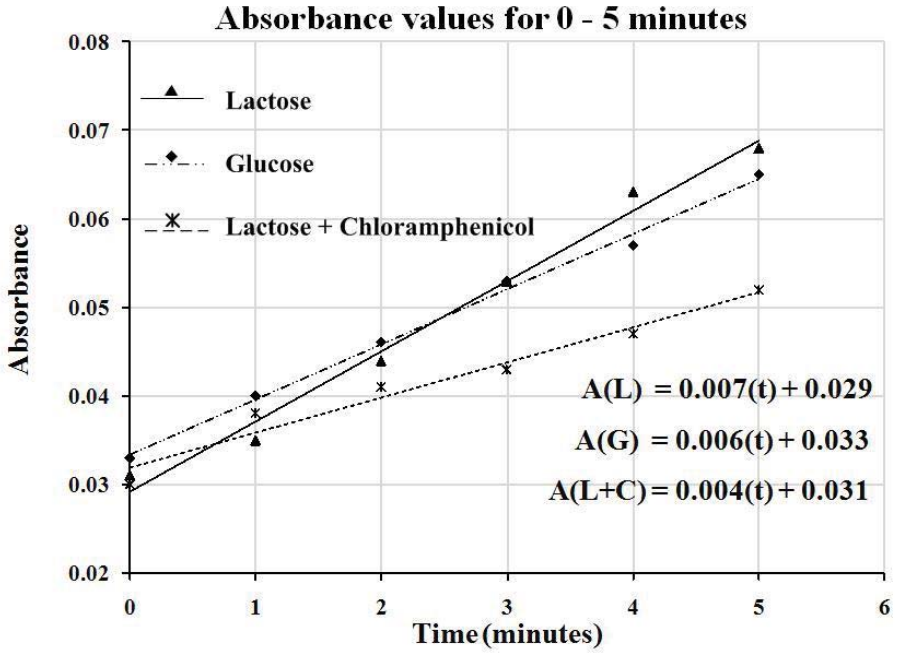

Fig. 5. 1. Absorbance versus time for 0 – 5 minutes.

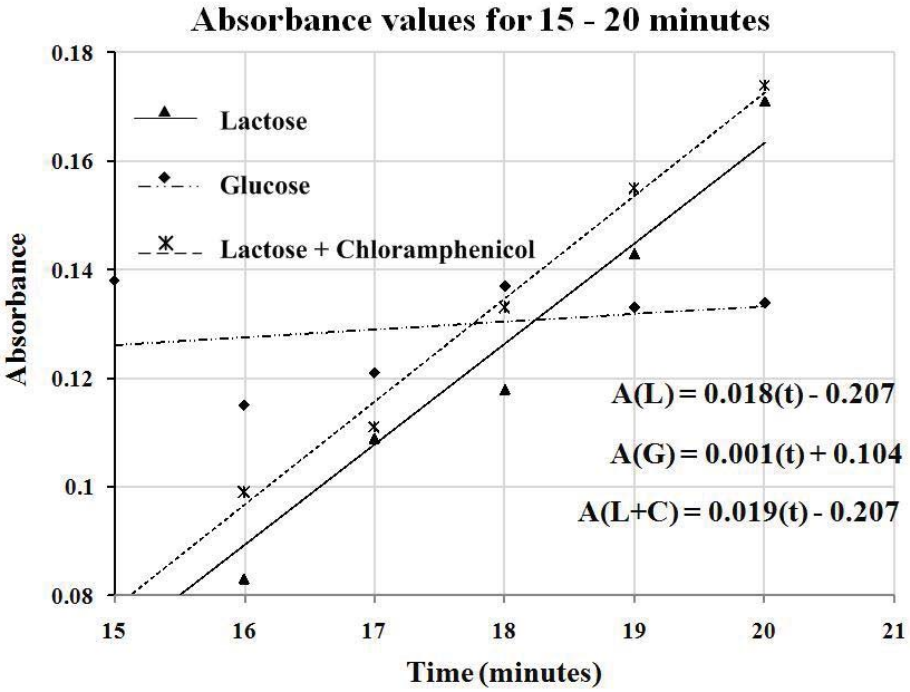

Fig. 5. 2. Absorbance versus time for 15 – 20 minutes.

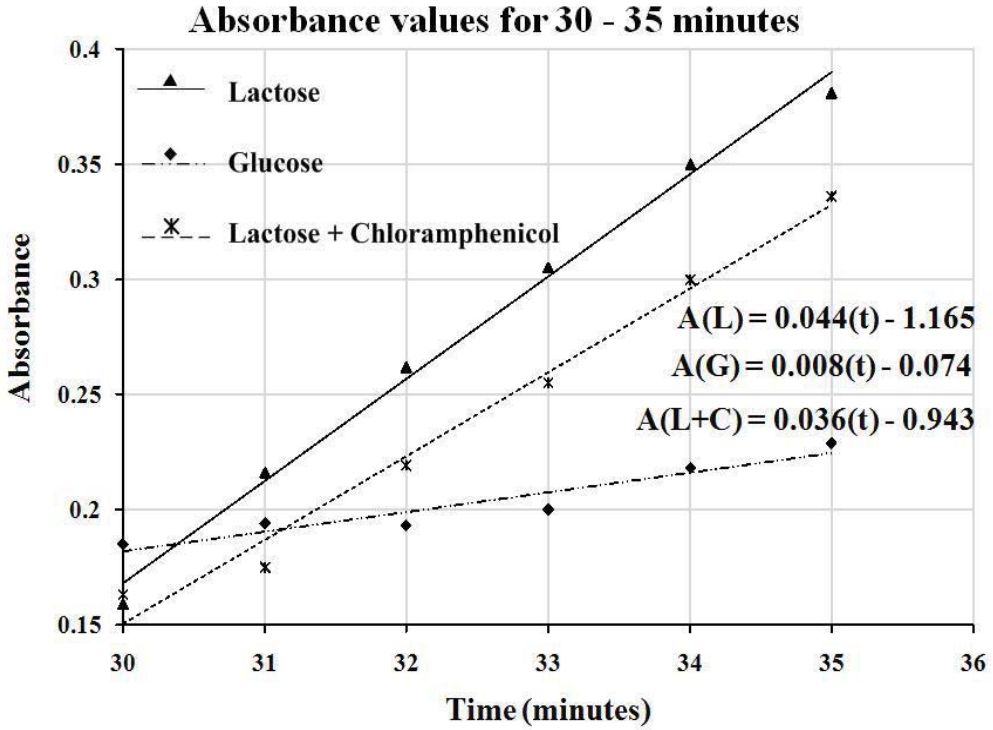

Fig. 5. 3. Absorbance versus time for 30 – 35 minutes.

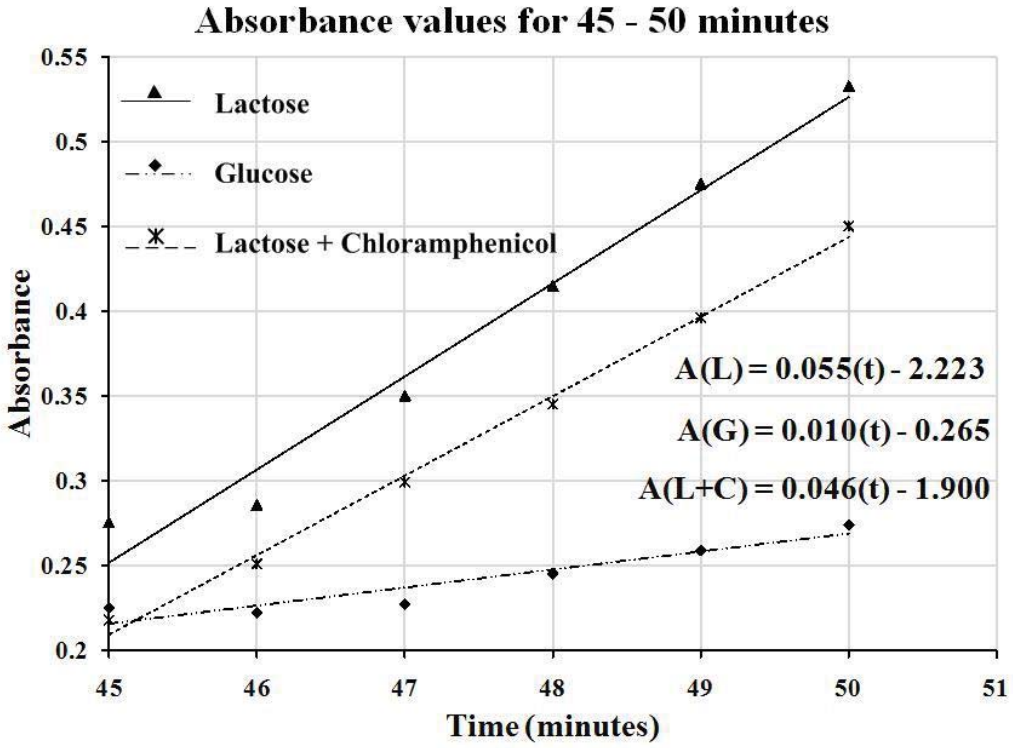

Fig. 5. 4. Absorbance versus time for 45 – 50 minutes.

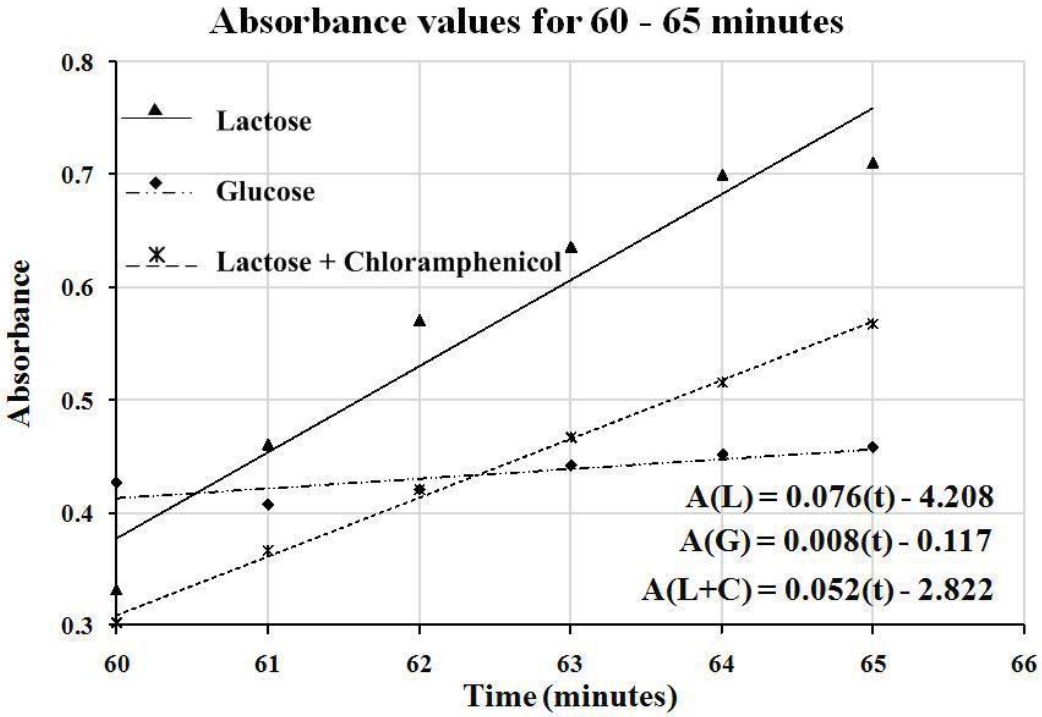

Fig. 5. 5. Absorbance versus time for 60 – 65 minutes.

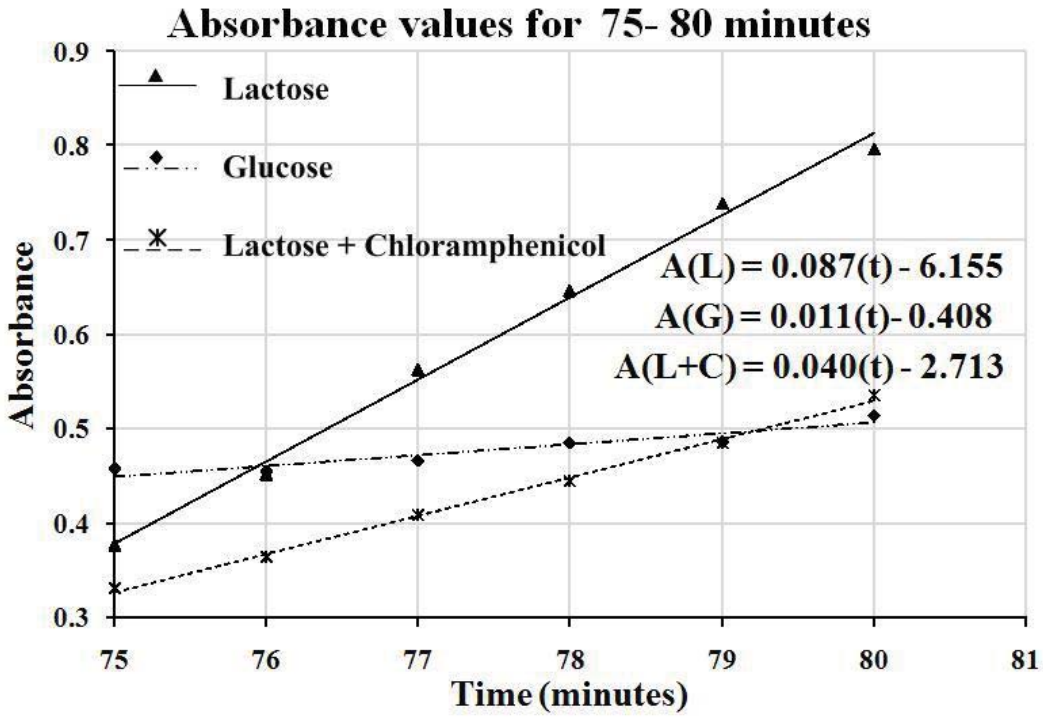

Fig. 5. 6. Absorbance versus time for 75 – 80 minutes.

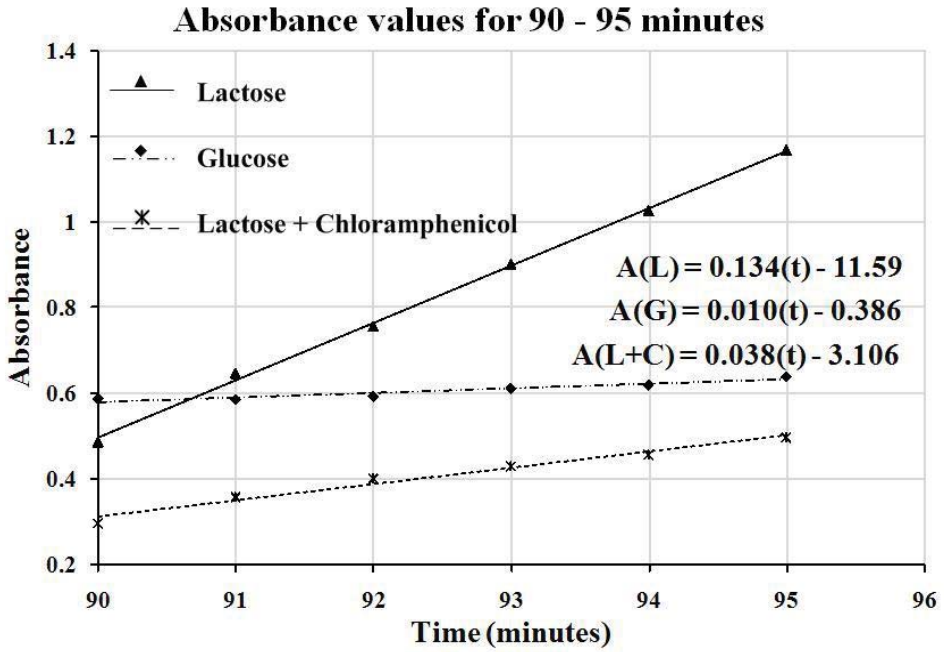

Fig. 5. 7. Absorbance versus time for 90 – 95 minutes.

The y-intercept values of the line equations mentioned in Fig 5.1 to Fig. 5.7 is automatically determined by Microsoft Excel by extrapolating the lines backwards until time=0 because y-intercept is calculated when x-axis has zero value. From the equations mentioned in Fig. 5.1 to Fig. 5.7, the change in absorbance per minute $\Delta A_{per\_\min}$ is determined. The slope of the linear line equation is $\Delta A_{per\_\min}$. For instance, $\Delta A_{per\_\min}$ for 0-5 min assay of lactose is:

$$\Delta A_{per\_\min} = 0.007 \tag{5-4}$$

By substituting $\Delta A_{per\_\min}$ in (5-1) a change in the *o*-nitrophenol concentration per minute $\Delta c_{per\_\min}$ [(mol/L)/min] is calculated.

$$\Delta c_{per\_\min} = \frac{\Delta A_{per\_\min}}{\varepsilon * b} \quad [(\text{mol/L})/\text{min}] \tag{5-5}$$

where ε = 18000Lmol^{-1}cm^{-1} [105] under specific assay conditions and b=1cm (width of cuvette used). In order to the convert concentration from mol/L to µmol/mL, $\Delta c_{per\_\min}$ is multiplied by 1000000(mol to µmol) and divided by 1000 (L to mL).

$$\Delta c_{(\mu/mL)/\min} = \Delta c_{per\_\min} * 10^6 / 10^3 \quad [(\mu\text{mol/mL})/\text{min}] \tag{5-6}$$

The spectrophotometer cuvette contains 3.5 mL solution (ONPG + phosphate buffer + cell suspension); therefore, $\Delta c_{(\mu/mL)/\min}$ is multiplied by 3.5 to determine µmoles of *o*-nitrophenol produced in a cuvette per minute.

$$o\text{- }nitrophenol_{\mu mol/min} = \Delta c_{(\mu/mL)/\min} * 3.5 \quad (\mu\text{mol/min}) \tag{5-7}$$

Finally, β-galactosidase enzyme activity $\beta - gal_{activity}$ i.e. µmoles of *o*-nitrophenol produced per mL of cell suspension per minute is calculated by dividing *o*-$nitrophenol_{\mu mol/min}$ by 1

$$\beta - gal_{activity} = (o\text{-}nitrophenol_{\mu mol/min})/1 \quad (\mu\text{mol/mL of cell suspension/min}) \tag{5-8}$$

Tables 5.4 – 5.6 show $\Delta A_{per\_\min}$ and $\beta - gal_{activity}$ values in each time interval for lactose, glucose, and lactose + chloramphenicol respectively.

Table 5. 4. ΔA_{per_min} and $\beta - gal_{activity}$ measured from 0 – 90 minutes for lactose

S.No.	Time Interval (mins)	$\Delta A_{per\_\min}$	$\beta - gal_{activity}$ (µmol/mL of cell suspension/min)
1.	0	0.007	$1.36*10^{-3}$
2.	15	0.018	$3.5*10^{-3}$
3.	30	0.044	$8.54*10^{-3}$
4.	45	0.055	0.0107
5.	60	0.076	0.0148
6.	75	0.087	0.0169
7.	90	0.134	0.02604

Table 5. 5. ΔA_{per_min} and $\beta - gal_{activity}$ measured from 0 – 90 minutes for glucose

S.No.	Time Interval (mins)	$\Delta A_{per\_\min}$	$\beta - gal_{activity}$ (µmol/mL of cell suspension/min)
1.	0	0.006	$1.17*10^{-3}$
2.	15	0.001	$1.95*10^{-4}$
3.	30	0.008	$1.55*10^{-3}$
4.	45	0.01	$1.95*10^{-3}$
5.	60	0.008	$1.55*10^{-3}$
6.	75	0.011	$2.14*10^{-3}$
7.	90	0.010	$1.95*10^{-3}$

Table 5. 6. ΔA_{per_min} and $\beta - gal_{activity}$ measured from 0 – 90 minutes for lactose + chloramphenicol

S.No.	Time Interval (mins)	$\Delta A_{per\_\min}$	$\beta - gal_{activity}$ (µmol/mL of cell suspension/min)
1.	0	0.004	$7.77*10^{-4}$
2.	15	0.019	$3.69*10^{-3}$
3.	30	0.036	$7*10^{-3}$
4.	45	0.046	$8.96*10^{-3}$
5.	60	0.052	0.0101
6.	75	0.04	$7.77*10^{-3}$
7.	90	0.038	$7.39*10^{-3}$

Fig. 5.8 illustrates the rate of $\beta - gal_{activity}$ for lactose, glucose and lactose + chloramphenicol. It is clear from the plots that in the case of glucose, enzyme activity is approximately zero. $\beta - gal_{activity}$ is increasing for lactose while, on the addition of chloramphenicol, it starts to decline and then becomes constant. The increase in enzymatic activity is due to the continuous induction of β-galactosidase by lactose [36]. Chloramphenicol is a translation inhibitor [105],[114]; therefore, its addition stops the β-galactosidase mRNA transcript to translate into a β-galactosidase enzyme. As a result

β-galactosidase enzymatic activity starts to decline. A certain point is reached when all mRNA transcripts are completely inhibited by chloramphenicol. At this point $\beta - gal_{activity}$ becomes constant. Since, glucose is not an inducer molecule for inducible gene regulation [36]; β-galactosidase is not produced to a notable level and $\beta - gal_{activity}$ is approximately zero.

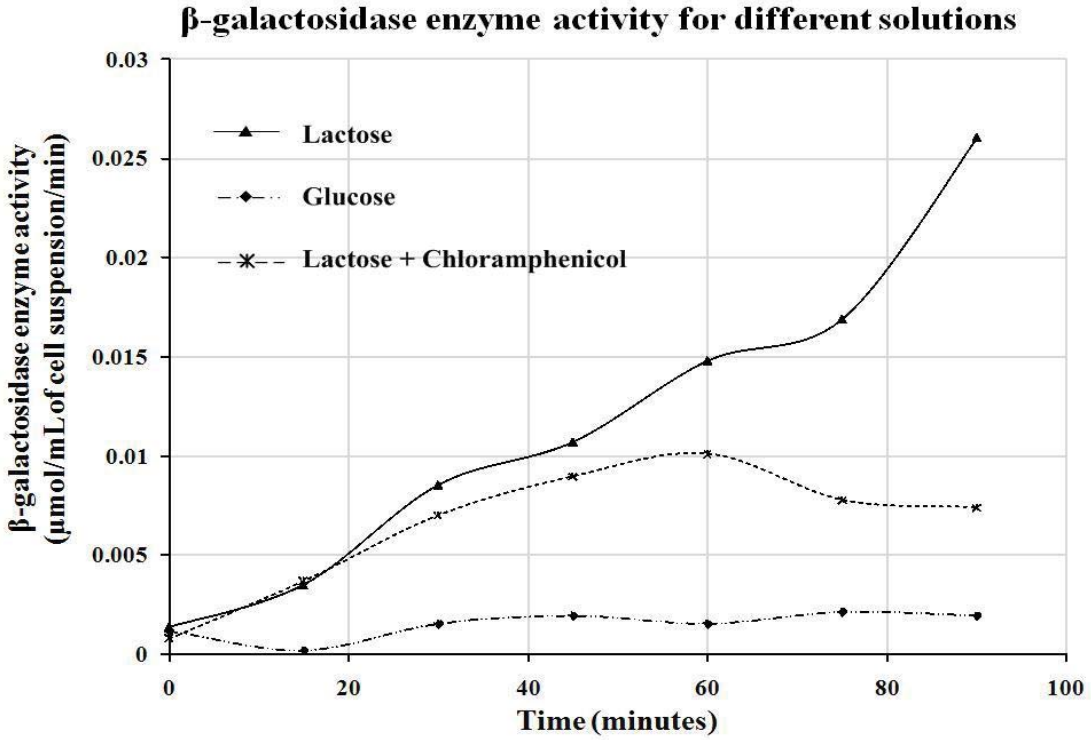

Fig. 5. 8. Rate of β-galactosidase enzyme activity for lactose, glucose and lactose + chloramphenicol.

5.4 VALIDATING ELECTRONIC DESIGN BY CORRELATING CIRCUIT RESULTS WITH BIOLOGICAL EXPERIMENT OUTCOMES

The cytomorphic circuit mimicking regulation of the gene expression process is capable of predicting cellular responses under different conditions. In order to prove this, simulation outputs of the inducible gene expression circuit presented in Fig. 3.5, Chapter 3 are compared with biological experimental results carried out for observing β-galactosidase enzyme activity. The enzymatic activity is directly proportional to the β-galactosidase enzyme protein level [110]. Higher activity corresponds to higher enzyme concentration and vice versa. Therefore, protein concentrations for different

electrical input conditions are illustrated to be analogous to $\beta - gal_{activity}$ under corresponding biological inputs.

Electronically: The inducer molecule concentration α_{ind} in Fig. 3.5 is assigned "High: 1.2V" and "Low: 0V" values to represent presence and absence of an inducer molecule (lactose) respectively. In order to compare the electronic circuit response with the biological experimental results, $\beta - gal_{activity}$ for 5% lactose solution and 5% glucose are analogous to protein concentration with and without an inducer molecule respectively. Fig. 5.9 depicts simulated protein concentration after translation when the inducer molecule level is high, on the left y-axis and $\beta - gal_{activity}$ for lactose on the right y-axis. Similarly, Fig. 5.10 shows simulated protein concentration after translation when the inducer molecule level is low, on the left y-axis and $\beta - gal_{activity}$ for glucose on the right y-axis. The electrical time scale (μs) is followed by the biological time domain (minutes) on the x-axis of both figures.

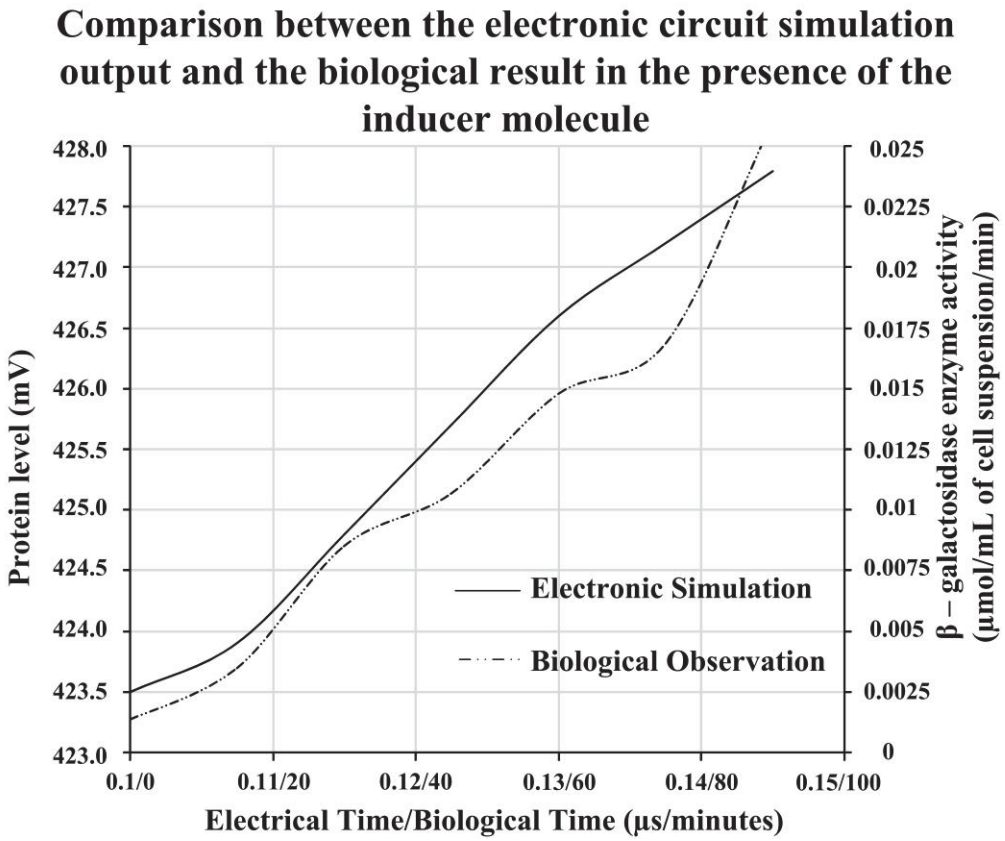

Fig. 5. 9. Predicted cellular response by electronic circuit design (solid line) for high inducer input and biologically observed *E.coli* behavior (dotted line) in presence of inducer molecule.

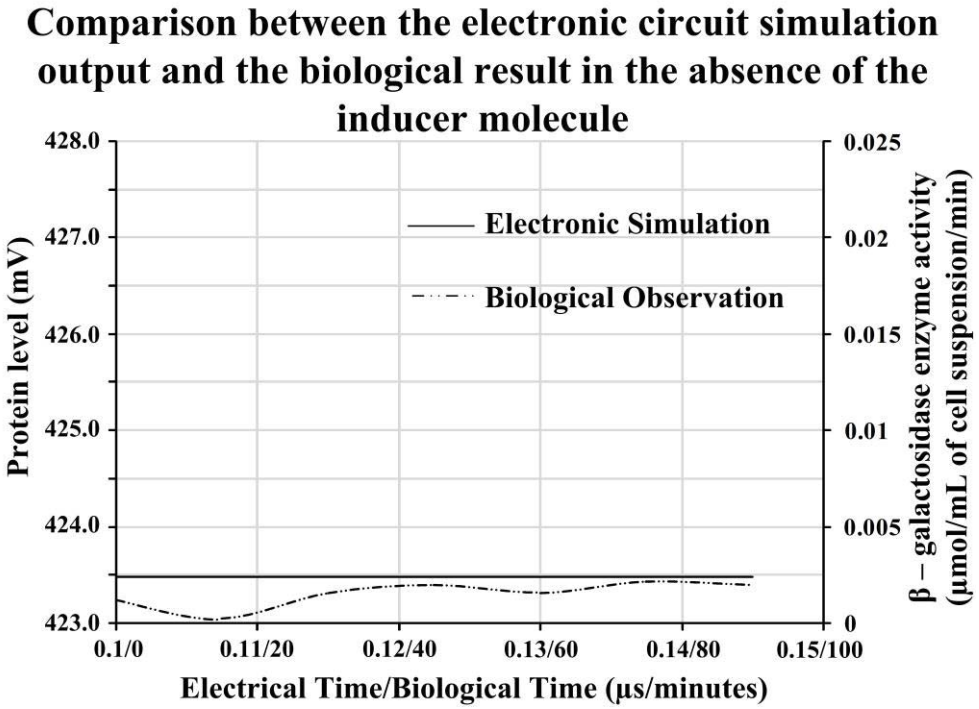

Fig. 5. 10. Predicted cellular response by electronic circuit design (solid line) for low inducer input and biologically observed *E.coli* behaviour (dotted line) in absence of inducer molecule.

miRNA attaches to the complementary mRNA and degrades the protein level. When miRNA is substantially less or not produced and inducer input is high, the protein level increases. Once miRNA is synthesized, the protein starts to degrade. This phenomenon is biologically equivalent to $\beta - gal_{activity}$ in the presence of chloramphenicol. The first gene transcription is initiated by adding 5% lactose, but protein formation is stopped by the chloramphenicol. In Fig. 5.11, the left y-axis shows a protein concentration (after the translation stage) in both the presence and the absence of miRNA. On the right y-axis, $\beta - gal_{activity}$ is plotted for lactose + chloramphenicol. Enzyme formation and inhibition stages are highlighted. The electrical time scale (µs) is followed by the biological time domain (minutes) on the x-axis.

In Fig.5.11, four phases are highlighted as 'a', 'b', 'c' and 'd'. The simulated protein level before and after translation inhibition by miRNA is highlighted as 'a' and 'b' respectively. β-galactosidase enzyme activity before chloramphenicol addition is marked as 'c', while 'd' shows the decrease in $\beta - gal_{activity}$ by chloramphenicol (i.e. β-galactosidase protein translation inhibiton by chloramphenicol).

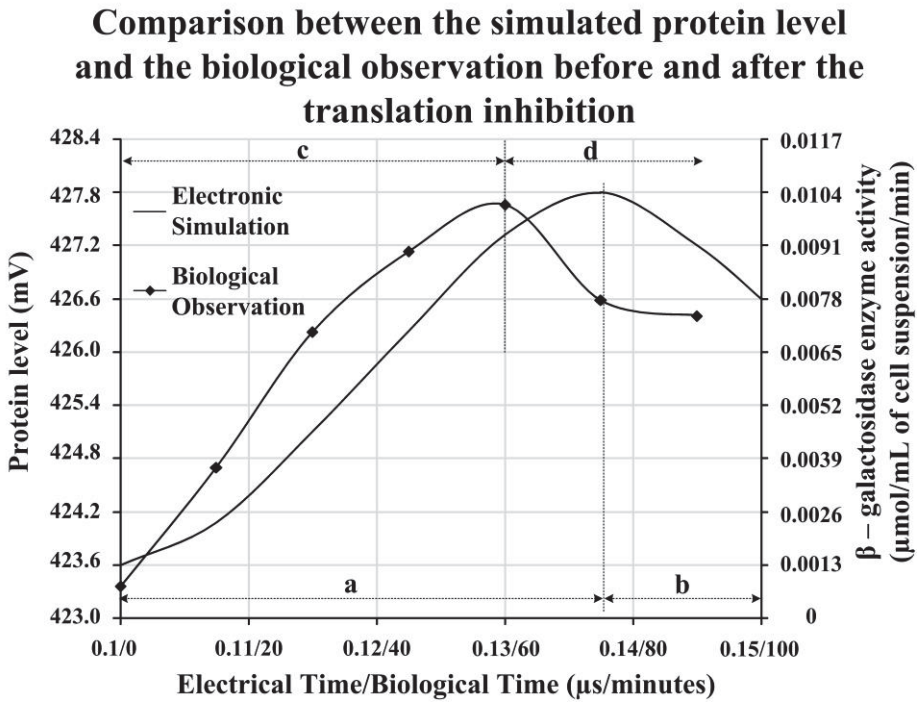

Fig. 5. 11. Effect of miRNA (translation inhibitor) on protein level (solid line) and effect of chloramphenicol (translation inhibitor) on *E.coli* behaviour (solid line with marker).

Results plotted in Figs. 5.9 – 5.11 satisfy: (1) cytomorphic circuit design validation as the electronic simulation outputs and the experimentally observed outcomes are comparable, and (2) the proposed cytomorphic circuit mimicking gene expression regulation mechanism is capable of predicting actual cellular response. When a biological experiment is performed there is some percentage of human and instrumental error expected. Even a very small percentage change of chemical composition can affect the results, but the overall response of simulated and the experimental results are similar as can be seen in Figs. 5.9 – 5.11. The circuit takes only a few micro seconds to envisage cellular behaviour. On the other hand, the biological experiment requires several days (weeks) to examine the response. Hence, this research builds up a way to electronically monitor DNA-protein interactions swiftly and with minimal effort.

5.5 VLSI FABRICATION OF THE NEUROMORPHIC CIRCUIT

To enable development of highly miniaturized integrated biomimetic circuits, reduction in the size of the electronic circuitry is essential. In this thesis, neuromorphic

circuit design mimicking the neural chemical synaptic transmission process controlling neuron-to-neuron communication (illustrated in Chapter 4, Fig. 4.7 and Fig. 4.8) is fabricated in VLSI using 0.13μm IBM technology. The IBM 130 nm CMOS technology is a low-cost versatile process with mask layers that enable fabrication of various passive and active devices. Input signals are applied to the chip and the circuit results are measured by using a Tektronix TDS 1002 two channel digital storage oscilloscope. The VLSI layout and fabrication details of these biomimetic circuits are discussed in the following subsections along with the observed oscilloscope results.

5.5.1 Layout and Fabrication Details

A chip photomicrograph of the neural synaptic transmission presented in Chapter 4 (Fig 4.7 and Fig. 4.8) is shown in Fig. 5.12. The chip areas for the temporal summation circuit (illustrated in Chapter 4, Fig. 4.7) and spatial summation circuit (illustrated in Chapter 4, Fig. 4.8) are 466μm * 189 μm (0.088 mm^2) and 466μm * 403 μm (0.188 mm^2) respectively excluding bonding pads. These circuits are numerically labelled and mentioned in the figure. The fabricated memristor emulator labelled in Fig 5.12 is the fabricated circuit of the memristor emulator circuit design illustrated in Chapter 4, Fig. 4.9. Capacitors are fabricated as single MIM capacitors which are enclosed between E1 and LY layers with QY as the top plate of the capacitors. E1 and LY are thick copper and aluminium metal layers respectively used by IBM CMOS8RF technology for fabrication [55]. Capacitance value is set by using the following nominal value equation as stated in the IBM CMOS8RF design manual [55]:

$$C_N = \left(C_A * L * M\right) + \left(C_P * 2 * \left(L + M\right)\right) \ fF \tag{5-9}$$

where C_N is the required capacitance value in femto Farad (*fF*), C_A is the area capacitance = 2.05 fF/μm^2, C_P is perimeter capacitance = 0.157 fF/μm^2, while L and M are the QY layer design length and width in μm respectively [55]. The transistors are fabricated as regular FET devices. Resistive devices are designed using p+ polysilicon layer and resistor terminals are connected by M1 layers.

Fig. 5.13 shows an inset view of the temporal summation circuit (synaptic transmission). The major parts are also labelled in the figure. The resistors are not

visible due to the LY and E1 fill layers (during fabrication). The operational amplifier detailed circuit design that is used for VLSI fabrication is mentioned in Appendix B.

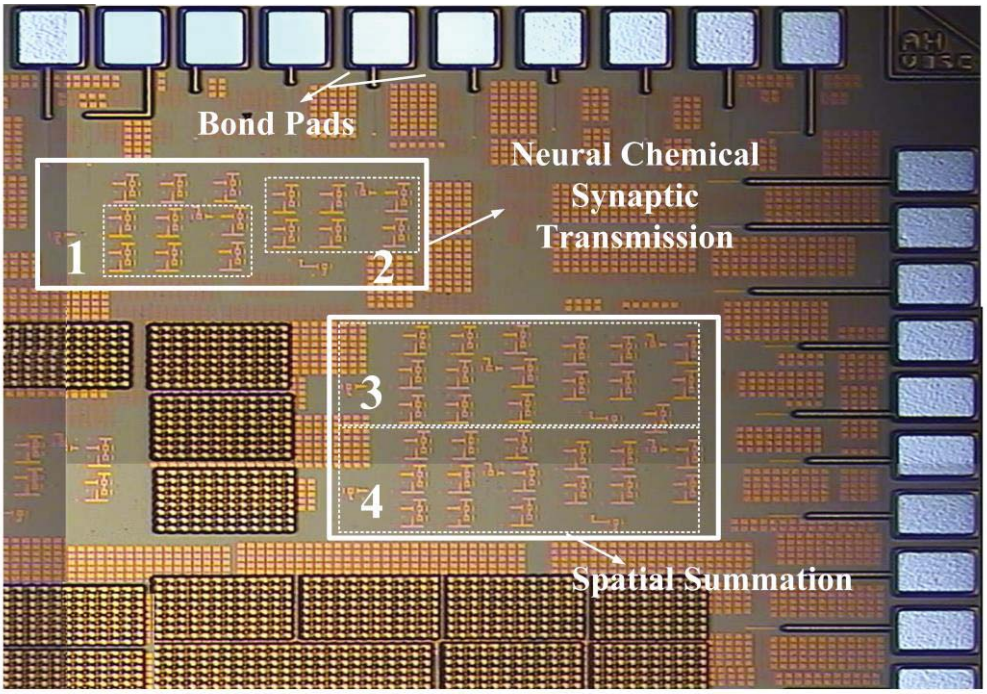

Fig. 5. 12. VLSI fabricated chip photomicrograph. Different sections of the biomimetic circuits are highlighted in square boxes and labelled numerically. These labelled sections are mentioned below the diagram.

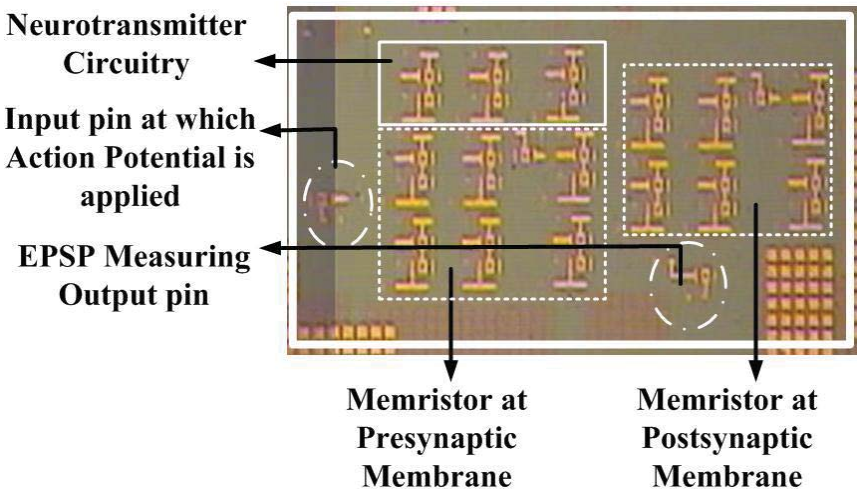

Fig. 5. 13. Inset view of temporal summation circuit from Fig. 5.12.

5.5.2 Test Setup

The chip is mounted on a "Test and Burn-In PGA socket". The external setup for the chip is done on a breadboard. Chip connections on the breadboard are captured on the left of Fig. 5.14. The top right picture shows chip mounted on a test & burn-in PGA socket, while the back aspect of the socket with soldered wires is shown at bottom right of the figure. This is general way of testing the chip because when the chip comes from industry after fabrication there are no external connections. Wires are soldered in order to connect the input and output pins to input sources and oscilloscope respectively.

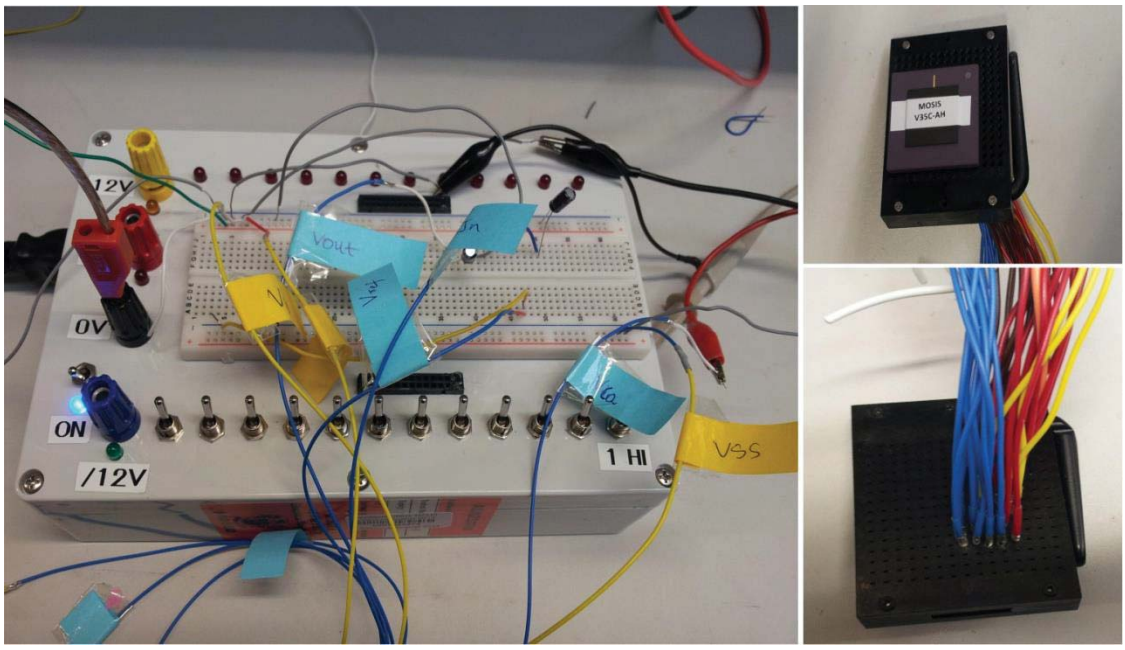

Fig. 5. 14. Chip connections and PGA socket

5.5.3 External Inputs to the Circuit

When the action potential signal V_{ap} is high, V_{Ca_i} (voltage corresponding to the internal Ca^{2+} ion concentration) starts to rise up. When it becomes greater than the reference voltage V_{ref} that is required to fuse the synaptic vesicles, V_{ACh_s} (buffered ACh) changes the postsynaptic membrane potential V_m. As a result, *EPC* is produced and the excitatory postsynaptic potential *EPSP*, due to *EPC*, appears on final output pin of the chip.

i. Action Potential Signal

An action potential is a rapid and transient electric impulse which occurs all-or-none. This input signal (V_{ap}) is represented by a square wave. Two types of action potential signals are required: continuous and single shot. In order to observe *EPSP* temporal summation occurring at the output pin of the chip, continuous V_{ap} is needed. An **LG FG-7002C Sweep/Function generator** is used to generate a square wave signal at time interval of 2 ms and 1.2V amplitude**.**

A pulse wave that is high for 1 ms is generated from a **Tektronix AFG3022 Dual Channel Arbitrary/Function generator**. This single shot signal is needed to capture the neuron potential for a single synaptic transmission and *EPSP* spatial summation.

ii. Extracellular Calcium Ion Concentration

On the arrival of an action potential, a signal representing an extracellular calcium ion concentration (V_{Ca}) is passed to the integrated circuit. It is a 0.47 to 0.5 V sinusoidal signal. The frequency of this external input is set to 100 Hz. The required signal, analogous to the extracellular Ca^{2+} concentration, is generated by an **LG FG-7002C Sweep/Function generator.**

iii. Reference Voltage

A reference voltage (V_{ref}) is needed at the inverting pin of a comparator inside the chip. This circuit node is connected to a bonding pad so that the required reference voltage can be applied externally. It is set to 0.42V applied by a **HY 3003D-3 DC power supply.**

Two capacitors with a value of 1μF are connected externally due to its large size. One capacitor is connected between the final output pin of the chip and ground, while the other is connected between an internal circuit node and ground. These capacitances are analogous to the biological membrane capacitance of a neuron. V_{DD} is set to 1.2V.

5.5.4 Oscilloscope Results

Input signals are applied to the chip and the circuit results are measured by using a **Tektronix TDS 1002 two channel digital storage oscilloscope.** Measured oscilloscope results are as follows:

i. Temporal Summation of neuron potentials

Due to the continuous arrival of V_{ap} continuous pulses, the electric potentials generated by the neuron are added temporally. This behaviour is observed at the output pin of the chip and is captured on the oscilloscope as shown in Fig. 5.15.

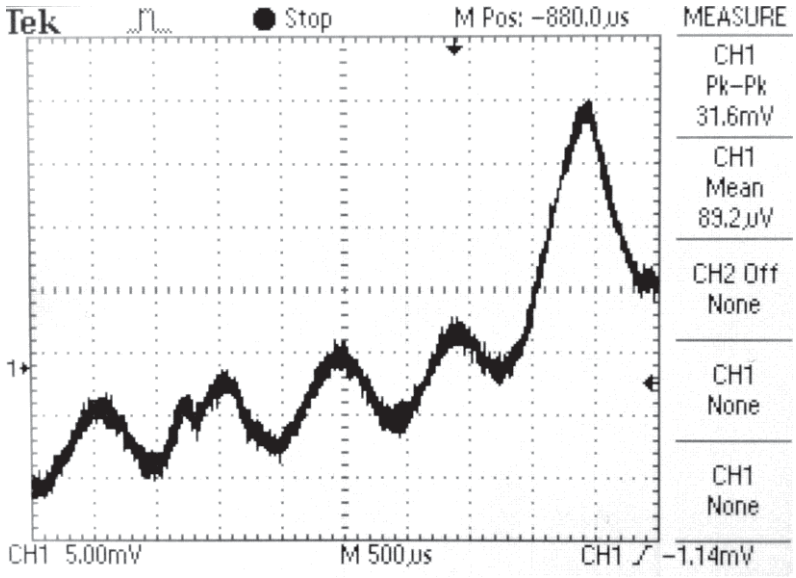

Fig. 5. 15. Chip output of the synaptic transmission circuit presented in Chapter 4, Fig. 4.7. Temporal Summation of *EPSPs* is observed at output pin of the chip for continuous action potential input signal.

ii. Spatial Summation of neuron potentials

When action potential and extracellular Ca^{2+} ion signal inputs are applied to two separate chemical synaptic transmission circuits, spatial summation of the potential at the output pin occurs. In order to check this phenomenon, two similar circuit designs analogous to a biocellular chemical synaptic transmission process at two separate neurons are integrated on the chip. A **Tektronix AFG3022 Dual Channel/ Arbitrary/Function generator** is used to produce V_{ap1} and V_{ap2}. V_{Ca1} and V_{Ca2} are

generated using an **LG FG-7002C Sweep/Function generator.** In Fig. 5.16 spatially summed *EPSPs* are captured on CH1 (channel 1 of oscilloscope), while individual *EPSP* is captured on CH2 (channel 2 of oscilloscope).

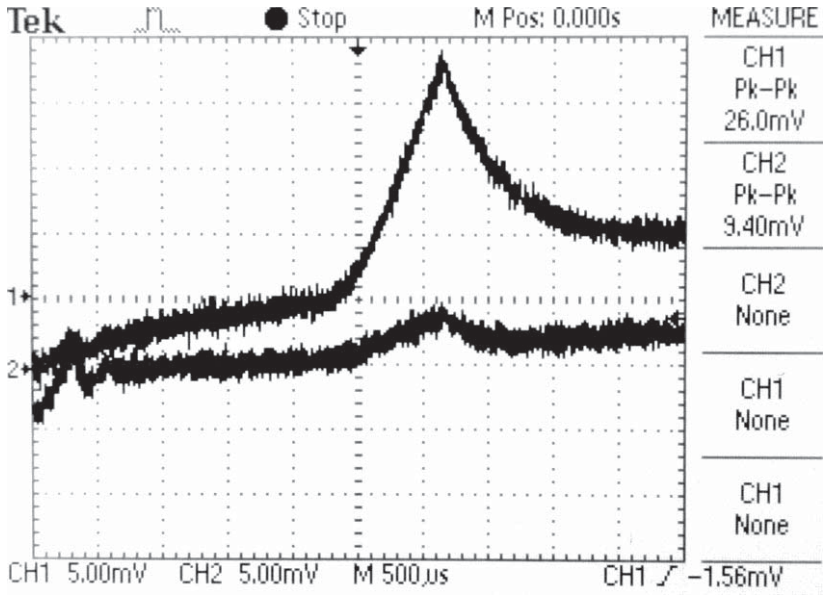

Fig. 5. 16. Chip output of the *EPSP* spatial summation circuit presented in Chapter 4, Fig. 4.8. *EPSPs* are summed spatially when a single action potential pulse is applied to two different synapses.

The overall power dissipation is around 330uW with a significant component of this power budget being consumed by the bipolar devices. The highly efficient human brain on the other hand, has been estimated to require around 20 W [119] for its large number of neurons and synapses. In particular, power consumed by the chemical synaptic transmission process is known to be around 2.8×10^{9} ATP/sec per neuron for a 4 Hz frequency stimulation [120]. Bio-cells operate by consuming ATP (Adenosine Triphosphate), a form of biological fuel present inside living organism [121]. Converting into joules/sec [51], [62] per neurotransmitter per neuron at 100Hz, in order to compare with the silicon chip, the molecular fuel consumption is estimated to be around 3.6×10^{-9} W. The fabricated chip occupies around 0.47 mm^2. of silicon area using the 130 nm process with each memristor emulator occupying only 0.02 mm^2. The temporal summation neural synaptic circuit (illustrated in Chapter 4, Fig 4.7) occupies 0.088 mm^2, while the spatial summation circuit (illustrated in Chapter 4, Fig. 4.8) occupies 0.188 mm^2. The connection to bond pads (for connecting input and output pins) has an approximate area of 0.194 mm^2, thus making a total chip area of 0.47 mm^2.

The memristor emulator area (0.02 mm^2) is included in the temporal and spatial summation circuit areas. The chip foot-print will thus be vastly reduced for technology with much smaller node-size. Since actual physical memristor size can be scaled down to 10 nm [122], significant reduction in the overall area and power consumption can be achieved by using an actual physical memristor. The overall power efficiency and die size of the silicon circuit will thus improve considerably with future technological advancement.

5.5.5 Circuit Design Validation

In order to validate the electronic circuit model developed for the neural synaptic transmission process, chip results of temporal summation and spatial summation obtained from Fig. 5.15 and Fig. 5.16 respectively are compared with experimentally reported data. A graph plotted in Fig. 5.17 illustrates the behavioural response comparison between the temporal summation of *EPSP*s for electronically simulated outputs and experimentally reported data taken from [85]. The *EPSP* magnitudes for electronic simulation and biologically observed results are shown on the left and right y –axes respectively, while time duration is mentioned on the x-axis. The simulation from the proposed model appears to be similar to the experimental observation.

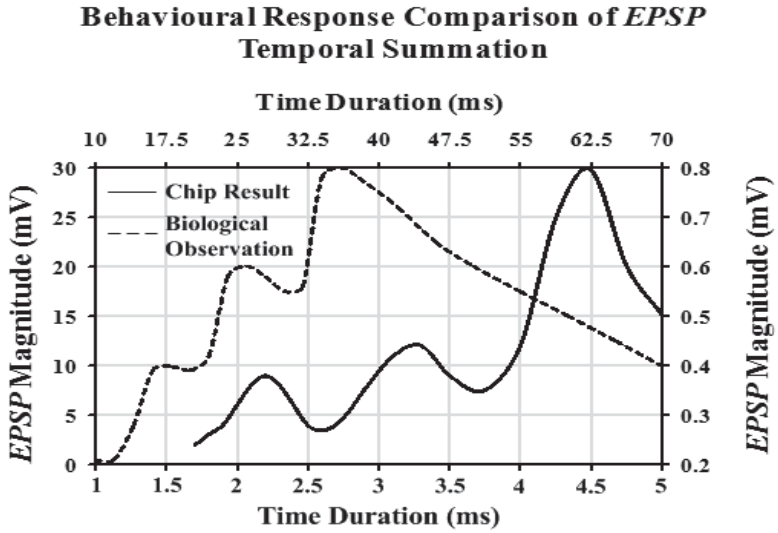

Fig. 5. 17. Temporal summation of *EPSPs* for chip output (solid line) and experimentally reported data (dotted line). The biological data is taken from [85]. Left y-axis represents postsynaptic potential amplitude obtained from oscilloscope results, while right y-axis shows the amplitude for biologically observed results. Time duration is mentioned on x-axis.

The spatial summation of the *EPSPs* resembles the experimentally recorded data for spatial summation as plotted in Fig. 5.18. Biological data is taken from [85]. The *EPSP* magnitudes for oscilloscope outputs and biologically observed results are shown on the left and right y –axes respectively. The bottom x-axis shows the time duration of the electronic output, while the biologically observed time duration is mentioned on the top x-axis. The time duration of the spatial summation is more as compared to the biological results, due to the applied action potential pulse signal with an initial "0" in its pattern. An overall comparison of the chip results and the experimentally reported data validates the proposed electronic circuit model mimicking the neural synaptic transmission process.

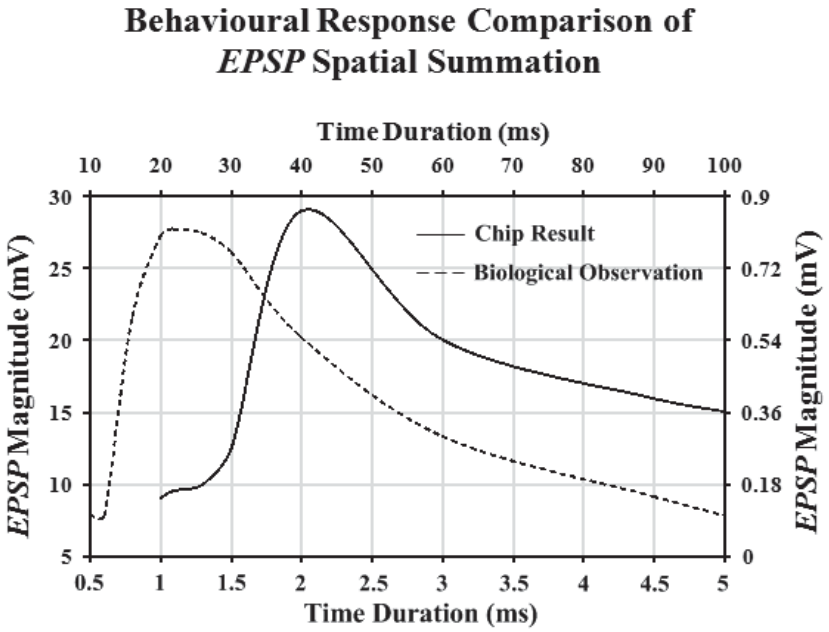

Fig. 5. 18. Spatial summation of *EPSPs* for electronic chip output (solid line) and experimentally reported data (dotted line). The biological data is taken from [85]. Left y-axis represents postsynaptic potential amplitude obtained from electronic results, while right y-axis shows the amplitude for biologically observed results. Time duration for electronic results is mentioned on bottom x-axis, while top x-axis shows biological time duration.

From neurobiological data unitary *EPSP* peak is approximately 0.2 mV for motor neuron [85] and 0.25 mV for hippocampal pyramidal neuron [123], [124]. *EPSP* peak after summation is approximately 0.8 mV [85]. Hence, individual *EPSP* ranges from 25 to 31.25 % of summed *EPSP* in neurobiological observation. From the silicon based

results (oscilloscope traces) it can be seen that this percentage is 29.7% (=[9.4/31.6]*100) for temporal summation and 36.1% (=[9.4/26]*100) for spatial summation. The relative temporal and spatial *EPSP* summation responses of the silicon emulation are thus quantitatively close to the neuro-biological experiment, as illustrated in Fig. 5.19.

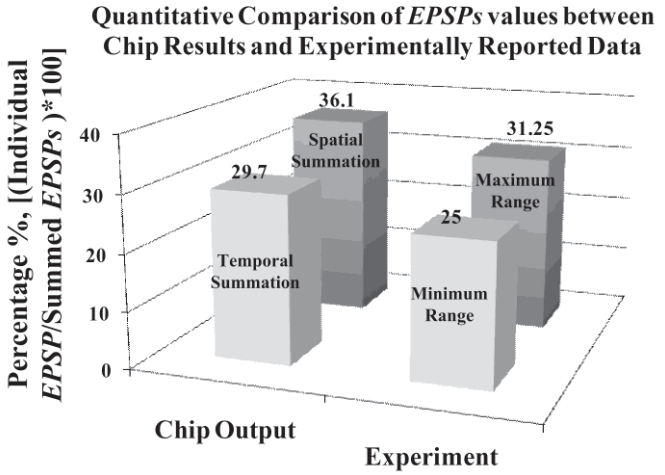

Fig. 5. 19. Bar chart comparison of *EPSP* summation between electronic chip results and the neurobiological data taken from [85], [123], [124].

The temporal lag of biological observations compared to chip results/simulations in Figs. 5.17 and 5.18, can, in general, be attributed to the slower and orders of magnitude variation in the time-scale of the cellular bio-chemical process dynamics [125], [126]. Also, setting the V_{Ca} frequency at 100 Hz for suitability (compatibility) with memristor emulator [82] is somewhat high in the biological domain [127]. In addition, there is also a random temporal variation in the concentration of the biological species involved in the chemical synaptic process.

Since, the biological experimentation is performed for testing the validity of the cytomorphic circuit design developed in this research, VLSI chip fabrication is not carried out for the cytomorphic circuit. The cytomorphic circuit is designed to simulate cellular response of living organisms. In order to predict and explore behaviour of cellular mechanisms or gene circuits, the simulation itself plays an important role. By changing circuit parameters and inputs analogous to biological parameters, the cellular response is predicted quickly. On the other hand, the fabricated chip even working with maximum efficiency will show results as predicted by the simulations. That is the

reason the *Ecoli* experiment is performed in order to validate the cytomorphic circuit functionality. Layout details have been provided in the Appendix D so that the chip can be fabricated in future. Clean DRC rule checks mentioned in Appendix D verifies that there is no layout error and the fabrication can be carried out without any problem. The results obtained from the fabricated chip will be microRNA and protein concentrations in terms of voltage and can be measured by oscilloscope.

5.6 CONCLUSION

A biological experiment aimed at examining and analysing the cellular response of bacterium *E.coli* under various environmental conditions is carried out. The cytomorphic circuit designed for gene expression mechanism is simulated for electronically analogous inputs. *E.coli* response to environmental variations and electronic simulation outputs are similar to a great extent. Thus, the designed cytomorphic circuit model is valid and is capable of observing a cellular response within a time scale of micro seconds instead of hours, days or weeks thus saving precious time, effort, and money. Biological experiments can take several weeks or months to complete, starting with the preparation of the appropriate culture, through to the performing of the assay. On the other hand, the cytomorphic circuit (the gene expression circuit model) provides a way to study cellular dynamical characteristics within an extremely short period of time.

VLSI fabrication details and oscilloscopic results of fabricated chips developed for the neuromorphic circuit are discussed. A comparison between the electronic chip outputs and biologically observed results validates the fabricated designs.

CHAPTER 6
BIOELECTRONIC CIRCUITS APPLICATIONS

6.1 INTRODUCTION

There are various biological phenomena that are controlled by neuron-to-neuron communication process caused by the chemical synaptic transmission. One of the consequences of the chemical changes occurring at the postsynaptic neuron after the synaptic transmission process is DNA transcription initiation of the neural genes in the postsynaptic neuron [28]. Hence, the neuromorphic circuit presented in Chapter 4 of the thesis is utilized to model the biochemical pathway of neural protein synthesis in the postsynaptic neuron. A complete VLSI electronic model for neural DNA transcription initiation and protein synthesis is presented in this chapter.

Synthetic gene networks are capable of implementing various electronic functionalities. Hasty in [9] proposed that logic AND gates, oscillators/repressillators and switches can be implemented by interacting two genes and their final products (proteins). However, the gene-protein network is not as simple as it appears. There are millions of interactions taking place within a microscopic living cell. When genes are interrelating their microRNAs are also playing a role in suppressing these genes. In this chapter, electronic designs of two gene oscillators are presented that mimic the relationship between different genes, their newly translated proteins and miRNAs degrading the mRNA transcripts. Oscillator electronic circuit designs are followed by feasibility procedures that can be applied in order to implement the oscillators through synthetic gene network in-vivo or in-vitro.

6.2 NEUROMORPHIC CIRCUIT APPLICATION

A brief overview of DNA transcription initiation process in the postsynaptic neuron due to synaptic transmission is given below, followed by the details of VLSI modelling of this biological process.

6.2.1 Biological Fundamental

When glutamate neurotransmitters bind to receptors at the postsynaptic neuron, Ca^{2+} ion concentration is increased within the neuron due to the opening of the Ca^{2+} permeable channels. One of the major consequences of the Ca^{2+} level elevation is the induction of the DNA transcription process [128]. The process of DNA transcription initiation due to the influx of Ca^{2+} ions in a postsynaptic neuron is illustrated in Fig. 6.1 [28].

All the functional stages of glutamate neurotransmitters are the same as those of Ach, i.e. neurotransmitter synthesis, storage and release [28],[129]. Glutamate is synthesized from glutamine in an enzymatic reaction involving glutaminase (enzyme) [28]. When glutamate neurotransmitters bind to NMDA (*N*-methyl-D-aspartate) receptors [28] at the postsynaptic membrane, Ca^{2+} permeable channels are opened. The Ca^{2+} influx stimulates the Ca^{2+}/calmodulin-dependent protein kinase IV (CaMKIV) [130] by attaching to it. The stimulated CaMKIV phosphorylates the cAMP-responsive element binding protein (CREB) which is an essential activator of DNA transcription [131],[132]. The phosphorylated CREB (pCREB) and the CREB binding protein (CBP), a co-activator, switch on (initiate) the transcription for neuronal gene expression [131]. After the DNA transcription, the protein is synthesized through the usual biochemical pathway [36].

6.2.2 VLSI Model of Ca^{2+} ion Stimulated Postsynaptic DNA Transcription

A VLSI biomimetic circuit model in the form of blocks representing the process of DNA transcription stimulation caused by the postsynaptic Ca^{2+} ion influx is depicted in Fig. 6.2. Since CREB is a protein [28], the "CREB protein synthesis block" represents CREB synthesis from DNA by the gene expression model depicted in Fig. 3.5, Chapter 3. For simplicity, the gene transcription control mechanism is controlled by a single signal. Control 1 and control 2 signals direct the CREB gene and its complementary miRNA gene transcription processes respectively. The output of the CREB protein synthesis block is V_{CREB} which is analogous to the synthesized CREB concentration.

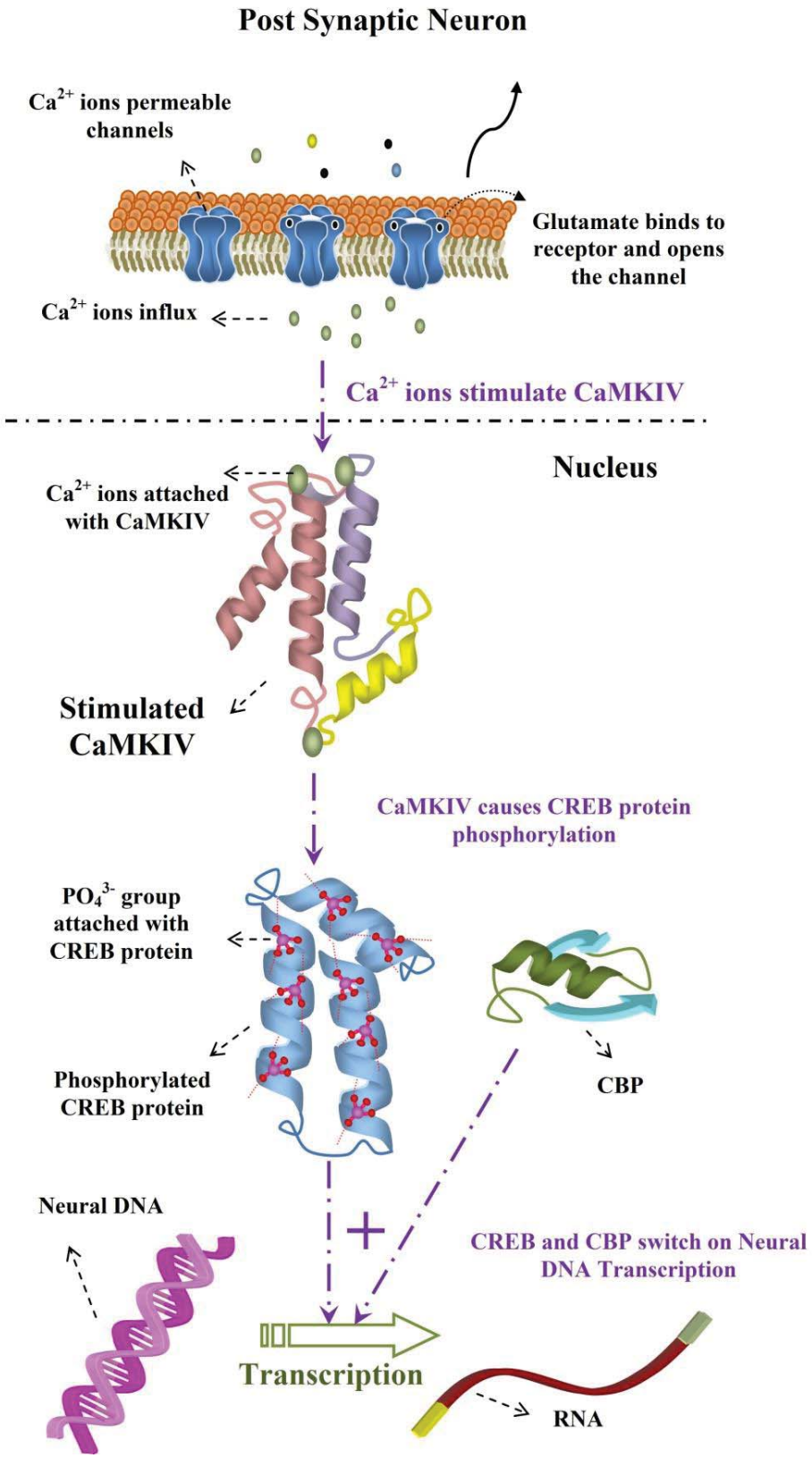

Fig. 6. 1. Biological representation of neural DNA initiation due to synaptic transmission process and protein synthesis inside postsynaptic neuron membrane. The biological representation concept is taken from [28].

The "Glutamate-NMDA synaptic transmission" block in Fig. 6.2 symbolizes the neural synaptic transmission process depicted in Fig. 4.7, Chapter 4. Inputs to this block are V_{Ca}, V_{ap} and V_{gm}, while *EPSP* is its output. V_{gm} is voltage analogous to the glutamine concentration. The weighted summer amplifier of the neurotransmitter synthesis block will have only one input, i.e. glutamine concentration. When the *EPSP* is higher than the action potential threshold (electronically analogous to the MOSFET threshold), switch S_{p1} in Fig. 6.2 is turned on. As a result, CaMKIV (V_{CaMKIV}) is stimulated. A non-inverting weighted summer (not shown in the diagram) is used to uplift summed *EPSP* above MOSFET threshold value as the simulated, as well as, the biologically observed summed *EPSP* is very low as illustrated in Chapter 4. Chemically, the process in which the PO_4^{3-} group is added to a protein molecule is known as phophorylation [106]. Due to the addition of a negative charge, the CREB molecule is chemically reduced. Hence, an electronic model of the reduced molecule [133] is used to mimic the phosphorylated CREB as shown in CREB phosphorylation block. The stimulated CaMKIV, V_{CaMKIV_s} turns on switch S_{p2}. V_{CREB} is passed on as phosphorylated CREB, V_{p_CREB}. Since CREB is a protein, its synthesis is represented by the cytomorphic circuit model of the gene expression mechanisms presented in Chapter 3, Fig. 3.5.

The fourth block of Fig. 6.2 is a "neural protein synthesis block". It is also represented by the cytomorphic circuit model of the gene expression mechanisms presented in Chapter 3, Fig. 3.5. When V_{p_CREB} and V_{CBP} (analogous to a CBP concentration) are present at the same time, neural gene transcription is initiated. Control 3 input in the diagram corresponds to the neural miRNA gene control signal. V_{miRNA} is the neural miRNA concentration that is degrading the neural mRNA, while $V_{protein}$ is the neural protein concentration transcribed synthesized from the neural DNA in the postsynaptic neuron.

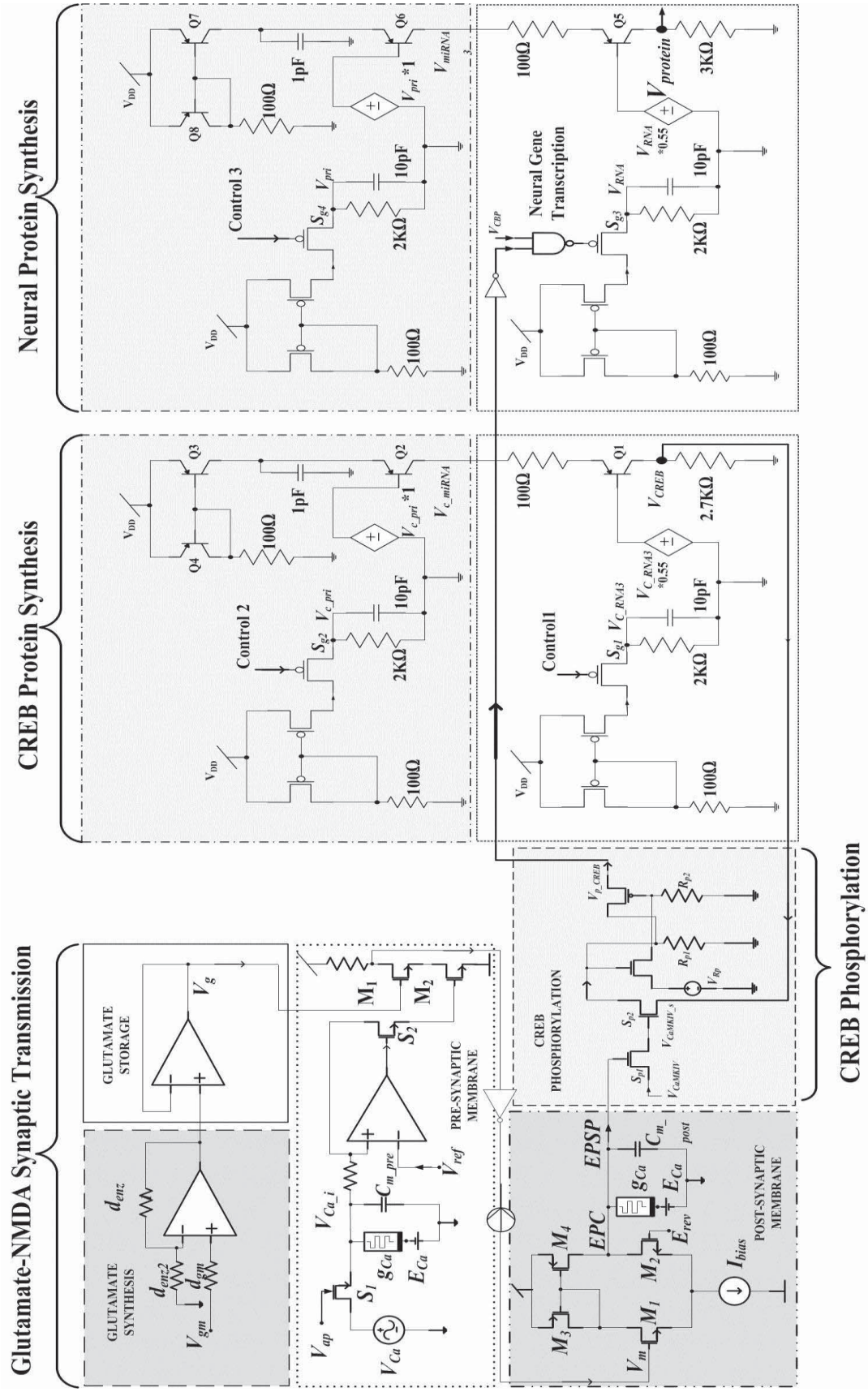

Fig. 6. 2. Electronic circuit model of the neural DNA initiation and protein synthesis inside postsynaptic membrane.

6.2.3 Simulation Results and Discussion

Input and circuit parameter values selected for the electronic model of neural DNA transcription initiation presented in Fig. 6.2 are mentioned below followed by the simulation results of the circuit model.

6.2.3.1 Circuit Parameters and Input Values

Fig. 6.2 circuit simulation is carried out on Mentor Graphics platform using a 0.13µm IBM CMOS process technology. Since it is a combination of cytomorphic (Chapter 3) and neuromorphic (Chapter 5) circuits; circuit parameters and input values are taken from its basic circuits from previous chapters. The only different values are: V_{gm}, control signals 1 – 3, V_{CBP} and V_{CaMKIV}. The glutamate concentration inside cellular plasma is between 7 – 12 mM [134] and 10 mM is taken as the average concentration. The corresponding glutamate concentration level in voltage is 1.2V (by using equation 4-24). By applying the equation of a non-inverting amplifier [50], the glutamine concentration in volts, V_{gm} is set to 0.6V to maintain this glutamate concentration. Control signals 1 – 3, V_{CBP} and V_{CaMKIV} are set as logic HIGH values (1.2V) in order to represent the presence of these molecules. After iterative simulations, V_R is set to 1V and 2KΩ is chosen for R_1 and R_2.

6.2.3.2 Simulation Results

During Fig. 6.2 simulation, when the action potential signal is high, glutamate neurotransmitters are released and Ca^{2+} permeable ion channels on the postsynaptic neuron membrane allow the influx of Ca^{2+} ions. *EPSP* is produced, S_{p1} is switched on and V_{CaMKIV} progresses to interact with the CREB protein. It causes V_{CREB} to proceed for phosphorylation and neural DNA transcription is initiated. mRNA is transcribed from the neural DNA from which neural protein is translated in the postsynaptic neuron. As a result, the inverse relationship between neural miRNA and protein is developed. illustrated in Fig. 6.3. Hence, the neuromorphic circuit is used to model the biochemical pathway of the neural protein synthesis.

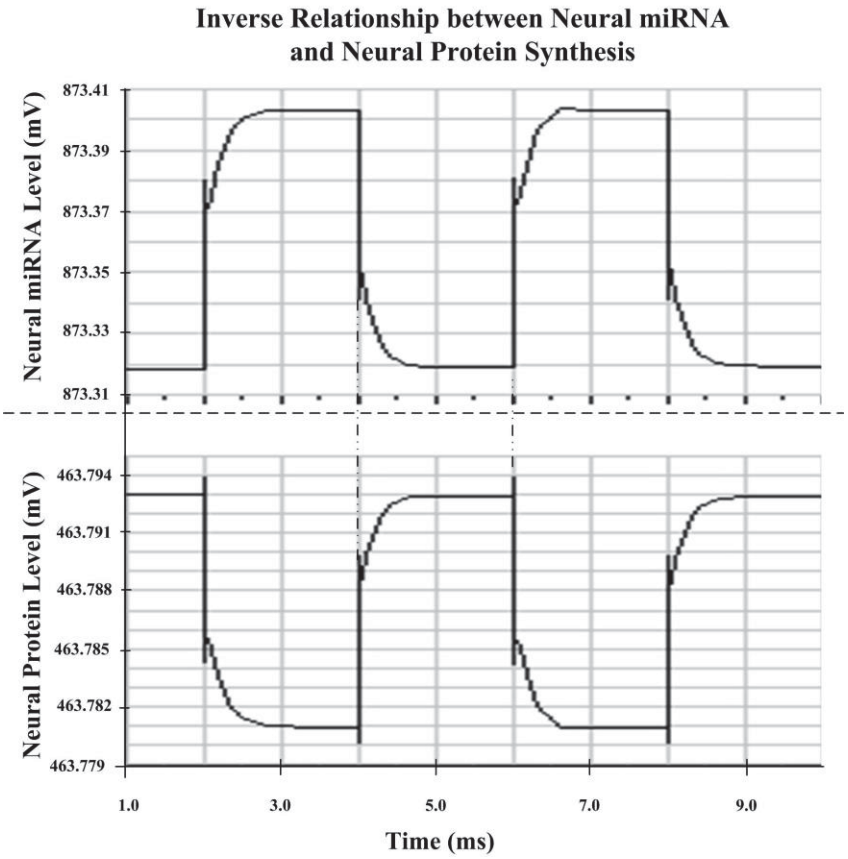

Fig. 6. 3. Inverse relationship between neural miRNA and neural protein. The protein is synthesized after the DNA transcription initiation in the postsynaptic neuron due to chemical synaptic transmission.

6.3 ELECTRONIC CIRCUIT DESIGNS OF GENE – PROTEIN – MIRNA OSCILLATORS/MULTIVIBRATORS

Electronic circuit models that are developed for *gene – protein – miRNA* oscillators/multivibrators utilize the cytomorphic circuit presented in Chapter 3, Fig. 3.5. Electronic circuit for two oscillators are designed: 1) two genes oscillator, and 2) six genes oscillator. Details of these oscillators are illustrated one by one in this section:

6.3.1 Two Genes Oscillator Electronic Circuit

Initially, *gene 1* is transcribed into mRNA from which protein is synthesized. This protein represses the gene from which it is produced. In this way the *gene 1* regulates itself through a negative feedback loop. At the same time, transcription of another gene '*X*' is repressed by *gene 1* protein. *X* generates miRNA transcripts that have

complementary sequences for mRNA of *gene 1*. Thus, with an increase in *gene 1* protein concentration, *gene 1* and *X* are repressed. This ultimately results in decrease in protein concentration of *gene 1* due to negative feedback loop causing *gene 1* and *X* to transcribe. miRNA degrades mRNA of *gene 1* due to which its protein decreases further. When the protein reaches to a level at which it can't repress its own gene and *X*, transcription of these genes is initiated again. This process continues resulting in oscillations. The electronic circuit model imitating this gene – protein – miRNA oscillatory relationship is shown in Fig. 6.4. The synthesized protein output, $V_{protein}$, is input to two NFET switches S1 and S2 through inverters that control the transcription of *gene 1* and *gene X* respectively. Voltage below 0.355 V is inverted to 1 V and above 0.355 V is inverted to 0V by the inverter. The W/L ratios of PMOS and NMOS used in the inverter are 0.16µ/0.25µ and 0.2µ/0.16µ respectively. Transistors size, capacitor and resistor values are mentioned in the diagram. To ensure that the BJT transistors are biased, and the $V_{protein}$ output switches across the transistor threshold value (0.355V), the circuit parameters are set after iterative simulations of the circuit. It is necessary for $V_{protein}$ voltage value to move along transistor threshold value because it controls the transcription of the genes.

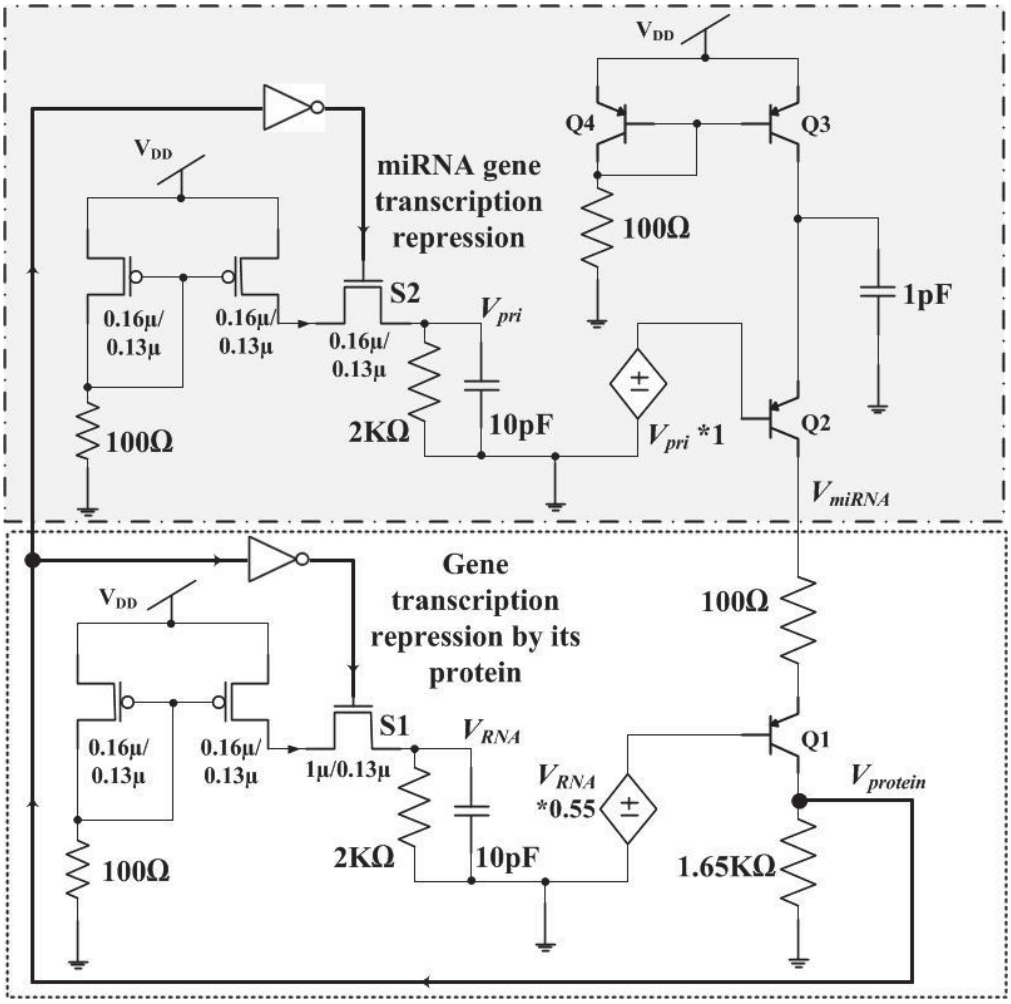

Fig. 6. 4. Electronic circuit model of two genes oscillator. $V_{protein}$ represents protein output of first gene, while V_{miRNA} mimics miRNA output of second gene. $V_{protein}$ represses transcription of *gene 1* and miRNA gene through S1 and S2 NFET switches.

6.3.2 Two Genes Oscillator Simulation Results

The circuit in Fig. 6.4 is simulated in Mentor Graphics and the simulation results are shown in Fig. 6.5. Oscillations are observed in protein and micro RNA concentrations produced from *gene 1* and the miRNA gene. Protein level is controlling the oscillatory behaviour of its own gene and the miRNA gene targeting the *gene 1* mRNA transcripts.

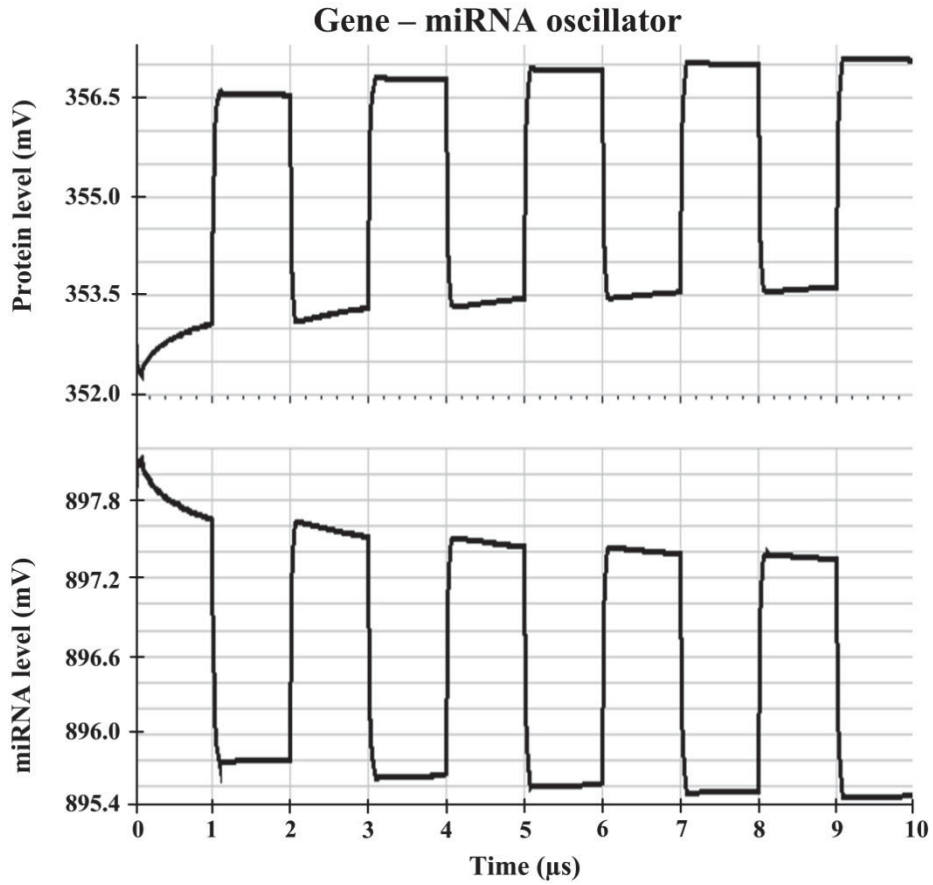

Fig. 6. 5. Oscillations observed for protein level of *gene 1* and miRNA level of the gene degrading *gene 1* mRNA.

6.3.3 Six Genes Oscillator / Multivibrator Electronic Circuit

In this oscillator, there are three genes (*1, 2* and *3*) and their corresponding miRNA genes that are interacting in a distinctive fashion. *Gene 1* plays a very important role in this oscillator circuit. Protein synthesized from *gene 1* is responsible for three processes: (i) auto regulation of its own gene by repressing the transcription of the DNA, (ii) transcription repression of miRNA gene targeting *gene 1*, and (iii) transcription repression of miRNA gene targeting *gene 2*. The oscillatory relationship between *gene 1* protein and the miRNA transcripts that is degrading *gene 1* mRNA is same as described above for gene – miRNA relationship for the two genes oscillator.

Gene 2 transcription is controlled by its own protein, as well as by the protein synthesized from *gene 3*. Protein translated from the mRNA transcripts of *gene 2* induces transcription of its own gene, while *gene 3* protein represses the transcription. At the same time, *gene 2* mRNA are degraded by its complementary miRNA sequences whose gene is repressed by *gene 1* protein. Hence, with an increase protein level of

gene 2 its transcription will be induced, but the protein will be decreased due to its miRNA and repression by *gene 3*. When the transcription of *gene 3* and miRNA attacking *gene 2* is repressed, gene 2 protein starts increasing again resulting in oscillations.

Gene 3 not only represses transcription of *gene 2*, but it also represses its own transcription and transcription of the miRNA gene degrading its mRNA transcripts. The oscillatory relationship of gene 3 and its miRNA gene is same as mentioned above for two genes oscillator. Since, there is inverse relationship between *gene 2* and *gene 3* proteins; two oscillation states are observed at the same time. Hence, the oscillator acts as a bistable multivibrator. The electronic circuit model imitating this unique oscillatory relationship between three genes, their proteins and three miRNA genes is shown in Fig. 6.6. $V_{protein1}$ synthesized from *gene 1* represses *gene 1* transcription through NFET switch S1, and represses transcription of miRNA genes through S2 and S4 switches that are degrading *gene 1* and *gene 2* mRNA transcripts respectively. $V_{protein2}$ is the output from *gene 2* that is degraded by V_{miRNA2}. It induces its own gene transcription. $V_{protein3}$, translated from *gene 3*, represses transcription of *gene 3* and miRNA gene targeting *gene 3* through S5 and S6 NFET switches respectively. A combination of NAND and NOT gate is used to control transcription of *gene 2*. When $V_{protein2}$ is high and $V_{protein3}$ is low, switch S3 is on. While in all other combinations of $V_{protein2}$ and $V_{protein3}$ S3 is off and the transcription of gene 2 is not initiated.

6.3.4 Six Genes Oscillator Simulation Results

The six gene oscillator circuit is simulated in Mentor Graphics and the simulation results are elaborated in this sub section. In Fig. 6.7, the oscillatory relationship between $V_{protein1}$ and miRNA degrading mRNA of *gene 1* is illustrated. Initially, the *gene1* is transcribed to form the protein and the miRNA transcripts attacking *gene 1* are also synthesized. $V_{protein1}$ causes transcriptional repression of its own gene and the miRNA gene producing V_{miRNA1} through switch S1 and S2 respectively. As a result protein synthesis is stopped and its concentration cannot increase due to the fact that mRNA transcripts of *gene 1* are degraded by V_{miRNA1}. Thus, *gene 1* and miRNA gene transcription is reinitiated and oscillations are observed for $V_{protein1}$ and V_{miRNA1} as shown in the simulation results.

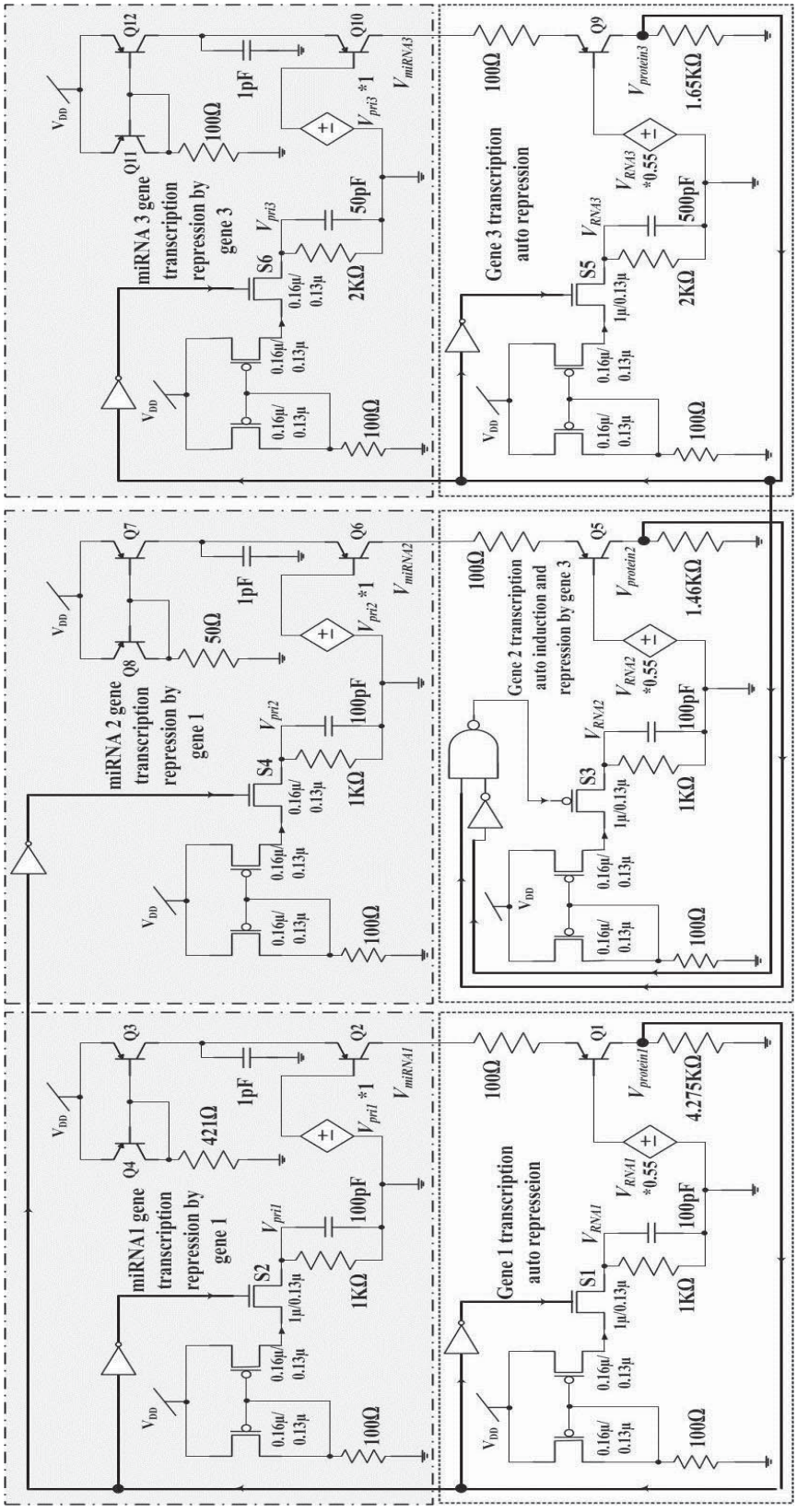

Fig. 6. 6. Electronic circuit model of six genes oscillator. Switches S1, S3 and S5 control transcription of *gene 1*, *gene 2* and *gene 3* respectively. Switches S2, S4 and S4 control transcription of miRNA genes repressing *gene 1*, *gene 2* and *gene 3* at translational level respectively.

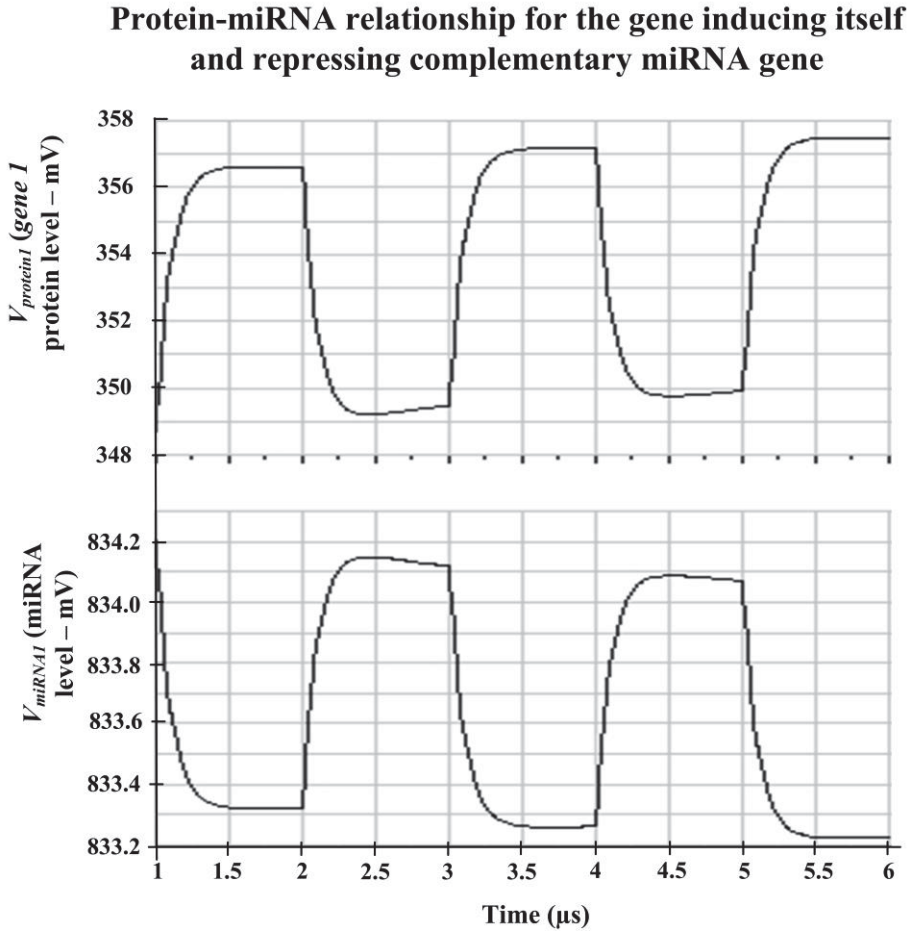

Fig. 6. 7. Oscillation patterns for the concentrations of $V_{protein1}$ (upper plot) and V_{miRNA1} (lower plot), i.e., the protein synthesized from *gene 1*, and the miRNA transcripts degrading mRNA of *gene 1*.

miRNA gene that degrades *gene 2* mRNA transcripts is also repressed by *gene 1* protein at the transcription level. The association between protein of *gene 1* and the miRNA gene attacking *gene 2* is depicted in Fig. 6.8. As expected, the simulation results show inverse relationship between protein '1' concentration, $V_{protein1}$ and the miRNA of *gene 2*, V_{miRNA2}.

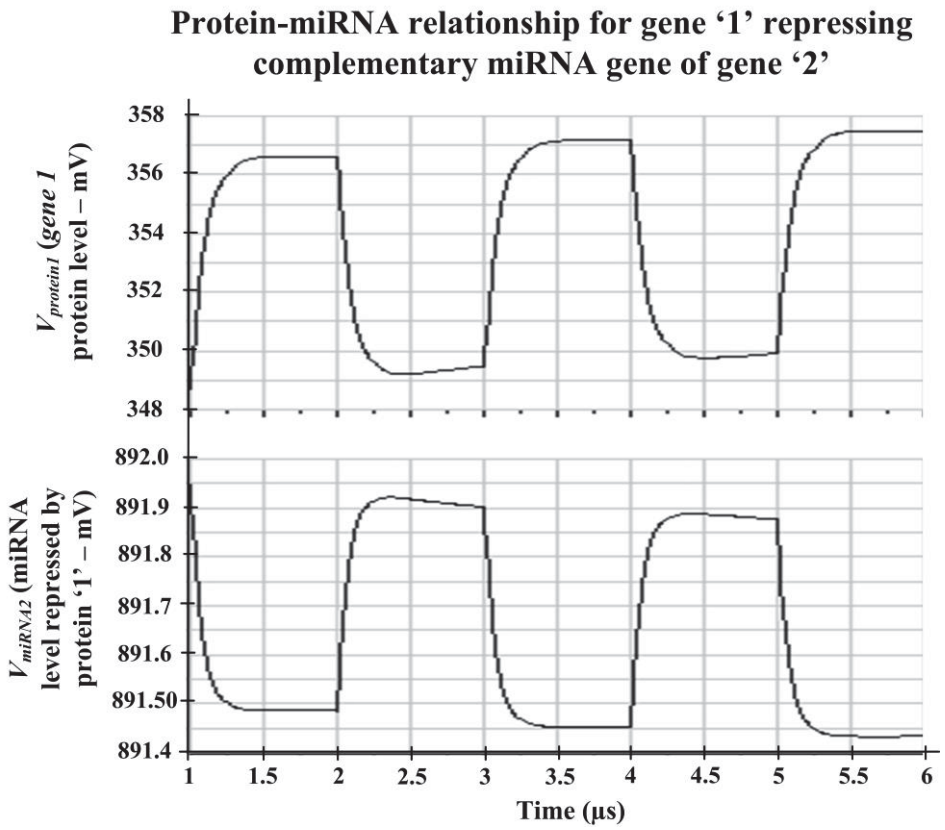

Fig. 6. 8. Oscillation patterns for the concentrations of $V_{protein1}$ (upper plot) and V_{miRNA2} (lower plot), i.e., the protein synthesized from *gene 1*, and the miRNA transcripts degrading mRNA of *gene 2*.

In the six gene oscillator network, third oscillation pattern is produced between $V_{protein2}$ and V_{miRNA2}, i.e. protein '2' (protein of *gene 2*) and miRNA repressing gene 2 at translational level ultimately degrading protein '2'. The results are depicted in Fig. 6.9. This is the usually relationship between the protein and the miRNA concentration of the cytomorphic gene expression circuit.

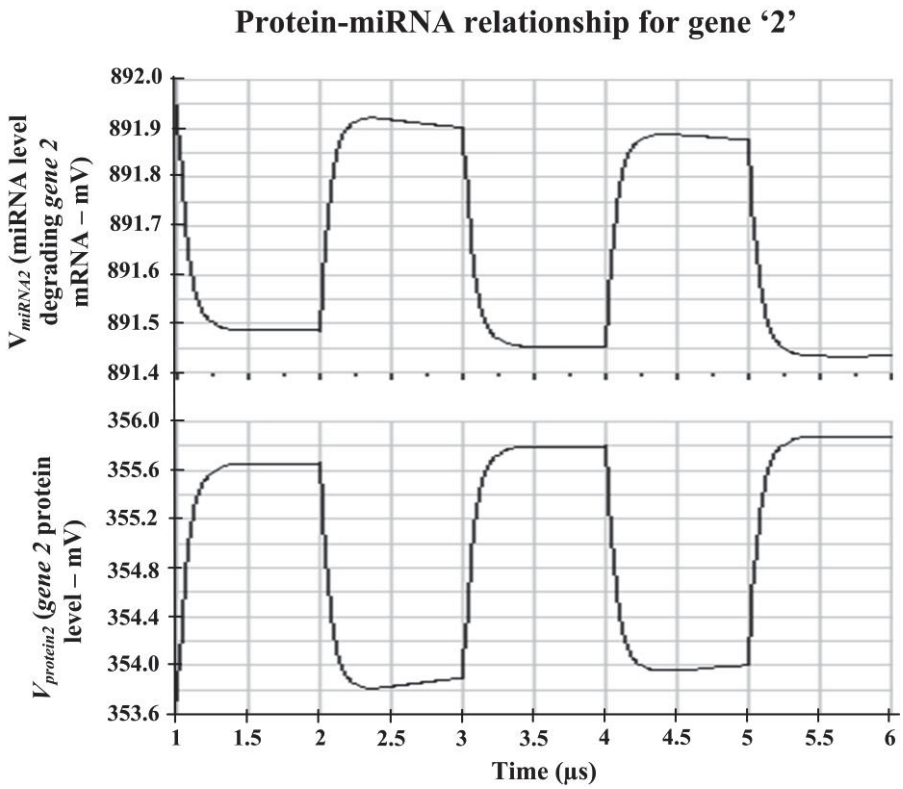

Fig. 6. 9. Oscillation patterns for the concentrations of V_{miRNA2} (upper plot) $V_{protein2}$ (lower plot) and, i.e., the miRNA transcripts degrading mRNA of *gene 2*, and the protein synthesized from *gene 2*.

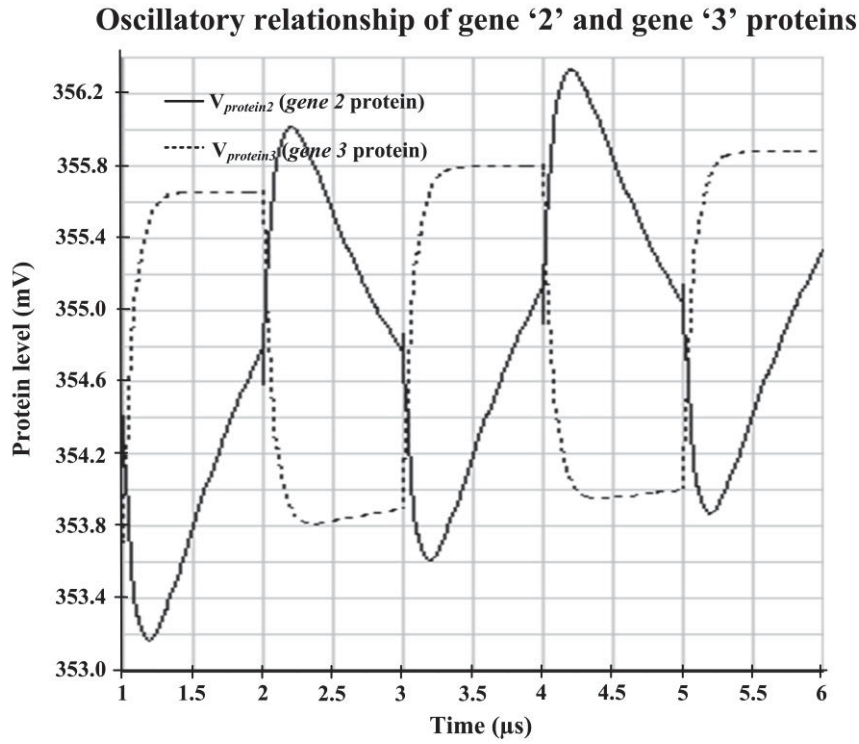

Fig. 6. 10. Oscillation patterns for the concentrations of $V_{protein2}$ (solid lines) and $V_{protein3}$ (dotted lines), i.e., the protein synthesized from *gene 2*, and the protein synthesized from *gene 3*.

The final oscillations are produced for between $V_{protein2}$ and $V_{protein3}$, i.e. protein '2' (protein of *gene 2*) and protein '3' (protein of *gene 3*). Since, $V_{protein3}$ represses gene 2 transcription; two states of the oscillations are observed at the same time and the oscillator can also be termed as a two state multivibrator. The oscillatory relationship between protein '2' and protein '3' is shown in Fig. 6.10. The oscillations for $V_{protein3}$ and V_{miRNA3}, i.e. miRNA concentration degrading *gene 3* are same as depicted in Fig. 6.5 for the two gene oscillator. It is clear from the oscillator circuits results that the cytomorphic circuit mimicking gene expression mechanism is capable to analyse the behaviour of gene – protein – miRNA oscillatory network.

6.4 FEASIBILITY PROCEDURE FOR GENES OSCILLATOR

The electronic circuit designs of gene – protein – miRNA oscillators, or in other words *cytomorphic oscillators* presented in section 6.3 can be implemented in biological cellular environment. A feasibility procedure for each of the cytomorphic oscillators is discussed in detailed in following sub sections.

6.4.1 Feasibility Procedure for Two Genes Oscillator

Hes1 gene synthesizes a protein that acts as a transcriptional repressor for its own gene that transcribes it [135]. *Hes1* mRNA stability is controlled by a microRNA termed as *miR9*. It has complementary sequences for *Hes1* mRNA due to which *miR9* attaches to *Hes1* mRNA and degrades it [136]. The *miR9* gene in the *Hes1 – miR9* oscillator loop is repressed by *Hes1* protein. *Hes1* follows negative repressible gene regulation because in the absence of repressor molecule, i.e. *Hes1* protein, *Hes1* is transcribed. When *Hes1* protein level is high, it represses *miR9* which inhibits *Hes1* protein translation by degrading *Hes1* mRNA. At the same time, *Hes1* gene is also repressed by its protein due to which its level starts decreasing. Thus, with a decrease in *Hes1* protein level, *miR9* and *Hes1* transcriptions are no longer repressed. The process continues and oscillatory behaviour in terms of ups and downs in concentration level is obtained.

The "two genes oscillator" can be implemented biologically in the cells by transfecting the cell with *Hes1* reporter DNA structure: "*pcDNA4-Hes1::ubq–luciferase WT 3'UTR*" and *miR9* precursors: *pre – miR – 9* [135] , [136]. *pcDNA4-*

Hes1::ubq– luciferase WT 3'UTR" and *pre – miR – 9* relationship can be observed through *bioluminescent imaging* [135] , [136]. A diagram showing the unique *Hes1 – miR9* oscillatory process [135] is illustrated in Fig. 6. 11.

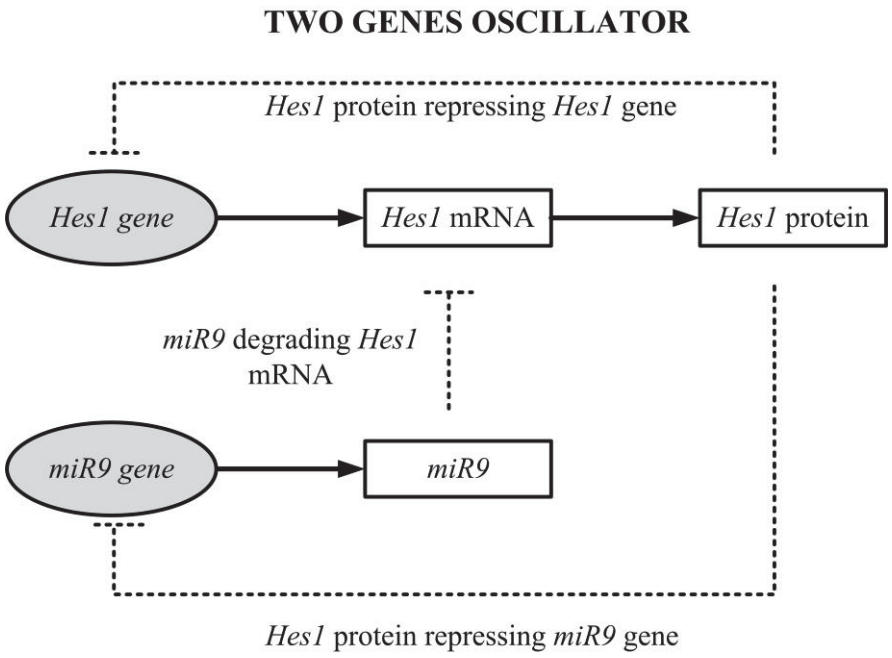

Fig. 6. 11. A block diagram showing relationship between two genes resulting in an oscillatory network. Solid lines show gene expression control at the transcriptional stage (by the protein), while dotted lines shows gene expression control at the translational stage (by miRNA). Arrow headed line shows transcriptional induction, while flat ended lines means repression (transcriptional / translational).

6.4.2 Feasibility Procedure for Six Genes Oscillator

A gene known as *c – myc* involves itself in a very complex gene oscillatory network. The protein synthesized from *c – myc* gene controls the transcription of genes: (i) auto regulation of its own gene by repressing the transcription of the DNA through negative feedback loop [137], (ii) transcription repression of *let 7* gene [138], and (iii) transcription repression of *let 7i* gene [138]. *let 7* and *let 7i* are miRNA genes that represses *c – myc* and *Mash1* genes respectively at translational stage of gene expression [138], [139]. Hence, *c – myc* not only regulates its own protein level [137], but also helps *Mash1* gene, which is a proneural gene, to promote its protein concentration by repressing *let7i* transcription [138], [139].

Proteins synthesized from two different genes control the transcription of *Mash1* [140]: (i) proteins produced from *Hes1* gene represses *Mash1* transcription, and (ii) protein translated from mRNA transcripts of *Mash1* gene induces *Mash1* transcription, i.e., *Mash1* auto regulates itself. Similar to the *Hes1 – miR9* oscillator (two genes oscillator mentioned above), *Hes1* also represses *miR9* gene transcription (miRNA gene attacking the mRNA transcripts of *Hes1* gene), and auto regulates itself through negative feedback loop [135]. A block diagram shows this unique six genes oscillator network in Fig. 6.12.

c – myc and *let – 7* network can be developed biologically in cells by trasnfecting 1a – c – myc fibroblast cells with pre – let – 7a [141]. The oscillatory behaviour of the *c – myc* and *let – 7* can be observed by western blotting [141]. *Mash1 – let7i* relationship can be observed biologically by transfecting HEK293T cells with *let7i* expressing plasmid and GFP-MASH1 3' UTR reporter as carried in [139]. The results can be observed by taking cells GFP fluorescence digital images and analysing the images through ImageJ (or similar) software [139]. Hes1 – miR network can be implemented biologically in the cells by transfecting the cell with *Hes1* reporter DNA structure: "*pcDNA4-Hes1::ubq– luciferase WT 3'UTR*" and *miR9* precursors: *pre – miR – 9* [135], [136]. *pcDNA4-Hes1::ubq– luciferase WT 3'UTR*" and *pre – miR – 9* relationship can be observed through *bioluminescent imaging* [135], [136].

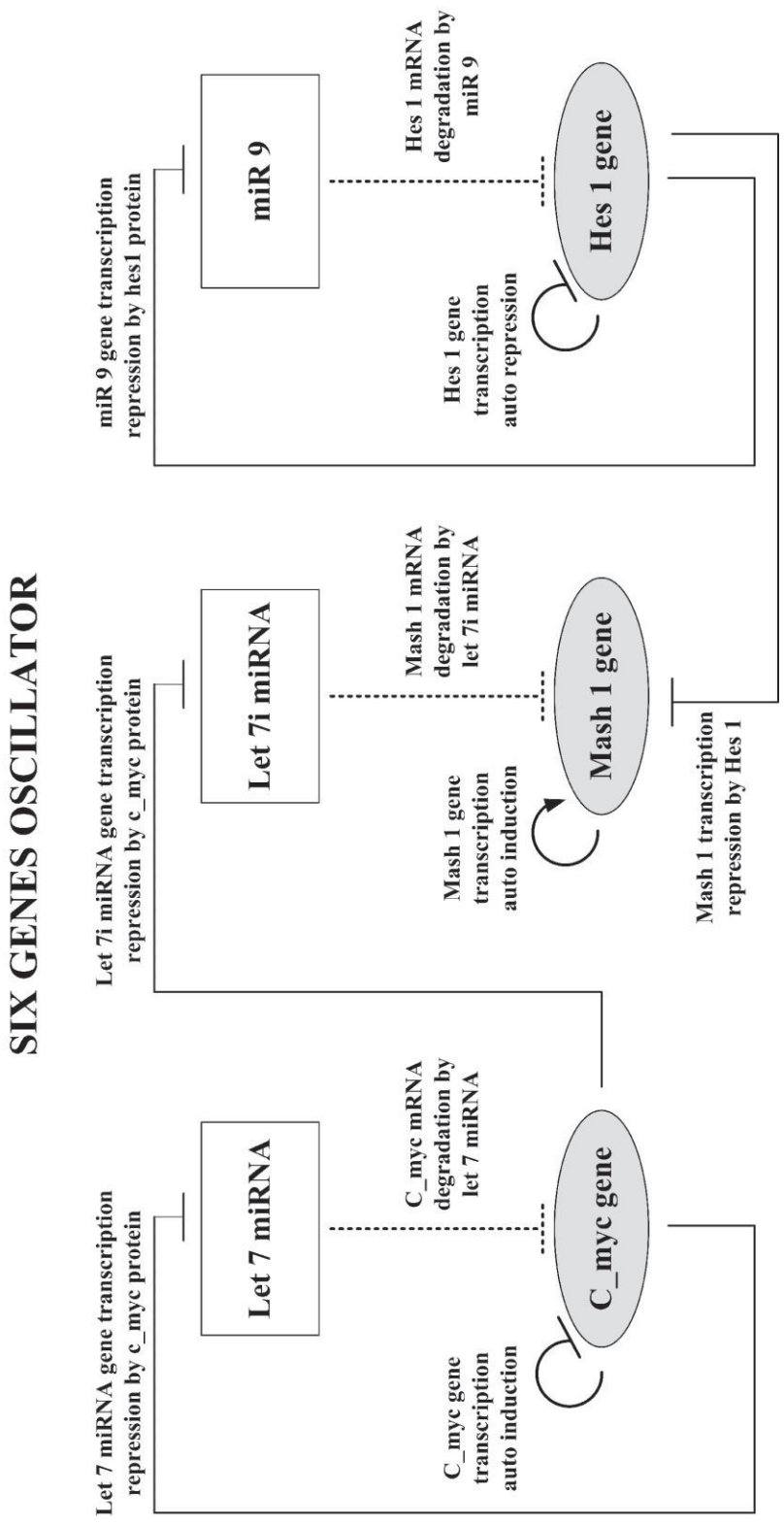

Fig. 6. 12. A block diagram showing relationship among six genes resulting in an oscillatory network. Solid lines show gene expression control at the transcriptional stage (by the protein), while dotted lines shows gene expression control at the translational stage (by miRNA). Arrow headed line shows transcriptional induction, while flat ended lines means repression (transcriptional / translational).

6.5 CONCLUSION

Applications of the neuromorphic and the cytomorphic circuit designs are presented in this chapter. Synaptic transmission process is a key factor in initiating DNA transcription in the postsynaptic neuron. Hence, the neuromorphic circuit design is used to model the biochemical pathway of neural protein synthesis in the postsynaptic neuron. The cytomorphic circuit mimicking the gene expression mechanisms is used to design two genes and six genes electronic oscillator circuit. A feasibility procedure that can be followed in order to biologically implement the gene oscillator circuits is also proposed in this chapter.

CHAPTER 7
CONCLUSION

7.1 SUMMARY

In this fast–moving era of research, engineers are striving hard to establish and enhance a connection between the electronic world and the biological world. Rapid progress in the research and development of bioelectronic circuits is not only bringing innovation to the engineering field, but is also assisting in understanding of biological complexities. Two major types of bioelectronic circuits are: 1) cytomorphic circuits that deal with modelling cellular mechanisms, and 2) neuromorphic circuits that are associated with representing neural activities electronically. In this doctoral research the electronic modelling, analysis, and design of the following biological phenomena in VLSI has been presented:

1. Gene expression mechanisms that involve DNA-protein interactions taking place inside a living cell (cytomorphic circuit) and
2. Neuron–to–neuron communication through the synaptic transmission process (neuromorphic circuit).

A brief overview of the basic fundamentals of these biological processes is given. Analogies between biological parameters and electrical circuit entities are studied and applied in order to imitate the biological phenomena. In the gene expression electronic model, the combined mathematical equations for the processes of protein translation and mRNA degradation by miRNA are analogous to the mathematical representation of the π-model of a common emitter BJT amplifier with emitter degeneration. In the same circuit model, a mature miRNA synthesis phenomenon also mimics the common emitter BJT amplifier π-model. Protein concentrations, after the translation and degradation stages, are observed. Moreover, the effect of the miRNA concentration on the translated protein level is also examined.

The conductance of Ca^{2+} ions through ion channels across a neuron membrane controls the synaptic transmission between two neurons. Memristors are shown to mimic the ionic conductance electronically. Operational amplifiers have been utilized to

imitate the stages of the transmission process proceeding inside the presynaptic neuron, while memristors and differential amplifiers are found to bear resemblance to later phases of the transmission process taking place within the postsynaptic neuron. Excitatory postsynaptic potentials and their summation in two different ways (temporal and spatial) are observed through the neuromorphic circuit.

Biological experimentation is carried out to study the gene expression mechanisms in bacterium *E.Coli*. The environment surrounding the bacteria cells is altered and the *E.coli* response to the environmental changes is analyzed. The cytomorphic circuit simulation results are also obtained by applying the inputs that are electronically analogous to the *E.coli* environmental changes. The experimental observations are strikingly similar to the electronically predicted output of the gene circuit design. Hence, the circuit can predict the cellular response of a living cell with minimal effort and time as published in [143]. Moreover, comparison of the biological experiment results with the electronic simulations outputs validates the cytomorphic circuit design. As an application, electronic gene oscillators modelling the interactions among various genes are designed through the cytomorphic circuit of the gene expression mechanism.

VLSI fabrication of the neuromorphic circuit is performed using 0.13µm IBM CMOS technology. Comparison of the neuromorphic circuit fabricated chip outputs with biological experimentally reported data proves the validity of the neuromorphic circuit design. The neuromorphic circuit is used to model the biochemical pathway of the neural DNA transcription initiation that occurs within the postsynaptic neuron after the synaptic transmission process. Utilization of the memristor circuit element in the proposed model can lead to the development of miniaturized, highly competent and energy efficient artificial neural remedies at the molecular level. Moreover, effects of any chemical changes on neural functionality and bio-chemical pathways can also be observed by altering the corresponding electronic parameter in the circuit model. The proposed VLSI implementation of the neuromorphic circuit thus provides an emulation platform for computational neuroscience at the molecular level. Hence, this doctoral research helps in taking a step further towards the design of bioelectronic circuits which will be capable of modeling complex biochemical pathways and unique interactions among genes, as well as among neurons at the molecular level. In this way, complex biological processes can be studied electronically without the risk of experimental complications.

IBM has designed neurosynaptic computer chip, named it True North, that is based on the concept of synaptic transmission dependent on neuron-to-neuron communication process [144]. The digital neurons in the chip communicate through spike signals. The neuromorphic circuit design concept proposed in this thesis (as published in [145]) is similar to the IBM commercial neuromorphic chip design because it is also based on synaptic transmission dependent process and it generates spikes (excitatory post synaptic potential) that becomes an input for next neuron for progressing the neuron-to-neuron communication process.

7.2 FUTURE WORK

7.2.1. Simulation and Treatment of Neurological Disorders

The neuromorphic circuit model can be used to simulate at molecular level, neurological disorders that are related to the synaptic transmission process such as Alzheimer's disease and Parkinson's disease. In addition, the fabricated chip can be considered as possible future substitute (implant) for damaged neurons that are not able to generate the required *EPSP*s through the synaptic transmission process. Effects of severe neurological diseases can be predicted and the neurological disorders can be treated with the help of the proposed electronic circuit designs.

7.2.2. Integration

The bioelectronic circuits presented in this thesis can yield multiple benefits when they are combined with similar circuit designs. Experimental complications can be triumphed over by analysing complex biological processes through electronic simulations of the combined circuit. In order to observe the relationship among numerous genes at the same time, the cytomorphic circuit can be connected to itself in various ways. Similarly, the neuromorphic circuit can be attached together through a proper approach so as to examine the process of neuron communication among several neurons. On the other hand, challenging issues can arise when these circuits are integrated with other circuit designs mimicking similar biological phenomena.

REFERENCES

[1] G. M. Walker, J. M. Ramsey, R. K. Cavin, D. J. C. Herr, C. I. Merzbacher, and V. Zhirnov "A Framework for Bioelectronics Discovery and Innovation," NIST, U.S. Dept. Commerce,Feb. 2009.

[2] J. F. Vincent, O. A. Bogatyreva, N. R. Bogatyrev, A. Bowyer, and A. K. Pahl, "Biomimetics: its practice and theory," *J. R. Soc. Interface,* vol. 3, no. 9, pp. 471- 482, Aug. 2006.

[3] R. Sarpeshkar, *Ultra Low Power Bioelectronics: Fundamentals, Biomedical Applications and Bio-Inspired Systems*. New York: Cambridge University Press, 2010.

[4] C. Mead, "Neuromorphic electronic systems," *Proc. IEEE,* vol. 78, no. 10, pp. 1629-1636, Oct. 1990.

[5] E. Neftci, J. Binas, U. Rutishauser, E. Chicca, G. Indiveri, and R. J. Douglas, "Synthesizing cognition in neuromorphic electronic systems," *Proc. Natl. Acad. Sci.,* vol. 110, no. 37, pp. E3468-E3476, Sep. 10, 2013.

[6] L. S. Smith and A. Hamilton (Editors), *Neuromorphic Systems, Engineering Silicon from Neurobiology*. Singapore: World Scientific Publication Co., 1998.

[7] J. L. Payne and A. Wagner. (2013,June). Constraint and contingency in multifunctional gene regulatory circuits. *PLoS Comput. Biol. 9(6),* e1003071. Available: http://www.ncbi.nlm.nih.gov/pubmed/23762020

[8] R. L. Schiek and E. E. May, "Development of a massively-parallel, biological circuit simulator," in *Proc. IEEE Bioinformatics Conf.*, 2003, pp. 620-622.

[9] J. Hasty, D. McMillen, and J. J. Collins, "Engineered gene circuits," *Nature,* vol. 420, pp. 224-230, Nov. 2002.

[10] D. A. Lauffenburger, "Cell signaling pathways as control modules: Complexity for simplicity?," *Proc. Nat. Acad. Sci.,* vol. 97, no. 10, pp. 5031-5033, May 2000.

[11] S. Kauffman, "The large scale structure and dynamics of gene control circuits: an ensemble approach," *J Theor. Biol.,* vol. 44, pp. 167-190, Mar. 1974.

[12] F. Corinto, V. Lanza, A. Ascoli, and M. Gilli, "Synchronization in networks of FitzHugh-Nagumo neurons with memristor synapses," in *20th Euro. Conf. Circuit Theo. Design*, Linkoping, 2011, pp. 608-611.

[13] G. Indiveri, B. Linares-Barranco, T. J. Hamilton, A. van Schaik, R. Etienne-Cummings, T. Delbruck, S. Liu, P. Dudek, P. Hafliger, S. Renaud, J. Schemmel, G. Cauwenberghs, J. Arthur, K. Hynna, F. Folowosele, S. Saighi, T. Serrano-Gotarredona, J. Wijekoon, Y. Wang, and K. Boahen, "Neuromorphic silicon neuron circuits," *Frontiers in Neuroscience,* vol. 5, no. 73, May 2011.

[14] J. Hasler and B. Marr, "Finding a roadmap to achieve large neuromorphic hardware systems," *Front. Neurosci.,* vol. 7, p. 118, Sept. 2013.

[15] Y. Ho, G. M. Huang, and P. Li, "Dynamical Properties and Design Analysis for Nonvolatile Memristor Memories," *IEEE Trans. Circuits Syst. I, Reg. Papers,* vol. 58, no. 4, pp. 724-736, Mar. 2011.

[16] T. Chang, Y. Yang, and W. Lu, "Building Neuromorphic Circuits with Memristive Devices," *IEEE Circuits Syst. Mag.,* vol. 13, no. 2, pp. 56-73, May 2013.

[17] J. Zola, M. Aluru, A. Sarje, and S. Aluru, "Parallel Information-Theory-Based Construction of Genome-Wide Gene Regulatory Networks," *IEEE Trans. Parallel Distrib. Syst.,* vol. 21, no. 12, pp. 1721-1733, Dec. 2010.

[18] R. Vinoth and S. Balaji, "Biomolecular Mimic Circuit for an Allosterically Regulated Enzyme of Pyrimidine Biosynthetic Pathway," *J. Biosens. Bioelectron.,* vol. 3, no. 1, Jan. 2012.

[19] H. H. McAdams and L. Shapiro, "Circuit Simulation of Genetic Networks," *Science,* vol. 269, pp. 650-656, Aug. 1995.

[20] M. L. Simpson, C. D. Cox, G. D. Peterson, and G. S. Sayler, "Engineering in the biological substrate: information processing in genetic circuits," *Proc. IEEE,* vol. 92, no. 5, pp. 848-863, May 2004.

[21] D. P. Clark and N. J. Pazdernik, *Molecular biology*, 2nd ed. Waltham, MA: Academic Press, 2013.

[22] S. M. Rezaul Hasan, "A Novel Mixed-Signal Integrated Circuit Model for DNA-Protein Regulatory Genetic Circuits and Genetic State Machines," *IEEE Trans. Circuits Syst. I, Reg. Papers,* vol. 55, no. 5, pp. 1185-1196, Jun. 6, 2008.

[23] A. Becskei and L. Serrano, "Engineering stability in gene networks by autoregulation," *Nature,* vol. 405, pp. 590-593, Jun. 2000.

[24] H. Qi, A. Blanchard, and T. Lu, "Engineered genetic information processing circuits," *Wiley Interdisciplinary Rev.: Syst. Bio. Medicine,* vol. 5, no. 3, pp. 273-287, 2013.

[25] S. Rialle, L. Felicori, C. Dias-Lopes, S. Peres, S. El Atia, A. R. Thierry, P. Amar, and F. Molina, "BioNetCAD: design, simulation and experimental validation of synthetic biochemical networks," *Bioinformatics,* vol. 26, no. 18, pp. 2298-2304, Sep. 2010.

[26] N. Ekekwe, "Neuromorphs: Replaceable human organs of the future?," *IEEE Potentials,* vol. 27, no. 1, pp. 8-25, Jan. - Feb. 2008.

[27] A. L. Hodgkin and A. F. Huxley, "A quantitative description of membrane current and its application to conduction and excitation in nerve," *J. Physiology,* vol. 117, pp. 500-544, 1952.

[28] D. Purves, G. J. Augustine, D. Fitzpatrick, L. C. Katz, A. LaMantia, J. O. McNamara, and S. M. Williams (Editors), *Neuroscience*, 2nd ed. Sunderland, MA: Sinauer Associates, Inc., 2001.

[29] M. F. Bear, B. W. Connors, and M. A. Paradiso, *NeuroScience, Exploring the Brain*, 3rd ed. Baltimore, MD: Lippincott Williams & Wilkins, 2007.

[30] J. M. Tour and T. He, "The fourth element," *Nature,* vol. 453, pp. 42-43, May 2008.

[31] L. O. Chua and S. M. Kang, "Memristive devices and systems," *Proc. IEEE,* vol. 64, no. 2, pp. 209-223, Feb. 1976.

[32] H. Kim, M. P. Sah, C. Yang, T. Roska, and L. O. Chua, "Memristor Bridge Synapses," *Proc. IEEE,* vol. 100, no. 6, pp. 2061-2070, June 2012.

[33] D. B. Strukov, G. S. Snider, D. R. Stewart, and R. S. Williams, "The missing memristor found," *Nature Lett.,* vol. 453, pp. 80 - 83, May 2008.

[34] F. Hutchison, "Electronic model of synaptic transmission," in *38th Ann. Northeast Bioeng. Conf.* , Philadelphia, PA, 2012, pp. 165-166.

[35] A. S. Demirkol and S. Ozoguz, "A low power VLSI implementation of the Izhikevich neuron model," in *IEEE 9th Int. New Circuits Syst. Conf.,* , Bordeaux, 2011, pp. 169-172.

[36] N. A. Campbell and J. B. Reece, *Biology*. San Francisco, CA: Pearson, 2005.

[37] R. F. Weaver, *Molecular Biology*. Boston, MA, USA: McGraw-Hill, 2005.

[38] L. Farina, A. De Santis, G. Morelli, and I. Ruberti, "Dynamic measure of gene co-regulation," *IET Syst. Biol.,* vol. 1, no. 1, pp. 10-17, Jan. 2007.

[39] D. Wang, M. K. Markey, C. O. Wilke, and A. Arapostathis, "Eigen-Genomic System Dynamic-Pattern Analysis (ESDA): Modeling mRNA Degradation and Self-Regulation," *IEEE/ACM Trans. Computational Biol. Bioinformatics,* vol. 9, no. 2, pp. 430-437, Mar./Apr. 2012.

[40] C. Carlberg and F. Molnar, *Mechanisms of Gene Regulation*, 1 ed. Netherlands: Springer, 2014.

[41] T. A. Brown. (2002). *Genomes (2nd ed.)* [Online]. Available: http://www.ncbi.nlm.nih.gov/books/NBK21128/

[42] V. N. Kim, "MicroRNA biogenesis: Coordinated cropping and dicing," *Nat. Rev. Mol. Cell Biol.,* vol. 6, no. 5, pp. 376-385, May 2005.

[43] L. He and G. J. Hannon, "Micrornas: Small RNAs with a big role in gene regulation," *Nature Rev. Genetics,* vol. 5, no. 7, pp. 522-531, Jul. 2004.

[44] G. M. Cooper. (2000). *The Cell: A Molecular Approach (2nd ed.)* [Online]. Available: http://www.ncbi.nlm.nih.gov/books/NBK9839/

[45] S. Alam and S. M. R. Hasan, "Modelling of calcium ion (Ca+2) conductance in nerve membrane protein channel as memristive circuit element," *IET Electron. Lett.,* vol. 47, no. 25, pp. 1361-1363, Dec. 2011.

[46] A. Zinovyev, N. Morozova, N. Nonne, E. Barillot, A. Harel-Bellan, and A. N. Gorban, "Dynamical modeling of microRNA action on the protein translation process," *BMC Syst. Biol.,* vol. 4, no. 13, Feb. 2010.

[47] T. Huang, S. Wan, Z. Xu, Y. Zheng, K.-Y. Feng, H.-P. Li , X. Kong , and Y.-D. Cai, "Analysis and Prediction of Translation Rate Based on Sequence and Functional Features of the mRNA," *Plos One,* vol. 6, no. 1, Jan. 2011.

[48] R. Brockmann, A. Beyer, J. J. Heinisch, and T. Wilhelm, "Posttranscriptional expression regulation: What determines translation rates?," *PLOS Comput. Biol.,* vol. 3, no. 3, pp. 531-539, Mar. 2007.

[49] B. Alberts, A. Johnson, J. Lewis, M. Raff, K. Roberts, and P. Walter. (2002). *Molecular Biology of the Cell (4th ed.)* [Online]. Available: http://www.ncbi.nlm.nih.gov/books/NBK21054/

[50] A. S. Sedra and K. C. Smith, *Microelectronic circuits*, 6th ed. New York: Oxford University Press, 2010.

[51] *Quantities, Units and Symbols in Physical Chemistry*. IUPAC Physical Chemistry Division, Blackwell Sci., U.K., 1993.

[52] J. A. Sprowl, "Voltage-time-voltage computation circuit using r-c exponential decay circuits to perform multiplication, division, root-finding and logarithmic conversion," U.S. Patent 3 676 661 A, 1972.

[53] B. Razavi, *Fundamentals of Microelectronics*. Nnnew Jersy, USA: John Wiley and Sons, 2008.

[54] J. Wang and M. A. Maldonado, "The ubiquitin-proteasome system and its role in inflammatory and autoimmune diseases," *Cell Mol. Immunol.,* vol. 3, no. 4, pp. 255-61, Aug. 2006.

[55] *CMOSRF8SF (CMRF8SF) Design Manual*: IBM Corp., 2007.

[56] J. S. Mattick and I. V. Makunin, "Non-coding RNA," *Human Mol. Genetics,* vol. 15, pp. R17-R29, Apr. 2006.

[57] C. E. Rasmussen and C. K. I. Williams, *Gaussian Processes for Machine Learning*. London, U.K.: MIT Press, 2006.

[58] M. Merrow, K. Spoelstra, and T. Roenneberg, "The circadian cycle: daily rhythms from behaviour to genes," *Embo Reports,* vol. 6, no. 10, pp. 930-935, Oct. 2005.

[59] A. Wagner, "Circuit topology and the evolution of robustness in two-gene circadian oscillators," *Proc. Nat. Acad. Sci. USA,* vol. 102, no. 33, pp. 11775-11780, Aug. 2005.

[60] P. L. Lowrey and J. S. Takahashi, "Mammalian circadian biology: Elucidating genome-wide levels of temporal organization," *Annu. Rev. Genomics Human Genetics,* vol. 5, pp. 407-441, 2004.

[61] M. F. Princiotta, D. Finzi, S.-B. Qian, J. Gibbs, S. Schuchmann, F. Buttgereit, J. R. Bennink, and J. W. Yewdell, "Quantitating protein synthesis, degradation, and endogenous antigen processing," *Immunity,* vol. 18, pp. 343-354, Mar 2003.

[62] "*Compendium of Chemical Terminology*," International Union of Pure and Applied Chemistry Aug. 2012.

[63] D. W. Bartlett and M. E. Davis, "Insights into the kinetics of siRNA-mediated gene silencing from live-cell and live-animal bioluminescent imaging," *Nucleic Acids Res.,* vol. 34, pp. 322–333, 2006.

[64] X. Wang, Y. Li, X. Xu, and Y. H. Wang, "Toward a system-level understanding of microRNA pathway via mathematical modeling," *Biosystems,* vol. 100, pp. 31-38, Apr. 2010.

[65] *Linear Scaling in Excel*. Available: http://www-ist.massey.ac.nz/dstirlin/CAST/CAST/Stransform/transform3.html

[66] *Linear scale function*. JsDoc Toolkit. 2010 [Online] Available: http://mbostock.github.io/protovis/jsdoc/symbols/pv.Scale.linear.html.

[67] D. P. Bartel, "MicroRNAs: Target Recognition and Regulatory Functions," *Cell,* vol. 136, pp. 215-233, Jan. 2009.

[68] A. J. Giraldez, Y. Mishima, J. Rihel, R. J. Grocock, S. Van Dongen, K. Inoue, A. J. Enright, and A. F. Schier, "Zebrafish MiR-430 promotes deadenylation and clearance of maternal mRNAs," *Science,* vol. 312, no. 5770, pp. 75-79, Apr. 2006.

[69] M. Yang, Y. Wei, F. Jiang, Y. Wang, X. Guo, J. He, and L. Kang, "MicroRNA-133 Inhibits Behavioral Aggregation by Controlling Dopamine Synthesis in Locusts," *PLoS Genetic,* vol. 10, no. 2, 2014.

[70] K. J. Livak and T. D. Schmittgen, "Analysis of Relative Gene Expression Data Using Real-Time Quantitative PCR and the 2(−Delta Delta C(T)) Method," *Methods,* vol. 25, no. 4, pp. 402-408, Dec 2001.

[71] C. Ragan, M. Zuker, and M. A. Ragan, "Quantitative Prediction of miRNA-mRNA Interaction Based on Equilibrium Concentrations," *Plos Comput. Biol.,* vol. 7, no.2, Feb. 2011.

[72] J. Zhao, T. Tenev, L. M. Martins, J. Downward, and N. R. Lemoine, "The ubiquitin-proteasome pathway regulates survivin degradation in a cell cycle-dependent manner," *J. Cell Sci.,* vol. 113, no. 23, pp. 4363-4371, Dec. 2000.

[73] M. D. Siegelin, D. E. Reuss, A. Habel, C. Herold-Mende, and A. von Deimling, "The flavonoid kaempferol sensitizes human glioma cells to TRAIL-mediated apoptosis by proteasomal degradation of survivin," *Mol. Cancer Therapeutics,* vol. 7, no. 11, pp. 3566-3574, Nov. 2008.

[74] R. Alur, C. Belta, V. Kumar, M. Mintz, G. J. Pappas, H. Rubin, and J. Schug, "Modeling and analyzing biomolecular networks," *Comput. Sci. Eng.,* vol. 4, no. 1, pp. 20-31, Jan-Feb. 2002.

[75] C. Morris and H. Lecar, "Voltage Oscillations in the Barnacle Giant Muscle-Fiber," *Biophys. J.,* vol. 35, pp. 193-213, Jul. 1981.

[76] K. M. Hynna and K. Boahen, "Neuronal ion-channel dynamics in silicon," in *Proc. IEEE Int. Symp. Circuits Syst.*, Island of Kos, 2006, pp. 3614 - 3617.

[77] E. Farquhar and P. Hasler, "A Bio-Physically Inspired Silicon Neuron," *IEEE Trans. Circuits and Systems. I: Regular Papers,* vol. 52, no. 3, pp. 477-488, Mar. 2005.

[78] S. P. Adhikari, Y. Changju, K. Hyongsuk, and L. O. Chua, "Memristor Bridge Synapse-Based Neural Network and Its Learning," *IEEE Trans. Neural Net.Learning Syst.,* vol. 23, no. 9, pp. 1426-1435, Jul. 2012.

[79] N. Serafino and M. Zaghloul, "Review of nanoscale memristor devices as synapses in neuromorphic systems," in *IEEE 56th Int. Midwest Symp. Circuits and Systems*, Columbus, 2013, pp. 602-603.

[80] W. Hui, L. Hai, and R. E. Pino, "Memristor-based synapse design and training scheme for neuromorphic computing architecture," in *Proc. Int. Joint Conf. Neural Networks*, Brisbane, 2012, pp. 1-5.

[81] F. E. Schweizer. (2001). Synapses. *Encyclo. Life Sci., John Wiley & Sons, Ltd* [Online]. Available: http://onlinelibrary.wiley.com/doi/10.1038/npg.els.0000207/full

[82] K. Hyongsuk, M. P. Sah, C. Yang, S. Chan, and L. O. Chua, "Memristor Emulator for Memristor Circuit Applications," *IEEE Trans. Circuits Syst. I, Reg. Papers,* vol. 59, no. 10, pp. 2422-2431, Oct. 2012.

[83] A. Rak and G. Cserey, "Macromodeling of the Memristor in SPICE," *IEEE Trans. Comp. Aided Design Integrated Circuits Syst.,* vol. 29, no. 4, pp. 632-636, 2010.

[84] D. Biolek, Z. Biolek, and V. Biolkova, "SPICE modeling of memristive, memcapacitative and meminductive systems," in *Euro. Conf. Circuit Theo. Design*, Antalya, 2009, pp. 249-252.

[85] J. G. Nicholls, A. R. Martin, P. A. Fuchs, D. A. Brown, and M. E. Diamond, *From Neuron to Brain*. Sunderland, MA: Sinauer Associates Inc., 2012.

[86] I. B. Levitan and L. K. Kaczmarek, *The Neuron: Cell and Molecular Biology*, 3rd ed. New York, USA: Oxford University Press, 2002.

[87] F. E. Schweizer (2006). Neurotransmitter Release from Presynaptic Terminals. [Online]. Available: http://onlinelibrary.wiley.com/doi/10.1038/npg.els.0000285/full

[88] L. Sherwood, *Human Physiology: From Cells to Systems*, 8th ed. Belmont, CA: Brooks/Cole Cengage Learning, 2012.
[89] G. N. Patel and S. P. DeWeerth, "Analogue VLSI Morris-Lecar neuron," *Electron. Lett.,* vol. 33. no. 12, pp. 12-13, Jun. 1997.
[90] L. S. Bobrow, *Fundamentals of Electrical Engineering*, 2nd ed. New York, U.S.A.: Oxford University Press, 1996.
[91] L. O. Chua, "Device modeling via nonlinear circuit elements," *IEEE Trans. Circuits Syst.,* vol. 27, no. 11, pp. 1014-1044, Nov. 1980.
[92] L. Garcia, J. Audin, G. D'Alessandro, B. Bioulac, and C. Hammond, "Dual Effect of High-Frequency Stimulation on Subthalamic Neuron Activity," *J. Neurosci.,* vol. 23, pp. 8743-8751, Sept. 24, 2003.
[93] B. Degos, J.-M. Deniau, M. Chavez, and N. Maurice, "Subthalamic Nucleus High-Frequency Stimulation Restores Altered Electrophysiological Properties of Cortical Neurons in Parkinsonian Rat," *PLoS ONE,* vol. 8, Dec. 31, 2013.
[94] R. C. Jaeger and T. N. Blalock, *Microelectronic circuit design*, 4th ed. New York: McGraw-Hill, 2011.
[95] K. R. Delaney and E. E. Stanley (2009), "Calcium and Neurotransmitter Release," in *Encyclo. Life Sci.,* John Wiley & Sons, Ltd [Online] Available: http://onlinelibrary.wiley.com/doi/10.1002/9780470015902.a0000027.pub3/pdf.
[96] L. Cai, B. M. Sutter, B. Li, and B. P. Tu, "Acetyl-CoA Induces Cell Growth and Proliferation by Promoting the Acetylation of Histones at Growth Genes," *Mol. Cell Elsevier Inc.,* vol. 42, no. 4, pp. 426-437, May 2011.
[97] *Foundry technologies 130-nm CMOS and RF CMOS*. IBM Corp., IBM Microelectro. Div., NY, 2003.
[98] C. C. Rumsey and L. F. Abbott, "Equalization of Synaptic Efficacy by Activity- and Timing-Dependent Synaptic Plasticity," *J. Neurophysiology,* vol. 91, no. 5, pp. 2273-2280, May 2004.
[99] N. L. Golding, T. J. Mickus, Y. Katz, W. L. Kath, and N. Spruston, "Factors mediating powerful voltage attenuation along CA1 pyramidal neuron dendrites," *J. Physiol.,* vol. 568, no. 1, pp. 69-82, Oct. 2005.
[100] J. A. Boulant, "Neuronal basis of Hammel's model for set-point thermoregulation," *J. Appl. Physiol.,* vol. 100, no. 4, pp. 1347-1354, Apr. 2006.
[101] D. Fricker and R. Miles, "EPSP amplification and the precision of spike timing in hippocampal neurons," *Neuron,* vol. 28, no. 2, pp. 559-569, Nov. 2000.
[102] J. A. M. Lorteije, S. I. Rusu, C. Kushmerick, and J. G. G. Borst, "Reliability and Precision of the Mouse Calyx of Held Synapse," *Journal of Neuroscience,* vol. 29, no. 44, pp. 13770-13784, Nov. 2009.
[103] S. Saighi, Y. Bornat, J. Tomas, G. Le Masson, and S. Renaud, "A Library of Analog Operators Based on the Hodgkin-Huxley Formalism for the Design of Tunable, Real-Time, Silicon Neurons," *IEEE Trans. Biomedical Circuits and Syst.,* vol. 5, no. 1, pp. 3-19, Feb. 2011.
[104] J. A. T. Pennington and J. S. Douglass, *Bowes & Church's Food Values of Portion Commonly Used*, 18 ed. Baltimore: Lippincott Williams & Wilkins, 2005.
[105] Experimental Guide:, "*Gene and Gene Expression: 122.231*," Massey University.
[106] *The American Heritage Medical Dictionary*. USA: Forbes Inc., Houghton Mifflin Comp., 2007.
[107] M. R. Wenk and A. Z. Fernandis, *A Manual for Biochemistry Protocols*. Singapore: World Scientific Publication, 2007.
[108] G. S. Sittampalam, N. P. Coussens, H. Nelson, M. Arkin, D. Auld, C. Austin, B. Bejcek, M. Glicksman, J. Inglese, V. Lemmon, Z. Li, J. McGee, O. McManus, L. Minor, A. Napper, T. Riss, O. J. Trask, and J. Weidner (Editors). (2004). *Assay Guidance Manual* [Online. Available: http://www.ncbi.nlm.nih.gov/books/NBK53196/].
[109] R. Boyer, *Biochemistry Laboratory, Modern Theory and Techniques*, 2nd ed. New Jersey, USA: Pearson Prentice Hall, 2012.

[110] R. C. Dickson, R. M. Sheetz, and L. R. Lacy, "Genetic-Regulation - Yeast mutants constitutive for βeta-galactosidase activity have an increased level of βeta-galactosidase messenger ribonucleic-acid," *Mol. Cell. Biol.,* vol. 1, no. 11, pp. 1048-1056, Nov. 1981.

[111] W. Li, X. Zhao, S. Zou, Y. Ma, K. Zhang, and M. Zhang, "Scanning assay of β-galactosidase activity," *Appl. Biochem. and Microbio.,* vol. 48, no. 6, pp. 603 – 607, 2012.

[112] M. J. Dykstra, *A Manual of Applied Techniques for Biological Electron Microscopy*. New York, USA: Plenum Press, 1993.

[113] D. Billen and H. C. Lichstein, "Nutritional requirements for hydrogenase production by Escherichia coli," *J. Bacteriol.,* vol. 60, no. 3, pp. 311 – 314, 1950.

[114] P. S. Sypherd and N. Strauss, "Chloramphenicol-promoted repression of β-galactosidase synthesis in Escherichia coli," *Biochem.,* vol. 49, pp. 400 – 407, 1963.

[115] M. Amezaga and I. R. Booth, "Osmoprotection of *Escherichia coli* by peptone is mediated by the uptake and accumulation of free proline but not of proline-containing peptides," *Appl. Environ. Microbio.,* vol. 65, no. 12, pp. 5722 – 5278, Dec. 1999.

[116] L. McLandsborough, *Food Microbiology Laboratory*. Florida: CRC Press, 2005.

[117] "*Preparation of E.coli Culture Glycerol Stocks*," Thermo Fisher Scientific Inc., Online. Available:http://www.thermoscientificbio.com/uploadedFiles/Resources/preparation-ecoli-culture-glycerol-stocks.pdf2012.

[118] N. Da Silva., M. H. Taniwaki, V. C. Junqueira, N. Silveira, M. S. Nascimento, and R. A. R. Gomes, *Microbiological Examination Methods of Food and Water, A Laboratory Manual*. Netherlands: CRC Press/ Balkema, 2013.

[119] M. Versace and B. Chandler, "The Brain of a New Machine," *IEEE Spectrum,* vol. 47, no. 12, pp. 30-37, Dec. 2010.

[120] L. R. Squire, D. Berg, F. Bloom, S. Du Lac and A. Ghosh (Editors), *Fundamental Neuroscience*, 3rd ed. Burlington, MA: Academic Press, Elsevier Inc., 2008.

[121] S. Lee, *The Gilligan Principle (The Problem with Darwinism)*. Bloomington, IN: Booktango, 2013.

[122] Y. Ho, G. M. Huang, and P. Li, "Nonvolatile memristor memory: Device characteristics and design implications," in *IEEE/ACM Int. Conf. Comp.-Aided Design - Digest Tech. Papers, 2009. ICCAD 2009.* , San Jose, CA, 2009, pp. 485-490.

[123] J. C. Magee and E. P. Cook, "Somatic EPSP amplitude is independent of synapse location in hippocampal pyramidal neurons," *Nature Neurosci.,* vol. 3, no. 9, pp. 895-903, Sep. 2000.

[124] R. J. Sayer, M. J. Friedlander, and S. J. Redman, "The Time Course and Amplitude of EPSPs Evoked at Synapses between Pairs of CA3/CA1 Neurons in the Hippocampal Slice," *J. Neuroscience,* vol. 10, no. 3, pp. 826-836, Mar. 1990.

[125] S. M. R. Hasan, "A Novel Mixed-Signal Integrated Circuit Model for DNA-Protein Regulatory Genetic Circuits and Genetic State Machines," *IEEE Trans. Circuits Syst. I, Reg. Papers,* vol. 55, no. 5, pp. 1185-1196, Jun. 2008.

[126] S. Alam and S. M. R. Hasan, "Integrated Circuit Modeling of Biocellular Post-Transcription Gene Mechanisms Regulated by MicroRNA and Proteasome," *IEEE Trans. Circuits Syst. I, Reg. Papers,* vol. 60, no. 9, pp. 2298-2310, Sept. 2013.

[127] L. Garcia, G. D'Alessandro, B. Bioulac, and C. Hammond, "High-frequency stimulation in Parkinson's disease: more or less?," *Trends Neurosci.,* vol. 28, pp. 209-216, Apr. 2005.

[128] P. L. Greer and M. E. Greenberg, "From Synapse to Nucleus: Calcium-Dependent Gene Transcription in the Control of Synapse Development and Function," *Neuron Elsevier Inc.,* vol. 59, no. 6, pp. 846-860, Sept. 2008.

[129] D. Tardito, J. Perez, E. Tiraboschi, L. Musazzi, G. Racagni, and M. Popoli, "Signaling Pathways Regulating Gene Expression, Neuroplasticity, and Neurotrophic Mechanisms in the Action of Antidepressants: A Critical Overview," *Pharmacol Rev,* vol. 58, no. 1, pp. 115-34, Mar. 2006.

[130] M. Matamales, "Neuronal activity-regulated gene transcription: how are distant synaptic signals conveyed to the nucleus? ," *F1000 Research,* vol. 1, no. 69, Dec. 2012.

[131] G. E. Hardingham, F. J. Arnold, and H. Bading, "Nuclear calcium signaling controls CREB-mediated gene expression triggered by synaptic activity," *Nature Neurosci.,* vol. 4, no. 3, pp. 261-267, Mar. 2001.

[132] H. Kang, L. D. Sun, C. M. Atkins, T. R. Soderling, M. A. Wilson, and S. Tonegawa, "An important role of neural activity-dependent CaMKIV signaling in the consolidation of long-term memory," *Cell,* vol. 106, no. 6, pp. 771-83, Sept. 2001.

[133] S. M. R. Hasan and Nazmul-Ula, "Analog CMOS Charge Model for Molecular Redox Electron-Transfer Reactions and Bio-Chemical Pathways," in *Proc. of IEEE Int. Conf. Circuits and Sys.*, Seattle, WA, 2008, pp. 2038-2041.

[134] F. Schubert, J. Gallinat, F. Seifert, and H. Rinneberg, "Glutamate concentrations in human brain using single voxel proton magnetic resonance spectroscopy at 3 Tesla," *Neuroimage,* vol. 21, pp. 1762-1771, Apr. 2004.

[135] M. Goodfellow, N. E. Phillips, C. Manning, T. Galla, and N. Papalopulu, "microRNA input into a neural ultradian oscillator controls emergence and timing of alternative cell states," *Nature Comm.,* vol. 5, Mar 2014.

[136] B. Bonev, P. Stanley, and N. Papalopulu, "MicroRNA-9 Modulates *Hes1* Ultradian Oscillations by Forming a Double-Negative Feedback Loop," *Cell Rep.,* vol. 2, no.1, pp. 10-18, Jul. 2012.

[137] F. Grignani, L. Lombardi, G. Inghirami, L. Sternas, K. Cechova, and R. Dalla-Favera, "Negative autoregulation of *c-myc* gene expression is inactivated in transformed cells," *EMBO J.,* vol. 9, no. 12, pp. 3913-3922, Dec 1990.

[138] A. Rosa and A. H. Brivanlou, "Regulatory Non-Coding RNAs in Pluripotent Stem Cells," *Int. J. Mol. Sci.,* vol. 14, no. 7, pp. 14346-14373, Jul. 2013.

[139] F. Cimadamore, A. Amador-Arjona, C. Chen, C.-T. Huang, and A. V. Terskikh, "SOX2-LIN28/let-7 pathway regulates proliferation and neurogenesis in neural precursors," *Proc. Natl. Acad. Sci.,* vol. 110, no. 32, pp. E3017-E3026, Aug. 2013.

[140] A. Kiparissides, M. Koutinas, T. Moss, J. Newman, E. N. Pistikopoulos, and A. Mantalaris, "Modelling the Delta1/Notch1 Pathway: In Search of the Mediator(s) of Neural Stem Cell Differentiation," *PLOS One,* vol. 6, no.2, Feb. 2011.

[141] V. B. Sampson, N. H. Rong, J. Han, Q. Yang, V. Aris, P. Soteropoulos, N. J. Petrelli, S. P. Dunn, and L. J. Krueger, "MicroRNA Let-7a Down-regulates MYC and Reverts MYC-Induced Growth in Burkitt Lymphoma Cells," *Cancer Research,* vol. 67, no.20, pp. 9762-9770, Oct. 2007.

[142] *Dorland's Medical Dictionary for Health Consumers*. USA: Saunders, Elsevier Inc., 2007.

[143] S. Alam, E.M.-K. Lai, J. Young and S.M.R. Hasan, "Rapid electronic prediction of gene expression regulation in bacterial cells," *Electronics Letters* , vol.50, no.22, pp. 1566-1568, Oct. 2014.

[144] J. Hsu," How IBM Got Brainlike Efficiency From the TrueNorth Chip", IEEE Spectrum, Sep. 2014. Online. Available: http://spectrum.ieee.org/computing/hardware/how-ibm-got-brainlike-efficiency-from-the-truenorth-chip

[145] S.Alam and S.M.R. Hasan, "A VLSI Circuit Emulation of Chemical Synaptic Transmission Dynamics and Post-Synaptic DNA Transcription", in *IEEE Transactions on Very Large Scale Integration Systems*, (Accepted for publication) available online, URL: http://ieeexplore.ieee.org/stamp/stamp.jsp?tp=&arnumber=7081359, accessed 13 Apr. 2015.

APPENDIX A
SOLUTION OF CALCIUM IONS CHANNEL MEMRISTIVE SYSTEM EQUATION

$$\frac{dM(V,t)}{dt} = \lambda_M(V)[M_\infty(V) - M(V,t)] \tag{A-1}$$

Arranging (A-1) in standard linear form;

$$\frac{dM(V,t)}{dt} = \lambda_M(V)M_\infty(V) - \lambda_M(V)M(V,t)$$

Or,
$$\frac{dM(V,t)}{dt} + \lambda_M(V)M(V,t) = \lambda_M(V)M_\infty(V) \tag{A-2}$$

(A-2) is a non-homogeneous first order differential equation with constant forcing function of the form [83]:

$$\frac{dx(t)}{dt} + ax(t) = b \tag{A-3}$$

Where,

$x(t) = M(V,t)$

$a = \lambda_M(V)$

$b = \lambda_M(V)M_\infty(V)$

Multiplying both sides of (A-2) by e^{at} i.e. $e^{\lambda_M(V)t}$

$$e^{\lambda_M(V)t}\frac{dM(V,t)}{dt} + e^{\lambda_M(V)t}\lambda_M(V)M(V,t) = e^{\lambda_M(V)t}\lambda_M(V)M_\infty(V) \tag{A-4}$$

Then,
$$\frac{d}{dt}\left[e^{\lambda_M(V)t}M(V,t)\right] = e^{\lambda_M(V)t}\frac{dM(V,t)}{dt} + e^{\lambda_M(V)t}\lambda_M(V)M(V,t)$$

Or, $$\frac{d}{dt}\left[e^{\lambda_M(V)t}M(V,t)\right]=e^{\lambda_M(V)t}\left[\frac{dM(V,t)}{dt}+\lambda_M(V)M(V,t)\right] \quad \text{(A-5)}$$

Right side of (A-5) excluding the term $e^{\lambda_M(V)t}$ becomes equal to left side of (A-2); therefore,

$$e^{\lambda_M(V)t}\left[\frac{dM(V,t)}{dt}+\lambda_M(V)M(V,t)\right]=e^{\lambda_M(V)t}\lambda_M(V)M_\infty(V) \quad \text{(A-6)}$$

Comparing (A-5) and (A-6)

$$\frac{d}{dt}\left[e^{\lambda_M(V)t}M(V,t)\right]=e^{\lambda_M(V)t}\lambda_M(V)M_\infty(V) \quad \text{(A-7)}$$

Integrating both sides of (A-7)

$$\int\left\{\frac{d}{dt}\left[e^{\lambda_M(V)t}M(V,t)\right]\right\}dt=\int\left\{e^{\lambda_M(V)t}\lambda_M(V)M_\infty(V)\right\}dt \quad \text{(A-8)}$$

Solving (A-8)

$$e^{\lambda_M(V)t}M(V,t)=\int\left\{e^{\lambda_M(V)t}\lambda_M(V)M_\infty(V)\right\}dt+A$$

$$\Rightarrow M(V,t)=e^{-\lambda_M(V)t}\int\left\{e^{\lambda_M(V)t}\lambda_M(V)M_\infty(V)\right\}dt+Ae^{-\lambda_M(V)t}$$

$$\Rightarrow M(V,t)=e^{-\lambda_M(V)t}\lambda_M(V)M_\infty(V)\left(\frac{1}{\lambda_M(V)}\right)e^{\lambda_M(V)t}+Ae^{-\lambda_M(V)t}$$

$$\Rightarrow \quad M(V,t)=M_\infty(V)+Ae^{-\lambda_M(V)t} \quad \text{(A-9)}$$

Determining A:

A is determined from initial condition i.e. $t = 0$ of (A-9)

$$M(V,0) = M_{\infty}(V) + Ae^{-\lambda_M(V)(0)} \qquad \text{(A-10)}$$

At time "0" $M(V,0) = M_0(V)$; therefore (A-10) becomes

$$M_0(V) = M_{\infty}(V) + A$$

$$\Rightarrow A = M_0(V) - M_{\infty}(V) \qquad \text{(A-11)}$$

Substituting value of A from (A-11) into (A-9)

$$M(V,t) = M_{\infty}(V) + \left[M_0(V) - M_{\infty}(V)\right]e^{-\lambda_M(V)t} \qquad \text{(A-12)}$$

where $M_{\infty}(V)$ is forced or steady state response, while $\left[M_0(V) - M_{\infty}(V)\right]e^{-\lambda_M(V)t}$ is natural response of the calcium ion conductance system through nerve membrane protein channel.

APPENDIX B

OPERATIONAL AMPLIFIER CIRCUIT DESIGN

The operational amplifier design used in the bioelectronic circuits throughout the thesis is shown in Fig. B-1.

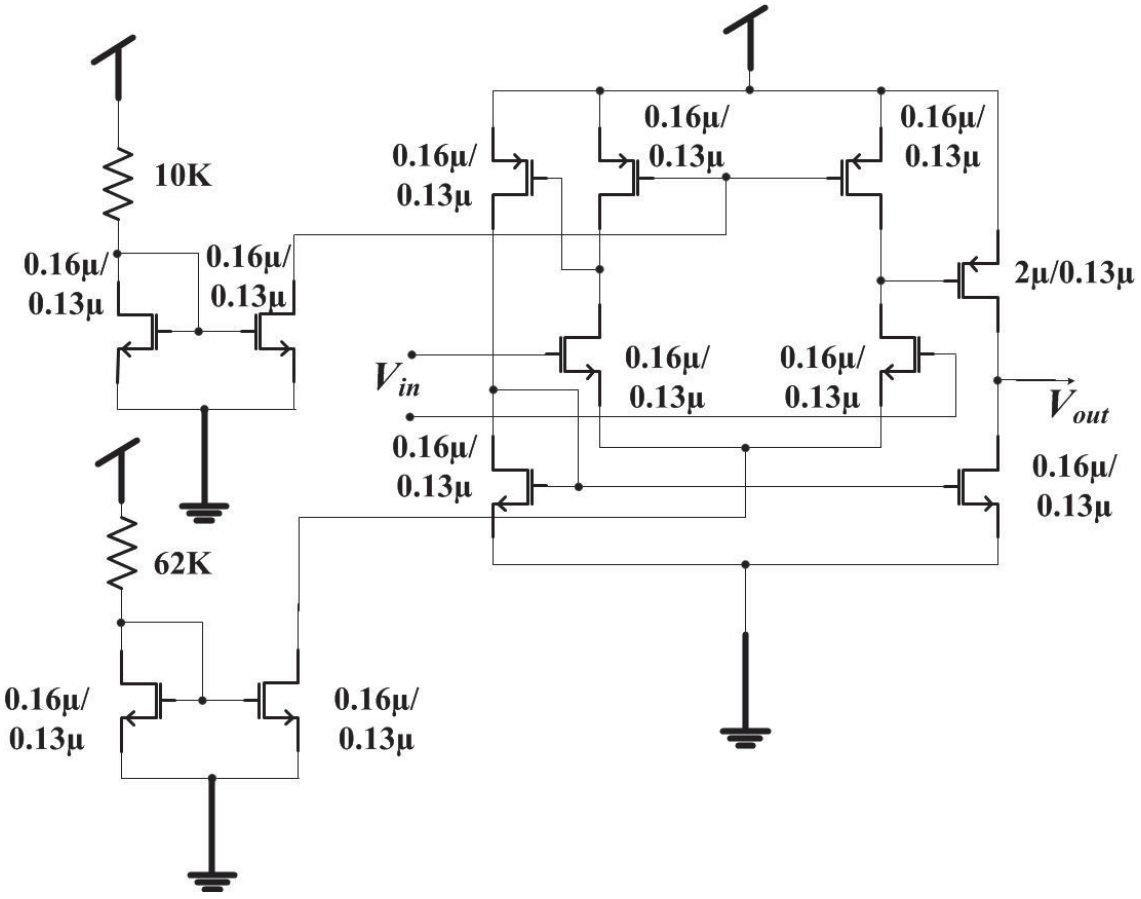

Fig. B-1: Operational Amplifier VLSI design

APPENDIX C
TECHNIQUES FOR PERFORMING ESCHERICHIA COLI EXPERIMENT

C-1. CULTURE MEDIUM PREPARATION PROCEDURE [118]:

The procedure for preparing culture medium consists of following steps:

1. Weighing and Hydrating:

A small disposable plastic container is placed in the weighing balance and the balance is set to 0.0000g. 0.4 g of KH_2PO_4 is weighted properly and is transferred into a clean 400ml Schott bottle. The plastic container is placed again in the balance and is set to 0.0000g again. The procedure is repeated until all chemicals are weighted (except $MgSO_4.7H_20$) and transferred to the Schott bottle (one at a time). After weighing the plastic container is discarded. The bottle is labeled as "*E.coli* basal medium" along with the current date. 400ml of "Reverse Osmosis (RO) water" is measured and is added to the bottle containing the chemical reagents. The solution is stirred and mixed properly. If necessary, heating is also carried out for proper mixing. Finally, 1mL of $MgSO_4.7H_20$ is added per 100mL of basal medium.

2. pH adjustment before sterilization

pH of the solution is adjusted to required value by using a pre-calibrated pH meter as described in [109]. NaOH or HCl solution is used to adjust pH value.

3. Sterilization

Schott bottle caps are covered by aluminium or tin foil. It protects the medium from recontamination or evaporation. Schott bottle containing medium is loaded into autoclave. Autoclave sterilization cycle (temperature/time) is set to 121^oC/15min. Autoclave takes 3 hours for this process (including heating, cooling and sterilization of medium). Technical guide provided with autoclave is followed for operating it.

Sterilization is necessary to kill any germs from basal medium. 3-4 empty flasks/bottles and test tubes are also sterilized in the oven for later use.

4. Post sterilization steps

pH of the medium is again checked after sterilization and adjusted if required by means of a pre-calibrated pH meter. The sterilized material is incubated at 160 rpm (revolution per minute) at 37^{o}C and refrigerated afterwards at 5 ± 3^{o}C. Technical guide provided with incubator is followed for operating it. Incubation provides suitable conditions for culture growth and development [142]. Before performing the practical, culture medium is melted and cooled to 40^{o}C temperature. Medium is maintained at this temperature in a hot water bath for experimental use.

C-2. STREAK PLATE TECHNIQUE [116]:

1. Inoculating loop wire is heated until red hot from Bunsen burner flame. It is placed into glycerol stock containing *E.coli*. The loaded loop is dragged back and forth on agar side of petri dish for making streaks.
2. Loop is heated again and cooled down by placing it on non-streaked agar portion. Four to five parallel streaks are made on remaining non-streaked plate by dragging the loop from previously streaked lines.
3. The above process is repeated for one more time and the plate is incubated.

C-3. BASAL MEDIUM INOCULATION [118]:

1. Inoculation needle is sterilized by placing it under Bunsen burner flame. After cooling it to room temperature it is ready to use.
2. Minimal quantity of bacteria is obtained from colonies developed on streaked plate. For this purpose the bacterial colonies are slightly touched by inoculation needle and smallest possible mass is withdrawn.
3. The needle is inserted into basal medium present inside a test tube.

C-4. SPECTROPHOTOMETRIC ANALYSIS [107]:

For spectrophotometric analysis following steps are carried out:

1. Since, spectrophotometer takes time for initialization; it is switched on 15 min prior to using it. Wavelength is set to 420nm.
2. *E.coli* grown on basal medium is transferred into spectrophotometer cuvette. It is placed in the specific slot, the instrument is auto-zeroed and cuvette is removed.
3. Sample to be analyzed is transferred into another cuvette. It is wiped from outside and inserted into the slot.
4. Start button is pressed and absorbance is noted down once it is stable on the spectrophotometer display screen.

C-5. PERCENT WEIGHT BY VOLUME (% WT/VOL) SOLUTION PREPARATION [109]:

For "x" % wt/vol solution, "x" g of solute is added in 100 mL of solution. Throughout the experiment distilled water is used as solution.

5% lactose solution: 5g of lactose in 100mL of water

5% glucose solution: 5g of glucose in 100mL of water

C-6. MOLAR SOLUTION PREPARATION [109]:

For 1M (Molar) solution, 1mole of solute is added into 1 litre solution. Mass of solute in grams equal to its molecular weight gives 1 mole. Therefore, by adding solute weighing (g) equal to its molecular weight in 1L makes 1 M solution. For example, 0.02M *o*-nitrophenyl-β-galactoside can be prepared by;

0.02 M *o*-nitrophenyl-β-galactoside:

Formula: $C_{12}H_{15}NO_8$

Molecular weight: 301

⇨ 1 M is obtained from 301g $C_{12}H_{15}NO_8$ in 1L water

⇨ 0.02 M --- 301 * 0.02 = 6.02 g $C_{12}H_{15}NO_8$ in 1L water

APPENDIX D

CYTOMORPHIC CIRCUIT LAYOUT

Layout of gene expression cytomorphic circuit presented in Chapter 3, Fig. 3.5 is implemented in Mentor Graphics using 130 nm IBM CMOS process technology. PNP device layout provided with in the IBM technology file is used to implement the PNP BJT amplifiers.

The voltage controlled voltage source $\alpha_R K$ is implemented by using two Op Amps. α_R is applied to negative terminal of first operational amplifier through a 100Ω resistor. 55Ω resistor is connected at the feedback path. This gives a gain of 0.55 that is equal to the ratio RNA transcripts classified as mRNA in small living organisms. Output terminal of the first amplifier (-0.55* α_R) [50] is connected to the second amplifier (at negative terminal) with a gain of 1. It results in final output voltage, α_{mR} = 0.55* α_R. This equation represents that mRNA concentration is controlled by RNA concentration with a gain of 0.55.

Similarly, the voltage controlled voltage source $\alpha_{pri} K_{drosha}$ is also implemented by using two Op Amps. α_{pri} is applied to negative terminal of first operational amplifier through a 100Ω resistor. 100Ω resistor is connected at the feedback path. This gives a gain of 1 that represents that all of primary miRNA transcripts are converted to pre-miRNA transcripts. Output of the first amplifier (-1* α_{pri}) [50] is connected to the second amplifier (at negative terminal) with a gain of 1. It results in final output voltage, α_{pre} = 1* α_{pri}. This equation represents that pre-miRNA concentration is controlled by pri-miRNA concentration with a gain of 1.

A complete layout screen shot is shown in Fig. D-1. Figs. D-2 to D-5 show zoomed in screen shots from different circuit nodes and are captioned accordingly. All layout components are provided in the 130 nm IBM CMOS process technology.

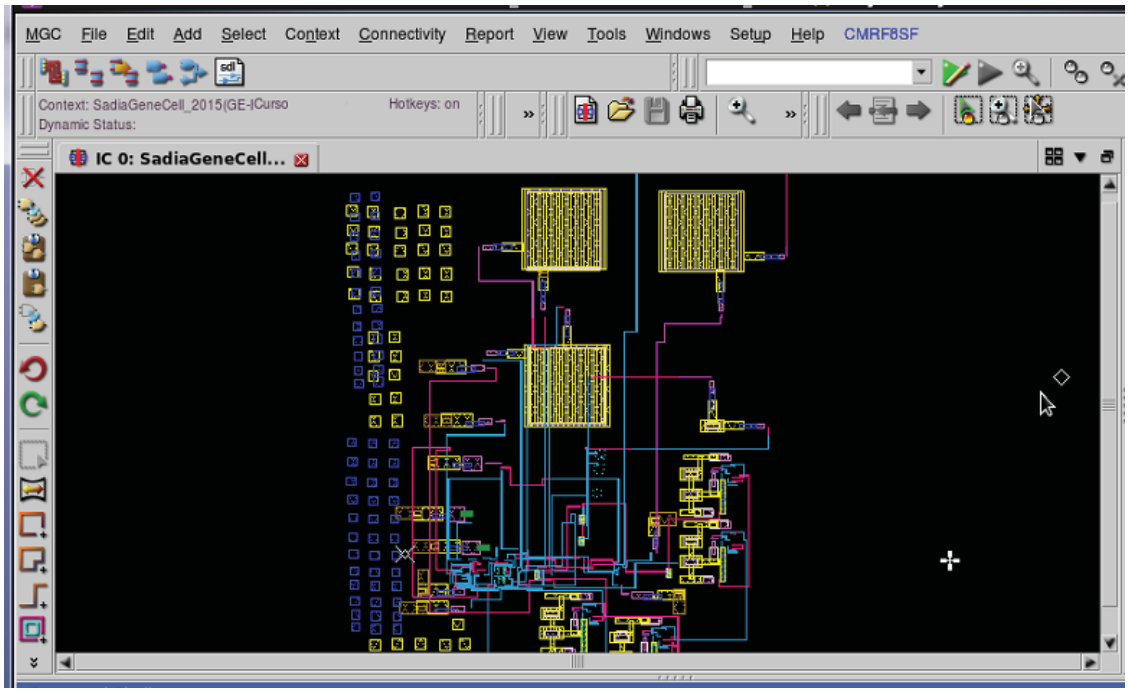

Fig. D-1. A screen shot showing design layout of the cytomorphic gene circuit electronic model presented in Chapter 3, Fig 3.5. The three big box like structures on top right corner are capacitor devices, while the colorful lines are different metal layers connecting the circuit devices. Resistors and transistors are not visible due to their small size. Yellow and blue boxes on the left side are dummy E1 and LY layers that are used to satisfy the DRC density rule.

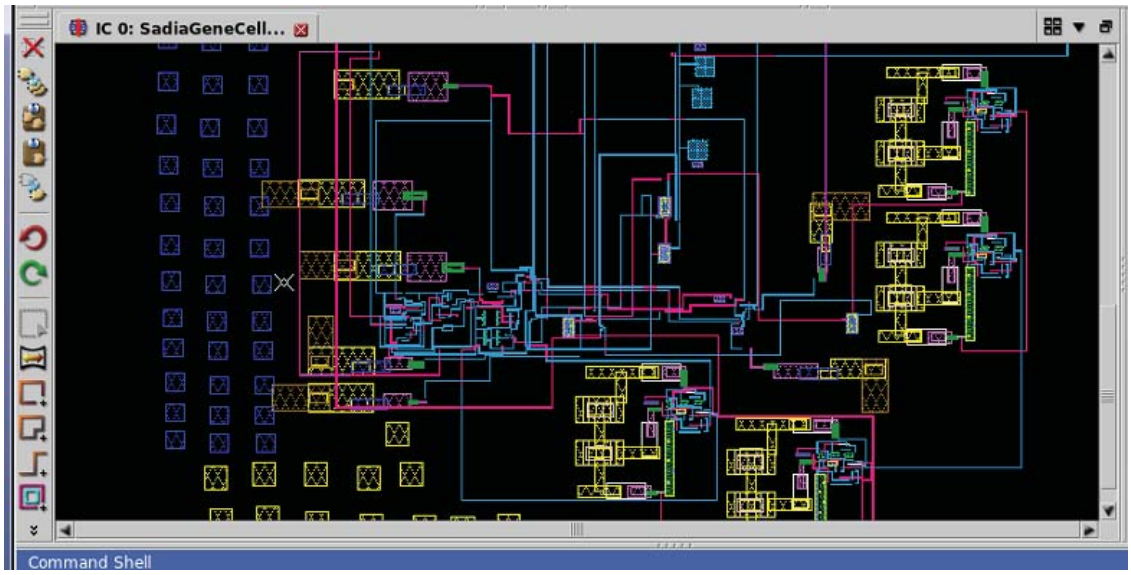

Fig. D-2. A close view of layout shown in Fig D-1.

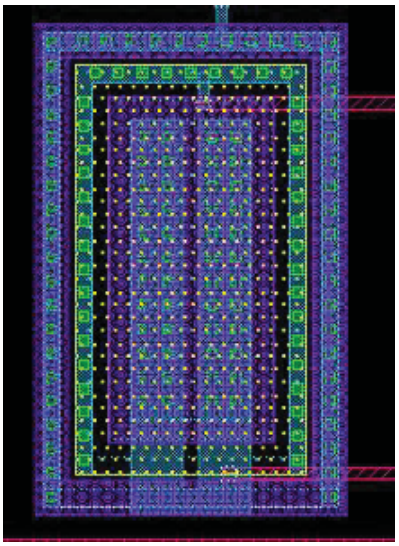

Fig. D-3. A close view of PNP device layout. Outer , middle and inner region represents collector, base and emitter respectively.

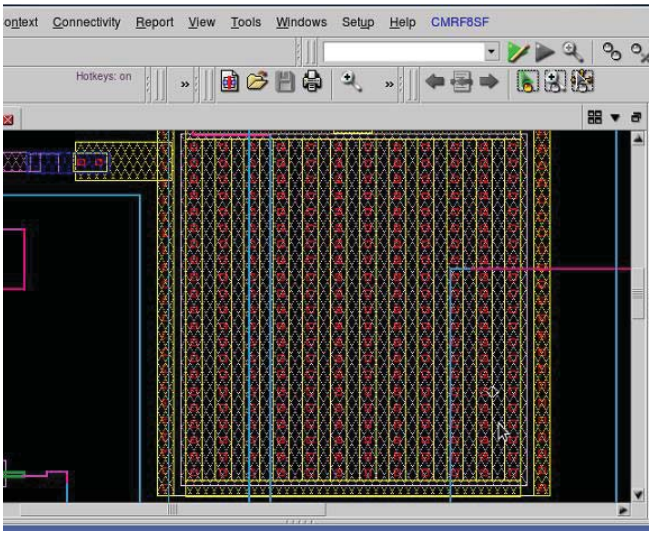

Fig. D-4. A close view of capacitor device. It is made of E1 and QY layers. Several small boxes are vias object connecting E1 and LY layers.

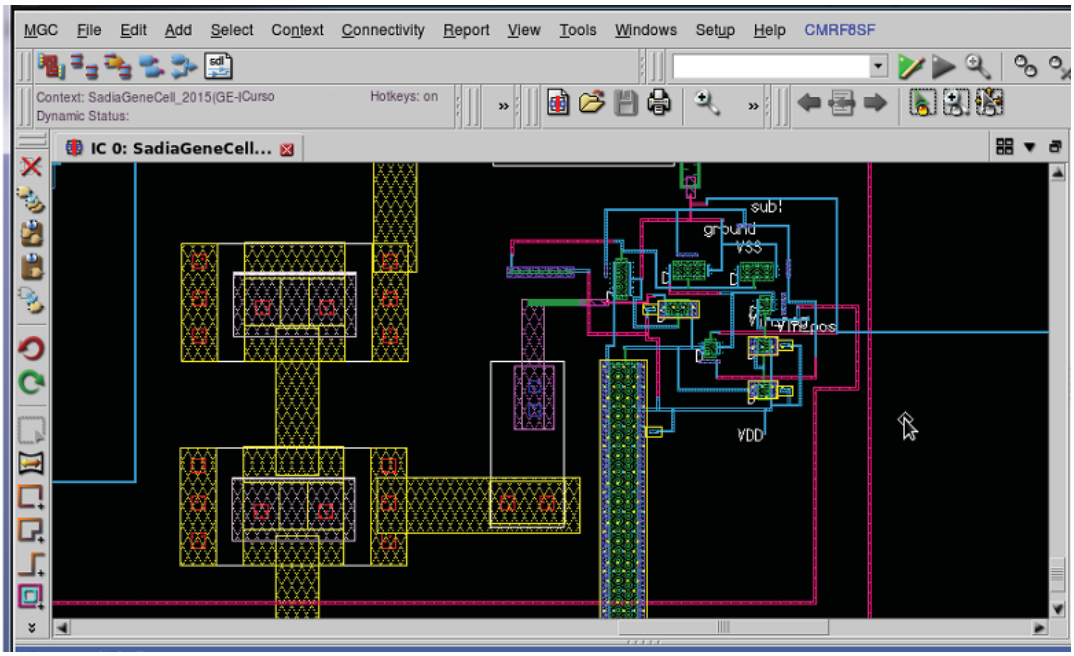

Fig. D-5. A close view of the operational amplifier layout used to implement the voltage controlled voltage source.

Design rule check is carried out for the designed layout and design rule check summary is provided below. It can be seen from the following design rule check summary produced by the Mentor Graphics that the layout has passed all the design rules and there are no errors.

DRC RULE CHECK SUMMARY
==========
==========
=== CALIBRE::DRC-H SUMMARY REPORT
===
Execution Date/Time: Sun Mar 22 08:49:17 2015
Calibre Version: v2012.1_28.18 Wed Mar 7 19:25:24 PST 2012
Rule File Pathname:
/home/sadia/SynpTranCkt.proj/Layout_2014.lib/default.group/layout.views/SadiaGeneCell_2015/SadiaGeneCell_2015.cal/_cmrf8sf.drc.cal_
Rule File Title:
Layout System: GDS
Layout Path(s): SadiaGeneCell_2015.calibre.db
Layout Primary Cell: SadiaGeneCell_2015
Current Directory:
/home/sadia/SynpTranCkt.proj/Layout_2014.lib/default.group/layout.views/SadiaGeneCell_2015/SadiaGeneCell_2015.cal
User Name: sadia
Maximum Results/RuleCheck: 1000
Maximum Result Vertices: 4096
DRC Results Database: SadiaGeneCell_2015.drc.results (ASCII)
Layout Depth: ALL

```
Text Depth:               PRIMARY
Summary Report File:      SadiaGeneCell_2015.drc.summary (REPLACE)
Geometry Flagging:        ACUTE = YES  SKEW = YES  ANGLED = NO  OFFGRID = YES
                          NONSIMPLE POLYGON = YES  NONSIMPLE PATH = YES
Excluded Cells:
Text Mapping:             COMMENT TEXT + RULE FILE INFORMATION
Layers:                   MEMORY-BASED
Keep Empty Checks:        YES

--------------------------------------------------------------------------------
--- SUMMARY
---
TOTAL CPU Time:                 6
TOTAL REAL Time:                8
TOTAL Original Layer Geometries: 3410 (7513)
TOTAL DRC RuleChecks Executed:   1684
TOTAL DRC Results Generated:     0 (0)
```

LIST OF PUBLICATIONS

1. S. Alam and S. M. R. Hasan, “Modelling of calcium ion (Ca^{+2}) conductance in nerve membrane protein channel as memristive circuit element,” *IET Electron. Lett.*, vol. 47, no. 25, pp. 1361-1363, Dec. 2011, doi: 10.1049/el.2011.3332.

A special overview of this paper was presented in “Inside View” of *IET Electronics Letters*, vol. 47, no. 25, pp. 1353, Dec. 2011.

2. S. Alam and S.M.R. Hasan, "Integrated Circuit Modeling of Biocellular Post-Transcription Gene Mechanisms Regulated by MicroRNA and Proteasome," *IEEE Trans. Circuits Syst. I: Reg. Papers*, vol. 60, no. 9, pp.2298-2310, Sept. 2013.

3. S. Alam, E.M.-K. Lai, J. Young and S.M.R. Hasan, "Rapid electronic prediction of gene expression regulation in bacterial cells," *Electronics Letters* , vol.50, no.22, pp. 1566-1568, Oct. 2014.

4. Accepted for publication in IEEE TVLSI:
S.Alam and S.M.R. Hasan, “A VLSI Circuit Emulation of Chemical Synaptic Transmission Dynamics and Post-Synaptic DNA Transcription”, in *IEEE Transactions on Very Large Scale Integration Systems*, (Accepted for publication) available online, URL: http://ieeexplore.ieee.org/stamp/stamp.jsp?tp=&arnumber=7081359, accessed 13 Apr. 2015.

5. S. Alam and S. M.R Hasan, “Bioelectronic Circuit Design for Gene Mechanisms, A basis for Engineered Gene Circuits”, in *Proc. of 20th Electron. New Zealand Conf.*, Sept. 5 – 6, Auckland, New Zealand, 2013.

MASSEY UNIVERSITY
GRADUATE RESEARCH SCHOOL

STATEMENT OF CONTRIBUTION TO DOCTORAL THESIS CONTAINING PUBLICATIONS

(To appear at the end of each thesis chapter/section/appendix submitted as an article/paper or collected as an appendix at the end of the thesis)

We, the candidate and the candidate's Principal Supervisor, certify that all co-authors have consented to their work being included in the thesis and they have accepted the candidate's contribution as indicated below in the *Statement of Originality*.

Name of Candidate: SADIA ALAM

Name/Title of Principal Supervisor: DR. S. M. REZAUL HASAN

Name of Published Research Output and full reference:

S. Alam and S.M.R. Hasan, "Integrated Circuit Modeling of Biocellular Post-Transcription Gene Mechanisms Regulated by MicroRNA and Proteasome," in IEEE Transactions on Circuits and Systems I: Regular Papers, vol. 60, no. 9, pp.2298-2310, Sept. 2013.

In which Chapter is the Published Work: Chapter 3

Please indicate either:

- The percentage of the Published Work that was contributed by the candidate:

  and / or

- Describe the contribution that the candidate has made to the Published Work:

  The research work was carried out by Sadia Alam under the supervision of the principal supervisor (Dr. S.M. Rezaul Hasan).

Candidate's Signature — 14-04-2015 (Date)

Principal Supervisor's signature — 14-04-2015 (Date)

MASSEY UNIVERSITY
GRADUATE RESEARCH SCHOOL

STATEMENT OF CONTRIBUTION TO DOCTORAL THESIS CONTAINING PUBLICATIONS

(To appear at the end of each thesis chapter/section/appendix submitted as an article/paper or collected as an appendix at the end of the thesis)

We, the candidate and the candidate's Principal Supervisor, certify that all co-authors have consented to their work being included in the thesis and they have accepted the candidate's contribution as indicated below in the *Statement of Originality*.

Name of Candidate: SADIA ALAM

Name/Title of Principal Supervisor: DR. S.M. REZAUL HASAN

Name of Published Research Output and full reference:

S. Alam and S. M. R. Hasan, "Modelling of calcium ion (Ca+2) conductance in nerve membrane protein channel as memristive circuit element," in IET Electronic Letters, vol. 47, no. 25, pp. 1361-1363, Dec. 2011.

In which Chapter is the Published Work: Chapter 4

Please indicate either:

- The percentage of the Published Work that was contributed by the candidate:

  and / or

- Describe the contribution that the candidate has made to the Published Work:

  The research work was carried out by Sadia Alam under the supervision of the principal supervisor (Dr. S.M. Rezaul Hasan).

Candidate's Signature — Date: 14-04-2015

Principal Supervisor's signature — Date: 14-04-2015

MASSEY UNIVERSITY
GRADUATE RESEARCH SCHOOL

STATEMENT OF CONTRIBUTION TO DOCTORAL THESIS CONTAINING PUBLICATIONS

(To appear at the end of each thesis chapter/section/appendix submitted as an article/paper or collected as an appendix at the end of the thesis)

We, the candidate and the candidate's Principal Supervisor, certify that all co-authors have consented to their work being included in the thesis and they have accepted the candidate's contribution as indicated below in the *Statement of Originality*.

Name of Candidate: SADIA ALAM

Name/Title of Principal Supervisor: DR. S.M. REZAUL HASAN

Name of Published Research Output and full reference:

S.Alam and S.M.R. Hasan, "A VLSI Circuit Emulation of Chemical Synaptic Transmission Dynamics and Post-Synaptic DNA Transcription" ,in IEEE Transactions on Very Large Scale Integration Systems, (Accepted for publication) available online, URL: http://ieeexplore.ieee.org/stamp/stamp.jsp?tp=&arnumber=7081359, accessed 13 Apr. 2015.

In which Chapter is the Published Work: Chapter 4,5 and 6

Please indicate either:

- The percentage of the Published Work that was contributed by the candidate:

  and / or

- Describe the contribution that the candidate has made to the Published Work:

  The research work was carried out by Sadia Alam under the supervision of the principal supervisor (Dr. S.M. Rezaul Hasan).

Candidate's Signature — 14-04-2015 (Date)

Principal Supervisor's signature — 14-04-2015 (Date)

MASSEY UNIVERSITY
GRADUATE RESEARCH SCHOOL

STATEMENT OF CONTRIBUTION TO DOCTORAL THESIS CONTAINING PUBLICATIONS

(To appear at the end of each thesis chapter/section/appendix submitted as an article/paper or collected as an appendix at the end of the thesis)

We, the candidate and the candidate's Principal Supervisor, certify that all co-authors have consented to their work being included in the thesis and they have accepted the candidate's contribution as indicated below in the *Statement of Originality*.

Name of Candidate: SADIA ALAM

Name/Title of Principal Supervisor: DR. S.M. REZAUL HASAN

Name of Published Research Output and full reference:

S. Alam, E.M.-K. Lai, J. Young and S.M.R. Hasan, "Rapid electronic prediction of gene expression regulation in bacterial cells," in IET Electronics Letters , vol.50, no.22, pp. 1566-1568, Oct. 2014.

In which Chapter is the Published Work: Chapter 5

Please indicate either:

- The percentage of the Published Work that was contributed by the candidate:

  and / or

- Describe the contribution that the candidate has made to the Published Work:

  The research work was carried out by Sadia Alam under the supervision of the principal supervisor (Dr. S.M. Rezaul Hasan)

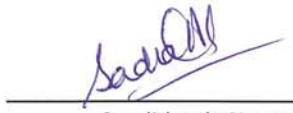

Candidate's Signature

14-04-2015
Date

Principal Supervisor's signature

14-04-2015
Date